Novel Electrochemical Techniques for Metabolic Profiling of Cellular Stress

By

Jennifer Robin McKenzie

Dissertation

Submitted to the Faculty of the

Graduate School of Vanderbilt University

in partial fulfillment of the requirements

for the degree of

Doctor of Philosophy

in

Chemistry

May, 2011

Nashville, Tennessee

Approved:

Professor David E. Cliffel

Professor John A. McLean

Professor John P. Wikswo

Professor David W. Wright

To my most wonderful husband Trent, who makes me happy every day.

ACKNOWLEDGEMENTS

There are a plethora of wonderful people that I must acknowledge for providing me with the support, encouragement, love, knowledge, and wisdom over the years that has led me to this point. First of all, I want to thank my parents, Rob and Dot Merritt, for teaching me everything I needed to know to the best person I could be. They were my first science teachers, helping me with all my science fairs growing up. I still don't know how my mother got us in to meet with the group at Rice working on buckeyballs (pre-Nobel Prize), but I like to think that jump started my science cred back in 3rd grade. My mother is my hero when it comes to leading the way in scientific innovation, always adopting the new diagnostics and treatments to help her patients' years before the bulk of the medical community catches up. My father has always discussed new and interesting science with me, long before I was educated enough to understand it all. This trend continues to this day, and I often come home to find some new book about the history of chemistry sitting on my doorstep. I also want to thank my sister Katie, who has budded into an amazing scientist in her own right. I still think we might be able to get mentioned in some textbooks someday in the future. My cousin Jaymes, for guiding me ever so gently towards attending Hendrix College, and my grandfather, for being so proud of me no matter what.

Of course, not all family is related to you. My wonderful husband Trent, who moved to Nashville for me, and who is now moving to Miami, is the best thing that has ever happened to me, and I feel so blessed and lucky everyday because of him. I have to thank

him for keeping me sane throughout graduate school, helping me celebrate my triumphs and move past my failures to better and brighter outcomes.

Thank you to me committee for your guidance throughout the years. And Dr. McLean, for giving me a phrase I have used so often over the years: “Damn you instrument, do my bidding!” Thank you specifically to Dr. Cliffel for the wonderful ideas, insight, advice, and for providing a welcoming group environment. I will never forget summer volleyball, winter games nights, or Deb’s Oreo pie. I also want to that the Cliffel group. I could not have asked for a better group of people to spend my days with. Everyone is kind, funny, helpful, and just a wee bit sarcastic. My kind of people. I should especially thank Leslie, who I was lucky enough to have join me on the SPE project, and Rachel, who trained me and provided a sounding board whenever needed. Everyone at *VIIBRE*, especially Ron, David, Phil, and Eduardo, and Jason who let me bug them on a regular basis while I tried to learn BioMEMs techniques. Randi and Heather for being the kind of wonderful and goofy friends that everyone should have. A smile was usually just an elevator away.

Liz Gron, Warfield Teague, and Shelly Bradley at Hendrix College for letting me work for them, always supporting me and cheering me on, and giving me the love and guidance throughout undergrad and graduate school. Gary, J.C and Erica for being the coolest neighbors ever. Music City Community Chorus, who let me sing all the solos I could want, and keeping my voice somewhat trained while I focused on my studies.

TABLE OF CONTENTS

Page

LIST OF TABLES

Table Page

LIST OF FIGURES

LIST OF ABBREVIATIONS

AEIROF: Anodically electrodeposited iridium oxidation films

APCs: antigen-presenting cells

ASICs: acid-sensing ion channels

ATCC : America Type Culture Collection

ATP: adenosine triphosphate

BSA: bovine serum albumin

BrA: brefeldin A

cAMP: cyclic adenosine monophosphate

CDC : Center for Disease Control

Ch: replicate chambers of the MAMP

CTx: Cholera toxin

CTxA: A subunit of cholera toxin

CTxB: B subunit of cholera toxin

DMEM: Dulbecco's Modified Eagle Medium

DPBS: Dulbecco's Phosphate Buffered Saline

DTT: dithiothreitol

ECAR: extracellular acidification rate

EDTA: ethylene diaminetetraacetic acid

ELISAs: enzyme-linked immunosorbant assays

EMEM: Eagle's Minimum Essential Medium

E_p: peak potential

$E_{p,a}$: anodic peak potential

$E_{p,c}$: cathodic peak potential

ER: endoplasmic reticulum

ERK1/2: extracellular signal-regulated kinase

FBS: fetal bovine serum

GD: glucose deprivation

GOx: glucose oxidase

HIF-1: hypoxia inducible factor 1

i_b: baseline current

i_p: peak current

i_s: stop flow current

IEC: intestinal epithelial cell

INF-γ: interferon gamma

iNOS: inducible nitric oxide synthase

ISFET: ion-selective field effect transistors

IrOx: iridium oxide

K_{ATP}: ATP-sensitive potassium channels

LAPS: light-addressable potentiometric sensor

LDH: lactate dehydrogenase

LOx: lactate oxidase

LPS: lipopolysaccaride

MAMP: multi-analyte microphysiometer

MAPK: mitogen-activated protein kinase

MHC II: Major Histocompatibility Complex Class II

MTT: 3-(4,5-dimethylthiazol-2-yl)-2,5 diphenyltetrazolium bromide

NeuroP: F_4-Neuroprostanes

NMDA: N-methyl-D-aspartic acid

OCP: open circuit potential

OGD: oxygen glucose deprivation

PB: phosphate buffer

PC: preconditioning

PDMS: poly(dimethylsiloxane)

q_1: cell density at time of plating

q_2: cell density at time of experiment

t_1: time of cell plating

t_2: time of experiment

T_d: Doubling Time

WE: working electrode

V_b: baseline potential

CHAPTER I

INTRODUCTION

While largely ignored by the fields of molecular biology and toxicology until now,[1, 2] the study of cellular metabolism is a vast and interesting field exploring how changes in cellular energetics respond to internal or external influences, as well as how the metabolic state of the cell influences cellular regulation.[3] Noteworthy examples are the changes in metabolism from mutations,[4] contributions of insulin and glucose toward cellular energetic states,[5] and the effects on the cell from exposure to biological toxins.[6, 7] Improved investigations of cellular metabolism through increased methodological capabilities would expand the wealth of knowledge provided by traditional methods of assessing cellular changes due to damage or stress.

The most straightforward traditional method of assessing cellular changes or damage is through microscopy, and has been used to qualify changes in neuronal viability[8-10] and to observe morphological changes occurring due to toxin exposure.[11, 12] The inclusion of fluorescent probes has widened the capabilities of microscopy by allowing labeling of discrete cellular processes. This is helpful when locating specific cell groups, such as neurons on a bed of glia, or when localizing cellular processes like mitochondria.[10, 13] Another example of fluorescent labeling is the internalization and binding of cholera toxin (CTx) which can be visualized by labeling with rhodium, a naturally fluorescent element,[14, 15]or other fluorescent labels.[16, 17]

Aside from microscopy, several popular toxicological methods are based on a toolbox of techniques involving fluorescent labels, often involving labeled antibodies. These methods include enzyme-linked immunosorbant assays (ELISAs), which uses labeled antibodies to quantify antigens, or to study binding, and has been used to quantify transcytosis of staphylococcal enterotoxin B (SEB) from the apical to basal side of an intestinal membrane,[18, 19] determine the production of cytokine production of T cells exposed to the toxin,[12] as well as the pH dependence of cholera toxin (CTx) binding to the GM_1 ganglioside.[16] Fluorescent labels have also been used to determine whether F-actin levels increased after macrophages were exposed to SEB,[12, 20]as well as to image Ca^{2+} release after CTx exposure.[21, 22] These methods require the availability of specific labels, and only provide information at one time point.

Macromolecules and proteins can be quantified without the use of fluorescent probes. Immunoblotting depends on the transfer of macromolecules, such as proteins and nucleic acids, to microporous membranes under the influence of an electric current or capillary action.[23] This method allows for concentration and quantification of proteins or nucleic acids contained within the cell. Further separation with the use of antibody probes has revolutionized and widened the appeal of this immunological technique. These methods have found use in the study of neurons and bacterial toxins where the detection of proteins released due to cellular stress or death,[10] cytochrome C release,[13] F-actin production,[24] or nitric oxide synthase,[25] has been achieved. As with fluorescent probes, specific antibodies are needed to quantify single proteins. In addition, this method requires cellular destruction to extract the desired proteins, as well as several hours to separate and transfer extracted proteins.

While many methods rely on binding to specific antibodies, radiolabeling relies on radioactive isotopes. For example, both CTx and SEB labeled were labeled with ^{125}I to study toxin internalization and binding locations.[14, 16, 26 20] Radiolabeled iodine has also been used to quantify cyclic adenosine monophosphate (cAMP) production after cellular activation by CTx.[14, 26] Quantification of cAMP has also been achieved though radiolabeled phosphorus (^{32}P) or [^{3}H]-adenine, as well as to track the origin of phosphate and adenosine groups that comprise cAMP.[11, 21] These methods have been widely used in the study of cAMP production after CTx exposure. Additionally, ^{51}Cr was often used as a marker of cellular viability,[24, 27, 28] but has largely been replaced by colorimetric techniques, which do not require the handling of chromium or radioactive reagents.

Colorimetric techniques are used to quantify analytes based on absorbance of wavelengths in the visible spectrum. One of the most popular uses of these assays is for the detection of lactate dehydrogenase (LDH), an intracellular enzyme only released upon cell death. LDH is only released from cells after membrane rupture and cell death, making it the ideal marker of cellular damage and death. This test was widely used to evaluate neuronal survival in the development of preconditioning models.[8-10, 13] Through careful application of inhibitors or other cellular effectors, the relative levels of LDH detected yielded valuable information about the cellular pathways involved in neuronal survival after nutrient deprivation.

A similar method employs 3-(4,5-dimethylthiazol-2-yl)-2,5 diphenyltetrazolium bromide (MTT) to assess viability, where the reducing power of the cellular mitochondria reduces the colorless tetrazolium salt to a purple formazan.[29] While cellular viability and metabolic activity are two common uses for the MTT assay, it has also found wide use as

a method for the quantification of cytokines induced by binding by SEB, including IL-2,[18, 27] IL-6, and tumor necrosis factor-α (TNF-α).[20] Additional colorimetric methods include adenosine triphosphate (ATP) assays, which measure the extracellular release of ATP and provides vital clues about the energetic status of the cells, as well as assays to quantify release of nitric oxide (NO), a key molecule released by immune cells during attack.[8, 20, 25, 30] These methods do not allow for real-time measurement and require additional reagents to drive the desired reaction to create the quantifiable color change. Additionally, the results are highly dependent on experimental parameters such as development time, and vary from person to person.

Molecular biology and toxicology have also developed methods to study cellular metabolism. Traditionally, metabolic profiling is obtained by following the uptake of radioactive metabolites.[31] Millions of cells in a culture dish are exposed to radiolabeled deoxyglucose, and the radioactivity of the cells after phosphorylation by hexokinase is assumed to be proportional to the glycolytic rate. These methods utilize a glucose analog with a slow rate of transport into the cell, lowering temporal resolution.[32] Glycolytic rate has also been calculated by quantifying consumption or production of analytes in flasks containing millions of cells.[33, 34] Development of electrochemical sensors for extracellular metabolites has allowed real-time measurements of these analytes in microfluidic environment.[6, 35] Multi-analyte microphysiometry uses several electrochemical sensors to simultaneously monitor the metabolism of cells housed in a microfluidic chamber. This method is uniquely poised to explore metabolic flux due to alterations in cell regulation in real-time, a task that is not achieved with the methods described above.

Real-time investigation of immunological problems was achieved using the multi-analyte microphysiometer (MAMP), which was developed from the Cytosensor® by Molecular Devices. The original instrument measured pH to obtain the extracellular acidification rates (ECAR) using a light addressable potentiometric sensor (LAPS), where the ECAR are correlated to changes in cellular metabolism.[36-38] The MAMP expanded upon the Cytosensor® microphysiometer with the addition of platinum electrodes into a Cytosensor sensor head for monitoring glucose, lactate and oxygen levels amperometrically.[39-42] In the MAMP, oxygen is detected at -0.45 V vs. Ag/AgCl (2M KCl) through direct reduction at a 127 μm diameter platinum electrode. Two 0.5 mm diameter Pt electrodes are coated with glucose oxidase (GOx) and lactate oxidase (LOx), respectively. Glucose and lactate are detected indirectly through the oxidation of hydrogen peroxide which is produced by the reactions of their respective immobilized oxidase enzymes as shown in Equation 1.

$$\beta - \mathrm{D} - \mathrm{glucose} + \mathrm{O_2} \xrightarrow{\text{glucose oxidase}} \delta - \mathrm{D} - \mathrm{gluconolactone} + \mathrm{H_2O_2}$$
$$L - \mathrm{Lactate} + \mathrm{O_2} \xrightarrow{\text{lactate oxidase}} \mathrm{pyruvate} + \mathrm{H_2O_2}$$

Equation 1.Enzymatic Reactions which detect Glucose and Lactate

The MAMP allows for sensitive detection of several analytes in real-time, and can provide key insights into change in cellular function in a way traditional toxicological methods cannot. The addition of multi-analyte microphysiometry to gold-standard techniques already in use will enhance the wealth of knowledge gained when investigating biological systems.

The following chapters will detail how real-time detection of extracellular metabolites proves that acid levels, not lactate, are the superior predictor of neuronal survival following nutrient deprivation. New insights into the metabolic response of neurons to CTx will be revealed, proving a significant "lag-time" of 30 min to an hour between toxin endocytosis and activation of continuous cAMP release is not required, as was previously believed. Additionally, the metabolic activation of different cell groups on the infection pathway of SEB was explored, providing new insight into the immediate effects of toxin binding on cellular homeostasis. Finally, the first studies aimed at further improvement of this already powerful methodology through the development of the first MAMP independent of the Cytosensor will be discussed.

Materials and Methods

Custom Media

Due to the high amounts of buffer present in cell culture media, all MAMP experiments use a modified version of the common cell culture medium, RPMI. The formulation is identical to traditional RPMI except that the phosphate buffer concentration has been lowered to 1 mM PO_4^{3-} and sodium bicarbonate has been removed entirely. The lowering of buffering capacity to minimal levels then allows measurement of changes in extracellular acid production.

The modified RPMI used in the MAMP experiments is also formulated to contain no glucose. Prior to individual experiments, glucose is added to a concentration of 5mM. Traditional RPMI contains 11 mM glucose, but a lower background concentration of 5

mM increases the sensitivity of the method. Unlike lactate, which is produced by the cells and not present in RPMI, glucose is measured as depletion from the chamber. Additionally, the linear range of the GOx sensor can be as low as 5 mM. Assuming a decrease of 0.5 mM glucose in the chamber during each stop-flow, better sensitivity can be gained by lowering the background concentration of glucose. Additionally, extracellular concentrations of glucose in neuronal cells is closer to 5 mM, thus using lower glucose concentrations in RPMI is physiologically relevant.

Data Analysis

Prepared cell inserts and modified sensor heads were placed in the four-channel microphysiometer as previously described.[41] Modified RPMI (5 mM glucose, 1 mM PO_4^{3-}) media was perfused through the chamber at 100 µL per minute using Cytosoft® to maintain a pump-on/pump-off cycle (80 s pump-on, 40 s pump-off) allowing for measurable consumption of oxygen and glucose as well as accumulation of lactate and acidic byproducts. Cell inserts and sensor heads are exchanged after preliminary measurements if cell or electrode performance in not optimal. Immortalized cell lines were typically only used if the ECAR was found to be between 100 and 300 -µV/s. This selection process is one way that biological variation is controlled for in the MAMP.

Once proper cells and sensors have been selected, glucose, lactate and oxygen signals were sampled by the potentiostat once per second for the entirety of the experiment. At the completion of each experiment, cells were perfused with sufficient concentrations of alamethicin to cause formation of pores in the cellular membrane and subsequent cellular death. This allows determination of sensor response during zero metabolic activity and calibration of the glucose and lactate sensors. In all experiments the sensors were

calibrated with modified RMPI media containing different amounts of glucose and lactate. Common combinations included no glucose and no lactate, 0.05 mM lactate and 1 mM glucose, with 0.1 mM lactate and 3 mM glucose, with 0.2 mM lactate and 5 mM glucose. Some experiments benefited from additional calibration steps, and are described as needed. The raw current collected from one chamber of a basal rate experiment with PC-12 cells is shown in Figure 1.

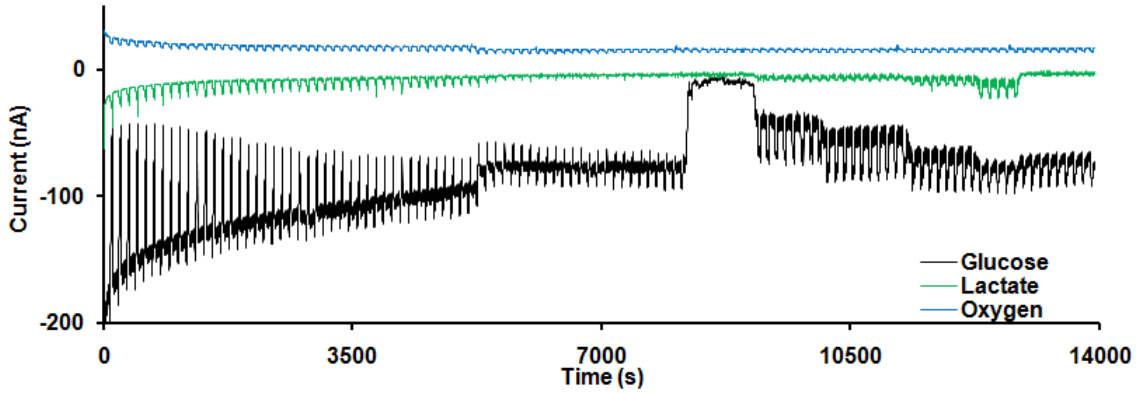

Figure 1. Data collected in one replicate chamber during basal rate experiment with PC12s. Cell necrosis was triggered at 5000 s, and calibrations begun at 8000 s.

After signal collection, raw amperometric signals were filtered using a LabVIEW program with a Fourier transform low pass filter to remove the peristaltic pump noise present in the baseline (Figure 2). Successful removal of the pump noise reduces the noise in the baseline current by a factor of four. As this value is required in the calculation of metabolic rates from raw signals, filtration is essential for removal of instrumental pump noise. While the pumps mainly contribute noise to the baseline signal, in some instances a current spike is observed as the flow starts again. This is often

observed as a spike in the lactate signal, and occurs randomly (Figure 2A). Low-pass filtration also removes or reduces the magnitude of these fluctuations, thus yielding metabolically relevant data (Figure 2B).

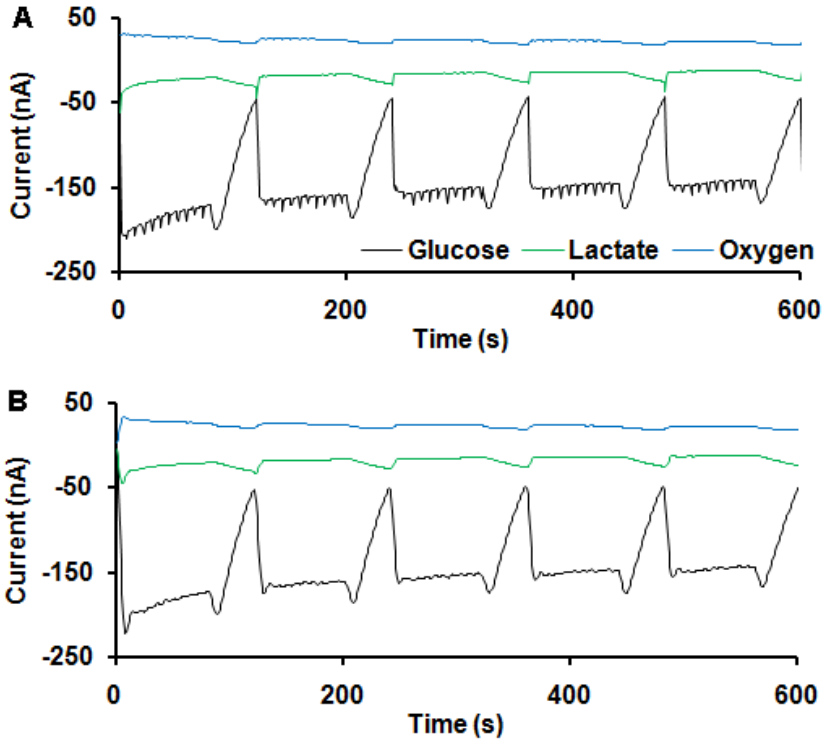

Figure 2. Comparison of signals before and after low-pass filtration. First 10 min of basal rate experiment. (A) Raw signals as measured by multi-chamber multipotentiostat. (B) Raw signals after low-pass filteration with a cut-off frequency of 0.095 Hz.

The filtered data is then handled in EXCEL. The baseline current, i_b, is calculated as the average of seven seconds before the start of the stop-flow period. The peak height, i_s, is typically located 40 s into the stop-flow, but unknown errors in sampling or pumping can cause fluctuations of a few seconds. The MAX and MIN functions in EXCEL are used to sample the seven seconds surrounding the end of the stop-flow period. This

allowed for selection of the current associated with the end of the stop-flow. The i_b and i_s were determined for each stop-flow period, and then used to calculate i_p, or the difference between the baseline current and the current at the end of the stop flow.

Due to the continued consumption of glucose and oxygen from cellular media by the sensors, depletion of glucose and oxygen from the chamber continue after zero metabolic activity has been achieved. In some cases, small fluctuations in lactate were also observed. The average i_p of several stop-flow periods after cell death was calculated for each chamber, and subtracted from the i_p of each stop-flow period to yield the current response due to cellular activity, Δi_p. Any chambers that yield negative values for Δi_p when cells are known to be alive are defined as having a sensor error that results in data which is not physiologically relevant, and is removed from further consideration. This has often occurred with the oxygen sensor in cases where the dead cell i_p is larger than live cell i_p, and can indicate that some change in the electrode occurred, such as a partially loss of the Nafion film at a random time during the experiment. Theoretically, if that were to occur, more oxygen and other interferents would be available for reduction at the electrode surface, resulting in an increase in current magnitude.

Molar glucose consumption and lactate release per stop flow period were calculated by comparing Δi_p to calibrations at the end of each experiment (Figure 3A). The calibration steps were chosen from the i_b during each calibration step. Non-faradaic processes cause the current at the glucose and lactate electrodes to be non-zero even in the absence of analyte, so the relative change in current, where the current at 0 mM glucose or lactate is subtracted from the following calibration steps, is used for the calibration curves.

The linear range of the GOx sensor can fluctuate depending on enzyme activity. The resulting calibration curves are therefore not always linear from 0 to 5 mM, often resulting in no change in current observed between 3 mM and 5 mM glucose. Calibration curves for glucose were plotted as Lineweaver-Burke plots, which plot the inverse of the concentration versus the inverse of the signal (Figure 3B). The resulting linear trend line equation was then used to convert Δi_p to molar concentrations for each stop flow.

The lactate concentrations measured at the LOx electrode were well within the linear range of the sensor, so a simple calibration curve was used to find the linear trend line equation (Figure 3C). Note that no baseline changes in the oxygen signal during lactate and glucose calibrations. This demonstrates that the oxygen tension in the chamber was not dependent on the consumption of oxygen by the oxidase enzymes. Molar oxygen was calculated by assuming the oxygen baseline of dead cells to be the concentration of dissolved oxygen, 0.24 mM, and was calculated as described previously.[43]

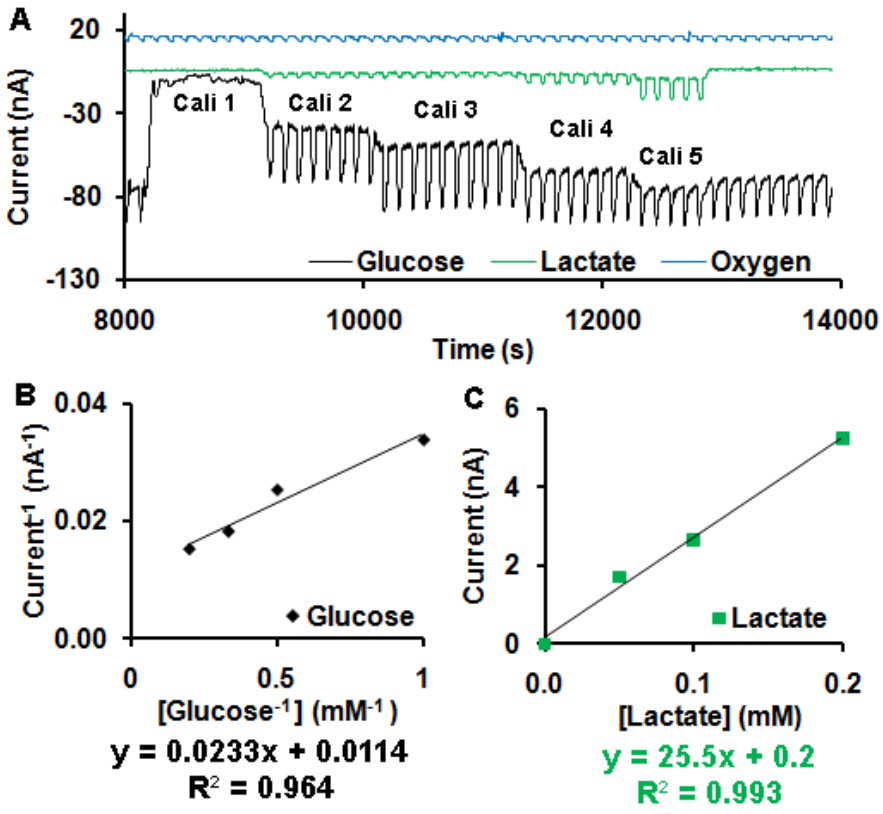

Figure 3. Calibration steps and curves for glucose and lactate. (A) Calibration steps of filtered signal. Cali 1: No glucose or lactate. Cali 2: 1 mM Glu, 0.05 mM Lac. Cali 3: 2 mM Glu, 0.05 mM Lac. Cali 4: 3 mM Glu, 0.1 mM Lac. Cali 5: 5 mM Glu, 0.2 mM Lac. (B) Glucose calibration curve in Lineweaver-Burke plot. (C) Lactate calibration curve.

By accounting for the microfluidic volume (3 µL), the number of cells present, and the length of the stop flow period (40 s), metabolic rates can be calculated in terms of $mol \cdot cell^{-1} \cdot s^{-1}$. The number of cells present in know to be 25% of the cells plated into the cell insert, as the other 75% are blocked by the addition of the spacer. In cell lines were the doubling rate (T_d), or exponential growth rate, of the cells was known, a cell density different from what was plated was calculated and used to calculate metabolic rates.

$$\log(q_2) = \left[\log(2) \times \left(\frac{t_2 - t_1}{T_d}\right)\right] + \log(q_1)$$

Equation 2. Calculation of Cell Density in Cell Insert at Time of Experiment.

Equation 2 is used to calculate q_2, the cell density at the beginning of the experiment, where t_1 and q_1 represent the plating time and plating density respectively and T_d represents the known doubling time of the cell line.

In cases where cell density was unknown, such as primary neurons, or comparisons between cell passages where rates may not be similar, the real-time changes in metabolism were normalized to the basal rate of the replicate prior to exposure. This allowed for changes in rate to be observed as percentages rather than absolute rate values.

Statistical analysis was performed by grouping stop-flow rates from each replicate chamber into basal, exposure, and various post exposure groups, then averaging the replicates. Statistical significance was determined by a two-tailed paired t-test with $p < 0.05$.

CHAPTER II*

INVESTIGATION OF PRECONDITIONING PHENOMENA IN THE MAMP

* This work was the result of a collaborative partnership between the labs of Drs. David Cliffel and BethAnn McLaughlin. Preconditioning models, microscopy, and cell culture were performed by Jacquelynn Brown, Amy Palubinsky, and Dr. Stephanie Zeiger.

The brain is a highly aerobic organ consuming 20% of all ATP generated in the adult body. [44-46] Loss of blood flow during stroke or myocardial infarction starves cells of vital nutrients and oxygen thereby affecting these ATP levels. Neurons are the most vulnerable population of cells to nutrient deprivation and, in concert with glia, undergo rapid changes in metabolic processing in an attempt to compensate for glucose deprivation by evoking powerful protective programs.[47] Preconditioning (PC) occurs when exposure to mild stress activates a cellular defense program leading to a temporal window of decreased vulnerability to subsequent stresses.[8, 10, 48] PC has been observed in several organ systems, such as brain,[49] heart,[50, 51] liver,[52, 53] smooth muscle,[54, 55] intestines,[56] and kidney[57] and has several conserved features, including involvement of mitochondrial ATP sensitive K^+ (K_{ATP}) channels, induction of heat shock proteins, and temporally and spatially controlled caspase 3 activation.[10]

Metabolic dysfunction has been shown to be a core feature of PC, where loss of energy substrates including glucose and oxygen, results in decreased production of ATP,

lowering the ATP/ADP ratio and evoking the opening of K_{ATP} channels .[58, 59] At the molecular level, the central nervous system responds to ATP depletion by altering metabolism so as to use non-preferred substrates for ATP generation, driving lactate through glycolysis, and enhancing expression of genes associated with both aerobic and anaerobic pathways. [48, 60, 61] This drive to adapt is perhaps best typified by the resulting increase in expression of the dimeric protein hypoxia inducible factor 1 (HIF-1). Increased HIF-1 stabilization enhances expression of oxygen capturing molecules, increases glucose transporter expression and results in synthesis of growth factors for vascular optimization.[61]

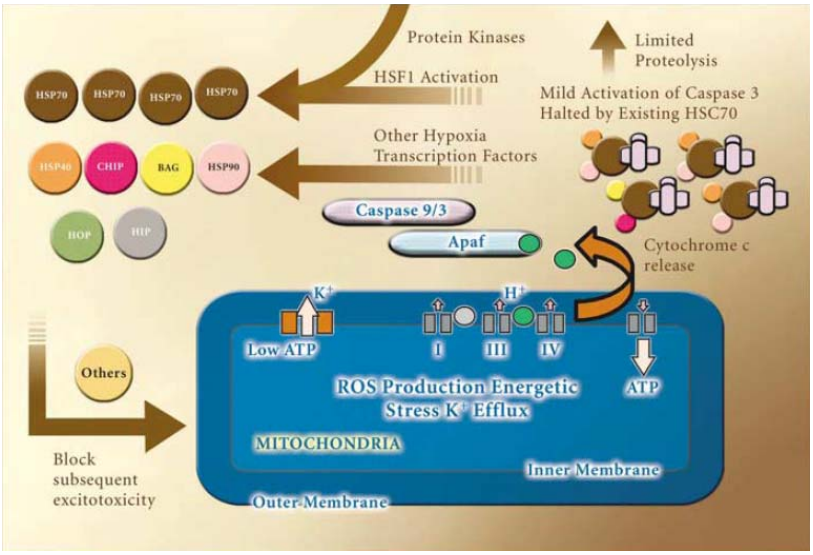

Figure 4. Model of Neuronal Ischemic Preconditioning. Based on observations that preconditioning elicits caspase cleavage and ROS generation, which are required for expression of protection and that this protection requires new protein synthesis, the following pathway was proposed.[48]

The essential metabolic response to oxygen and glucose deprivation (OGD) is to immediately shift movement of pyruvate through the TCA cycle and oxidative phosphorylation to anaerobic respiration, which utilizes LDH to convert pyruvate and NADH to lactic acid and NAD^+. Lactic acid is actively shuttled out of neurons along with protons to produce a net extracellular acidification. Lactate is capable of serving as an alternative fuel for oxidative phosphorylation in the absence of glucose, while co-currently released protons lower intracellular and extracellular pH.[60] Yet the utility of high levels of extracellular lactate as an alternative fuel is contentious in both *in vitro* and *in vivo* settings.[59, 62, 63] Moreover, the cellular responsiveness to lactic acidosis extends beyond energetic dysfunction and includes acid-induced activation of proton sensitive channels know as acid-sensing ion channels (ASICs). These proteins alter neuronal membrane potential and cell signaling and are critical for determining neuronal cell fate.

While excellent pharmacological agents and molecular tools are available to manipulate oxidative phosphorylation, promote glycolysis and block ASICs, we lack a fundamental understanding of the early metabolic events that determine cell fate. Some of these events and interactions include the role of glia in promoting neuronal metabolic compensation under conditions of mild stress and the extent to which anaerobic respiration can be utilized as a short- or long-term survival strategy in preconditioning. To address these questions, we utilized the MAMP[39, 41, 42] for simultaneous electrochemical measurement of extracellular glucose, lactate, oxygen, and acid allowing for real-time determination of metabolic flux. In this work, we used microphysiometry to compare the metabolic status of mixed and pure neuronal cultures undergoing GD, and found that the greatest single predictor of neuronal survival was extracellular acid levels.

Following GD, extracellular acid release in mixed cultures was significantly lower than that of pure neuronal cultures, while release of lactate was not significantly different in either culture systems. Due to the discovery of the importance of extracellular acid following neuronal challenge, a novel acid sensor was developed to improve the sensitivity of acid detection in the microphysiometer. IrOx has been shown to be successful in physiological systems.[64, 65] Anodically electrodeposited iridium oxidation films (AEIROFs) have been reported using numerous methods, including cycling potential or current, or holding current or potential constant.[64, 66, 67]

This work demonstrates an excellent technique for exploring metabolic changes that occur during neuronal stress, and provides new insights into the role of acid in influencing neuronal survival.

Materials and Methods

Materials and Reagents

LDH Toxicology Assay Kit (Tox7), potassium cyanide, GOx (Type IIS from *Aspergillus niger*), bovine serum albumin (BSA, fraction V, 96%), and glutaraldehyde (25 wt % solution in water) were purchased from Sigma (St. Louis, MO). OxyBlot Protein Oxidation Detection Kit was provided by Millipore (Temecula, CA). Psalmotoxin 1 was obtained from Peptides International (Louisville, KY). Stabilized LOx was purchased from Applied Enzyme Technology (Pontypool, UK). Nafion (perfluorosulfonic acid-PTFE copolymer, 5% w/w solution in ethanol) and Pt wire were purchased from Alfa Aesar (Ward Hill, MA). Sterile 20% glucose solution was purchased from Teknova (Hollister, CA). Sterile (L)-lactic acid was purchased from Fisher Scientific (Pittsburg, PA). Lyophilized alamethicin was obtained from A.G. Scientific, Inc. (San Diego, CA) and reconstituted with 1mL absolute ethanol. All media and media supplements were from Invitrogen (Carlsbad, CA) except for the microphysiometry experiments which used custom RPMI (1mM phosphate buffer, glucose and bicarbonate-free) from Mediatech, Inc. (Manassas, VA). Transwell® Polyester Permeable Supports with 3μm pores were purchased from Corning Life Sciences (Lowell, MA). All MAMP consumables were obtained from Molecular Devices Corp. (Sunnyvale, CA).

Cell Culture

Pure neuronal (98% neurons) cortical cultures were prepared from embryonic day 18 Sprague-Dawley rats as previously described.[13] Briefly, cortices were digested in trypsin and dissociated. The resultant cell suspension was adjusted to 335,000 cells/mL and cells were plated in 6-well tissue culture plates containing poly-L-ornithine-treated coverslips in growth media (80% Dulbecco's Modified Eagle Medium (DMEM), 10% Ham's F12-nutrients, 10% fetal bovine serum (FBS) (Hyclone) with 24 U/ml penicillin, 24 μg/ml streptomycin, and 2 mM L-glutamine). After 2 days in culture, cytosine arabinoside (1 μM) was added to inhibit glial cell proliferation, after which cells were maintained in Neurobasal media (Invitrogen) containing 2X N2 supplement, 50X B27 supplement, 50X NS21 supplement,[68] penicillin and streptomycin. All experiments were conducted three weeks following dissection (21-25 days in vitro), when excitotoxicity is expressed fully in our system.

Mixed cultures (80% glial/20% cortical neuron cultures) were prepared as described above for pure neuronal cultures with minor changes. Cells were maintained in growth media without inhibition of glial cells until DIV13 at which point cytosine arabinoside was added. After glial inhibition, cells were maintained in D2C media (94% DMEM, L-glutamine, 2% FBS, 0.025 M HEPES, 0.0125 mM L-glutamine, 24 U/ml penicillin, 24 μg/ml streptomycin) for up to one month (25–29DIV). Alternatively, both cell types were grown as stated but on polyester cell inserts at two times the density for microphysiometry.

Measurement of F_4-neuroprostanes

Lipid peroxidation was assessed through quantification of F_4-neuroprostanes (F_4-NeuroPs), F_2-IsoP-like compounds generated from the free radical-mediated peroxidation of docosahexaenoic acid, a polyunsaturated fatty acid enriched in neurons. F_4-NeuroPs can be measured simultaneously using gas chromatography–mass spectrometry as previously described.[69] Briefly, cells were harvested and 500 μL of the lysate mixed with methanol containing 0.05% butylated hydroxytoluene to prevent auto-oxidation. The remaining lysate was saved for a protein assay to normalize for protein concentrations. F_4-NeuroPs esterified to phospholipids were hydrolyzed by chemical saponification, after which total F_4-NeuroPs were extracted using C-18 and silica Sep-Pak cartridges, purified by thin-layer chromatography, converted to pentaflurobenzyl ester trimethylsilyl ether derivatives, and quantified by stable isotope dilution techniques using gas chromatography/negative ion chemical ionization mass spectrometry using [$^2H_4$]-8-iso-$PGF_{2\alpha}$ (m/z 573) as an internal standard. F_4-NeuroPs are detected at m/z 593.

Detection of Oxidized Proteins

Twenty-four hours following either 60 or 90 min GD exposure, pure neuronal or mixed cultures were harvested into 200 μL of TNEB (50 mM Tris, 2 mM ethylenediaminetetraacetic acid (EDTA), 150 mM NaCl, 8 mM β-glycerophosphate, 100 μM orthovanadate, 1% Triton X-100 (1%), 1:100 protease inhibitor) and total oxidized proteins were determined using the OxyBlotTM Protein Oxidation Detection Kit. Following the cell harvest, 100 μL of the lysate was used for protein assay and the other 100 μL was immediately treated with 50 mM dithiothreitol (DTT) to prevent protein oxidation. The DTT treated lysates was split into two separate 50 μL aliquots, one for the

derivatization reaction containing 2,4-dinitrophenylhydrazine and the other for the negative control containing derivatization control solution. Samples were stored at 4 ºC for no longer than 7 days after derivatization. Equal protein concentrations were analyzed by western blot using antibodies specific for the detection of oxidized proteins provided by the manufacturer. Data represent results from at least 3 independent experiments. Statistical significance was determined by two-tailed paired t-test with $p < 0.05$.

LDH Toxicity Assays

Twenty four hours following each evaluated insult, 40 µL of cell media was removed from each well and used to assess cell viability using a LDH-based in vitro toxicity kit as previously described.[70] In order to account for variation in total LDH content, raw LDH values were normalized to the toxicity caused by 100 µM N-methyl-D-aspartic acid (NMDA) plus 10 µM glycine, which is known to cause 100% cell death in this system.[10] All experiments were performed with a minimum 'n' of 3 using cells derived from at least three independent primary dissections.

ASIC Preconditioning

Chemical preconditioning on mixed cultures was performed as previously described[10] with and without the ASIC channel blocker, Psalmotoxin 1. Briefly, preconditioning reagents were prepared in sterile, glucose-free balanced salt solution (150 mM NaCl, 2.8 mM KCl, 1 mM $CaCl_2$, and 10 mM Hepes; pH 7.3) and 3 mM KCN when needed. Mixed cultures were preconditioned in this media for 90 min and treatment was terminated by rinsing cells (200:1) and replacing the wash solution with maintenance medium. For the half of the cells being treated with Psalmotoxin 1, they were pre-incubated for 30 min in 10 nM Psalmotoxin 1 and the ASIC blocker was also included during preconditioning

and recovery. 18-24 hrs after the preconditioning stimulus cells were treated with the glutamate receptor agonist NMDA as previously described[9] and neuronal viability was assessed 18-24 hrs later via the LDH assay described above. Statistical significance was determined ulitizing a 2 way Anova test followed by Bonferroni posttests.

Analysis and statistics

Except where otherwise noted data were summarized and are represented as mean +/- SEM. The statistical significance of differences between means was assessed using one-way ANOVA at the 95% confidence level ($p < 0.05$), followed by Tukey multiple-comparison tests using GraphPad Prism software.

Instrumentation

A modified Cytosensor® sensor head was created as previously described.[7, 39] The surface of the sensor head was cleaned by scrubbing with water and ethanol, or by polishing with 3 μm diamond polish from Buehler (Lake Bluff, IL). A four channel microphysiometer and Cytosoft® program (Molecular Devices) were used to control pump cycles and hold the temperature at 37 °C. A 120 s stop flow cycle was used with 80 s at a flow rate of 100 μL per min and a stop period of 40 s. A flow/stop-flow system allows for consumption and accumulation of metabolites, as well as increased sensitivity, enabling detection of small changes in metabolism.

Glucose and lactate-sensing electrode films were prepared similarly to those previously described.[8, 39, 42] Briefly, 2 mg of GOx was dissolved in 300 μL of a BSA-buffer solution then quickly mixed with 3 μL of 25% glutaraldehyde. 1.8 mg of LOx was dissolved in 100 μL of a BSA-buffer solution then quickly mixed with 0.8 μL of 25% glutaraldehyde. Electrode films were cast by allowing a droplet of the enzyme solution to dry on the Pt

electrode surface of the sensor head. A droplet of the 5% Nafion solution was also applied to the oxygen electrode (127 μm bare Pt wire) to reduce biofouling as shown in the literature.[41, 42, 71] New solutions were prepared for each experiment.

Glucose, lactate, and oxygen measurements were performed with a multi-chamber bipotentiostat built in-house by the *Vanderbilt Institute for Integrative Biosystems Research and Education* (VIIBRE). Data was collected using LabView software, which when coupled with the potentiostat, enabled monitoring of multiple analytes in four chambers simultaneously. The glucose and lactate sensing electrodes were held at a potential of +0.6 V to oxidize H_2O_2 produced within enzyme films, while the oxygen electrode was held at -0.45 V to reduce dissolved oxygen. All potentials were set versus the Cytosensor Ag/AgCl (2 M KCl) reference electrode in the effluent stream.

Acidification was measured using the LAPS, the original acid-sensing component of the Cytosensor® Microphysiometer. The LAPS is a silicon chip with a thin insulating layer of silicon oxide and silicon nitride that is situated in the bottom of the sensing chamber. Light is pulsed once a second on the silicon, which absorbs it and create electron-hole pairs. These electrons and holes move in opposite directions in the chip's electric field creating a photocurrent that is detected by an external circuit. As extracellular acid increases in the cell chamber, the potential at the surface of the silicon drops, and this change in measured. In some experiments, an additional acid-sensing electrode was incorporated into the sensor head. In these instances, one of the 0.5 mm Pt electrodes in the sensor head was modified with an iridium oxide (IrOx) film instead of a GOx solution to allow for measurement of acidification from the top of the cell chamber. An IrOx solution was prepared using standard procedures.[65, 66] Electrochemical

deposition of the films were achieved by holding the electrode in solution at +0.6 V vs. Ag/AgCl (2 M KCl) with the VIIBRE potentiostat for 7 min. The resulting film is a combination of Ir(IV) and Ir(III) complexes. As the concentration of acid increases in the cell chamber, Ir(III) converts to Ir(IV), causing an increase in potential at the electrode surface. The open circuit potential (OCP) at the IrOx film was measured once a second using a new potentiometric module built for and integrated into the VIIBRE multi-channel bipotentiostat. These films were prepared one day prior to microphysiometry experiments, and sensor heads were stored in phosphate buffer at 4 °C overnight.

Microphysiometry Analysis

Prepared cell inserts and modified sensor heads were placed in the four-channel microphysiometer as previously described.[41] Modified RPMI (5 mM glucose, 1 mM PO_4^{3-}) media was perfused through the chamber at 100 µL per minute using Cytosoft® to maintain a pump-on/pump-off cycle (80 s pump-on, 40 s pump-off) allowing for measurable consumption of oxygen and glucose as well as accumulation of lactate and acidic byproducts. Glucose, lactate and oxygen signals were sampled by the potentiostat once per second for the entirety of the experiment. At the completion of each experiment the neurons were perfused with 15 µM alamethicin which leads to formation of pores in the cellular membrane and subsequent cellular death. This allows determination of sensor response during zero metabolic activity and calibration of the glucose and lactate sensors.

Amperometric signals were analyzed by comparing the stop-flow peaks for live and dead cells. The current response of a given stop flow period, i_p, is defined as the difference between the baseline current and the current at the end of the stop flow. The

current response due to cellular activity, Δi_p, is obtained by subtracting the response during zero metabolic activity from the response with live cells for each stop flow period.

Molar glucose consumption and lactate release per stop flow period were calculated by comparing Δi_p to calibrations at the end of each experiment. Molar oxygen was calculated by assuming the oxygen baseline of dead cells to be the concentration of dissolved oxygen, 0.24 mM, and was calculated as described previously.[43] As each chamber of cells differs slightly in neuronal density and therefore metabolic activity, all signals were normalized to 100% of the average metabolic rate 30 min before GD. Each replicate was boxcar smoothed with a 5 point moving average to further reduce noise and replicate chambers were compared and grouped into basal, exposure, and various post-exposure groups. A gradual decay in metabolic activity is observed for all analytes due to decay in the electrochemical signal, as well as changes to neuronal metabolism due to housing in the microphysiometer. To control for this decay, the changes in metabolic concentrations of all analytes are shown normalized to control chambers. Statistical significance was determined by a two-tailed paired t-test with $p < 0.05$.

Acidification rates at the LAPS were automatically calculated by the Cytosoft® program as the slope of the change in potential during each stop flow, as described. [36] When in use, the OCP module sampled the potential at the IrOx pH sensor once per second. When LAPS and IrOx acid sensors were used together, four calibration solutions with the pH range from approximately 7.1 to 7.4 were perfused through the chamber.

The performance of the IrOx sensor and LAPS in a chamber were evaluated by determining sensor drift, sensitivity to changes in pH over the desired range and the noise of the measured potential. Sensor drift in μV per second was calculated as the slope of

the baseline potential (V_b), or the potential measured during flow periods, over time. Sensitivity to changes in pH were calculated by averaging the V_b for several flow periods for each calibration step to obtain sensitivity in mV per pH unit.

Neuronal Nutrient Deprivation

Mature neuronal cultures were perfused with 5 mM glucose RPMI in the microphysiometer for 90 min. Following the initial 90 min perfusion, RPMI containing no glucose was perfused for either 5 or 90 min, after which the 5 mM glucose RPMI was returned and perfused for an additional 120 min. Control experiments in which no GD occurred were performed simultaneously.

Mixed Culture Nutrient Deprivation

Mixed cultures were perfused with 5 mM glucose RPMI in the microphysiometer for 90 min. Following the initial 90 min perfusion, the media was replaced with RPMI containing no glucose and perfused for either 60 or 90 min, after which the 5 mM glucose RPMI was returned to the cells and perfused for an additional 60 min. Control experiments in which no GD occurred were performed simultaneously.

Results and Discussion

Metabolic Analysis Provides New Insights into Ischemic Preconditioning

A novel model of preconditioning was designed to better approximate neuronal damage that occurs due to transient ischemic attacks. In this model, pure neurons underwent mild (5 min) and lethal (90 min) oxygen glucose deprivation (OGD). It was observed that 5

min OGD resulted in increased ATP production, demonstrating that mild ischemia preserved and enhanced neuronal energetic status.

Figure 5 shows the real-time percent change in metabolic consumption of glucose (Figure 5A and B) and oxygen (Figure 5E and F) and production of lactate (Figure 5C and D) and acidification (Figure 5G and H). Each figure plots the mean ± SEM of the replicate deprived chambers as well as the control replicate chambers. The error bars in the averages are due to the varied metabolic response of neurons in individual chambers in the MAMP. This figure illustrates the temporal resolution of the MAMP technique, as well as the importance of control chambers in the MAMP. All cells placed in the instrument undergo some change as a result of the modified running media used, as well as other experimental factors. For primary neurons, the result is a small but constant decrease in metabolic rates over the course of the experiment. Despite the decrease in metabolism, some trends can be observed in the real-time data. Neuronal glucose consumption does not appear significantly altered after 5 or 90 min GD. Lactate and acid production appear ultimately unaffected after 5 min GD, but the real-time data shows that neurons receiving 90 min GD were altered and did not recover in the same manner as those receiving mild GD. Oxygen consumption is clearly different in both 5 and 90 min GD, where neurons receiving 5 min GD appear to have slightly increased consumption, and those receiving 90 min GD have decreased consumption.

In order to quantify trend in the real-time data, it was normalized to the control chambers and grouped to find average levels of the analytes at different time points during the deprivation and recovery (Figure 6). In all cases, clear trends are observed when comparing control and deprived chambers; however, not all of these trends are

statistically significant due to the biological variation in the primary cultures. While grouping the real-time data allows for statistical analysis, too much weight should not be put on the lack of significance in the resulting trends. The strength of the MAMP technique lies in gaining real-time multi-analyte data in several replicate chambers at once. Additionally,

Evaluation of lactate release revealed that loss of glucose significantly impaired anaerobic lactate release during both the 5 min GD, where lactate release dropped to 0.27 ± 0.06 of control chambers and 90 min GD, where lactate release dropped to 0.00 ± 0.01 of control chambers. The measured lactate release is lower during 90 min GD than 5 min GD due to the excess time allowed for released lactate to be washed out of the chamber. Ten minutes into the recovery period, neither chamber had fully recovered lactate release equivalent to control levels, where neurons receiving 5 min GD had recovered to 0.92 ± 0.05 of control, nor had neurons receiving 90 min recovered 0.67 ± 0.07 of control. Within 2 hrs following the initial 5 min GD, however, lactate release recovered fully. In contrast, the lethal 90 min exposed neurons were unable to recover anaerobic respiration and lactate production to control levels even 2 h following stress (Figure 6A).

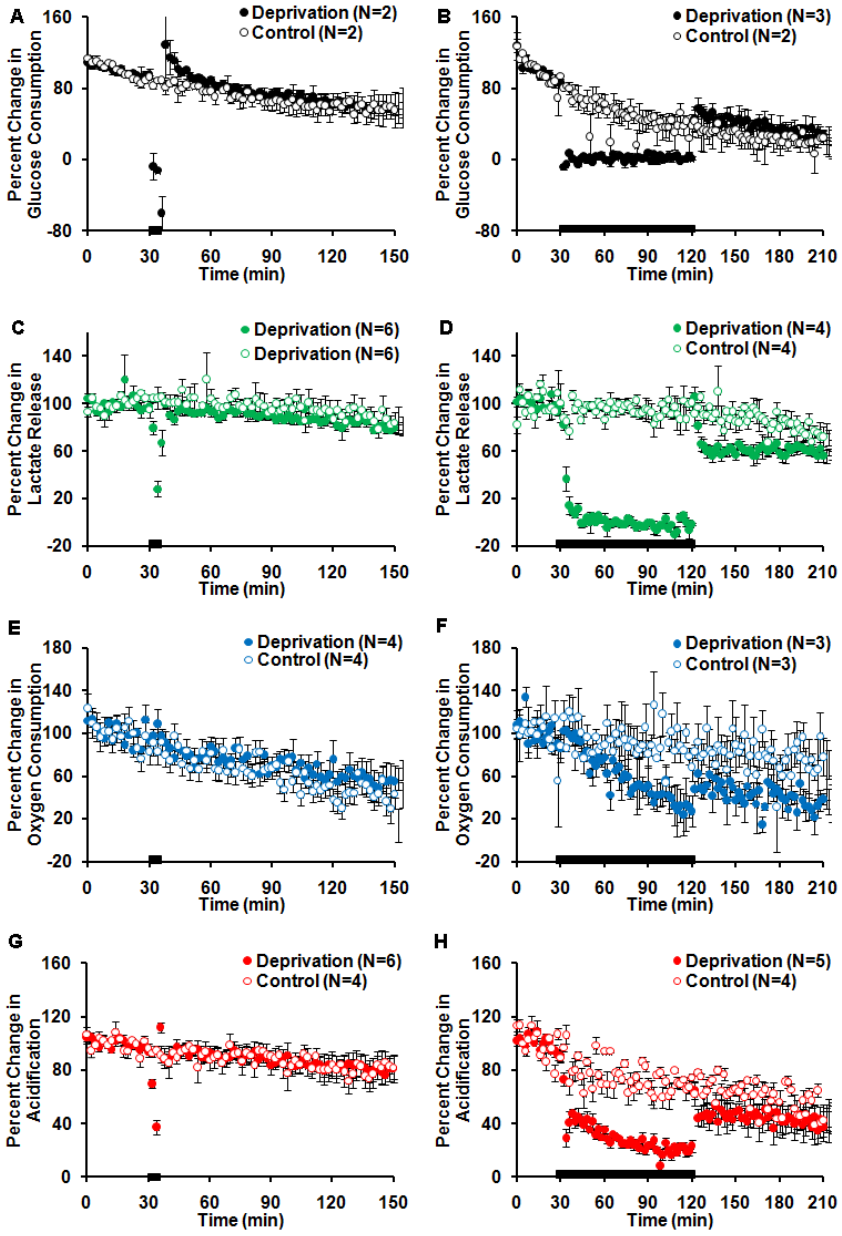

Figure 5. Percent Change in Neuronal Consumption and Production of Metabolites in Real-time. Average of replicate for deprived and control chambers ± SEM. Black bar represent GD. (A) Glucose Consumption, 5 min GD. (B) Glucose Consumption, 90 min GD. (C) Lactate Production 5 min GD. (B) Lactate Production, 90 min GD. (E) Oxygen Consumption, 5 min GD. (F) Oxygen Consumption, 90 min GD. (G) Acidification, 5 min GD. (H) Acidification, 90 min GD.

As shown in Figure 6B, neurons receiving 90 min GD suffered an immediate and fatal reduction in oxygen consumption which continued to drop after glucose was returned, and was 0.39 ± 0.19 of control consumption after 2 hrs of recovery. Neurons receiving only 5 min GD were significantly affected during GD, but within 10 min of recovery had returned to basal levels. The mean of oxygen consumption began to rise, with a significant increase in oxygen consumption to 1.30 ± 1.29 observed at 60 min. After 2 hrs of recovery, oxygen consumption is increased to 1.36 ± 0.39 of control chambers, although the spread in the replicate chambers means that this increase was not significant. The increased oxygen consumption indicates that one of the mechanisms of neuronal preconditioning may be enhanced aerobic activity following mild stress,

Evaluation of acid release revealed both groups underwent an immediate reduction in acid release, dropping to 0.40 ± 0.06 of control for neurons receiving 5 min GD, and 0.36 ± 0.02 of control for neurons receiving 90 min GD. The neurons receiving mild 5 min GD fully recovered after 10 min of glucose returning, with the 90 min GD neurons only recovering to 0.86 ± 0.17 of control levels after 2 hrs. From this study, we observed that aerobic and anaerobic respiration is damaged after lethal GD, and neurons receiving mild GD exhibited no permanent changes to anaerobic respiration, and enhanced aerobic respiration beginning within 1 hr after stress.

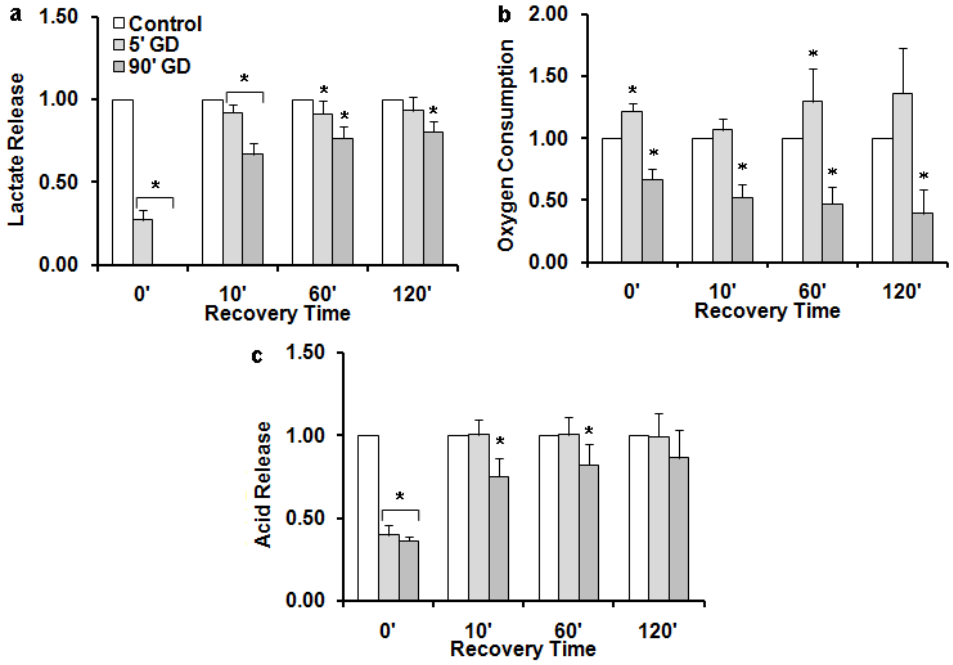

Figure 6. Changes in Pure Neuronal Metalism due to Mild and Lethal Glucose Deprivation. (a) Lactate Release (b) Oxygen Consumption and (c) Acidification were measured using microphysiometry. Each replicate was divided into four time groups: 0' denotes measurements during GD and 10', 60', and 120' denotes time points after glucose media is returned. Data were normalized to control cell measurements at the corresponding time points and represent the mean from at least 3 independent experiments. *denotes statistical significance as compared to control cells with $p<0.05$.

Microphysiometry Model Allows for Real-time Analysis without Significantly Altering Cellular Behavior

Given the immediate metabolic consequences of GD on pure neurons, the next goal was to investigate the effect of GD on mixed cultures to determine how the presence of glia changes consumption and release of extracellular metabolites. Viability assays based on LDH release were performed to compare the viability of neurons and mixed cultures receiving 60 min or 90 min were performed (Figure 7. Mixed cultures had significantly

higher viability than neurons when compared to control chambers, showing that 90 min GD is lethal for neurons, but not for mixed culture.

Representative photomicrographs taken 24hrs following GD demonstrate phase bright neurons on a bed of glia with intact processes in control (Figure 8a) and 60 min exposed cultures (Figure 8b). In contrast, a 90 min exposure resulted in neuronal soma shrinkage, and some loss of phase bright cell bodies (Figure 8c). Figure 8D shows the total loss of neurons due to treatment with excitotoxic NMDA.

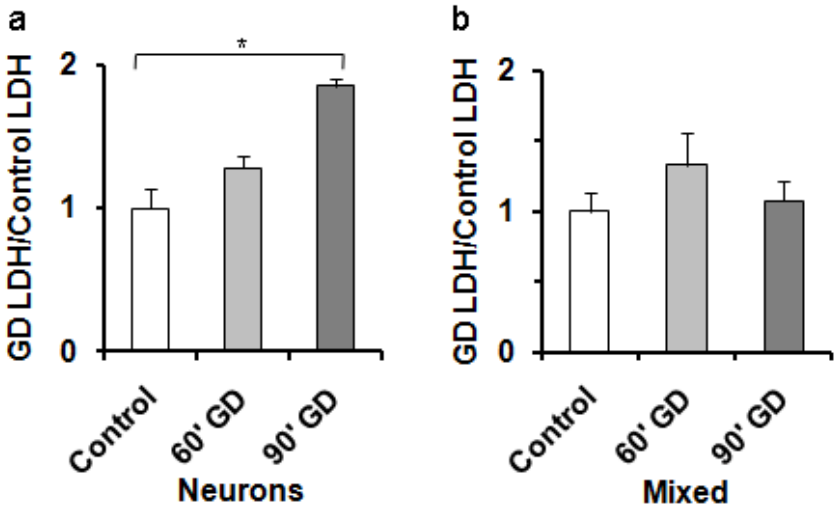

Figure 7. LDH release assays 24 hours after GD Reveal Different Levels of Viability in Neurons and Mixed Cultures. (a) LDH of Neurons as compared to control chambers (b) Mixed Cultures as compared to control chambers.

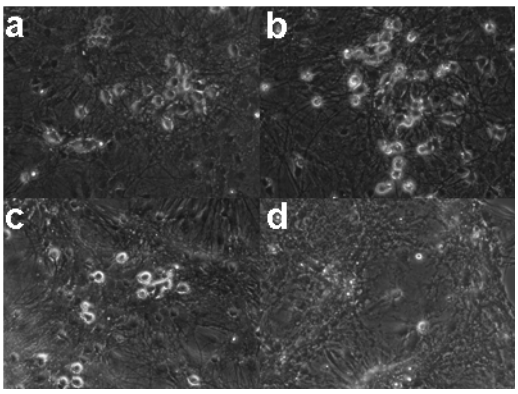

Figure 8. Development on PC Model Compatible with Microphysiometry (a-d) Representative photomicrographs taken 24 hrs after GD illustrate the effect of different exposure durations on neuronal architecture. Neurons from control conditions (a) and those following 60 min GD (b) have phase bright somas with well defined processes whereas the 90 min GD (c) results resulted in neuronal soma shrinkage, and some loss of phase bright cell bodies. (d) Total loss of neurons due to treatment with excitotoxic NMDA.

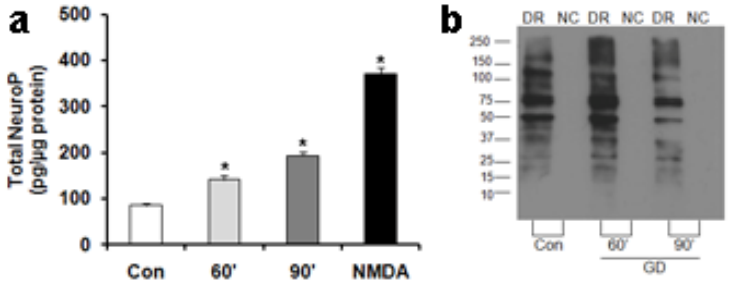

Figure 9. Oxidative Damage to Neurons due to 60 min and 90 min GD (a) Neuroprostane levels measured at 24 hrs were significantly increased in cultures receiving 60 min GD compared to control. Oxidative stress was further enhanced in cultures receiving 90 min GD.(b) Oxyblot from mixed cultures shows protein oxidation and redox stress occur in cultures receiving mild and lethal GD. Data were normalized to control cell measurements at the corresponding time point and represent the mean from at least 3 independent experiments. *denotes statistical significance as compared to control cells with $p<0.05$.

To determine the extent of oxidative stress of neuron after GD, we measured F_4-Neuroprostanes (NeuroP) formation via mass spectrometry. This study revealed that the oxidative stress of mixed cultures receiving GD was increased compared to control cultures (Figure 9.). Interestingly, OxyBlot analysis in pure neuronal cultures following GD results in similar levels and trends in oxidative protein damage to those seen following OGD (Figure 9b). Having established a GD model comparable to our OGD model, we next sought to elucidate the metabolic compensation that occurs when mixed cultures are deprived of glucose.

Extracellular Acid is Reduced for Mixed Cultures Receiving Mild and Extended Glucose Deprivation

The metabolic compensation of mixed cultures during 60 and 90 min GD followed by up to 60 min of recovery time was measured. Figure 10 shows the real-time percent change in metabolic consumption of glucose (Figure 10A and B) and oxygen (Figure 10E and F) and production of lactate (Figure 10C and D) and acidification (Figure 10G and H). Each figure plots the mean ± SEM of the replicate deprived chambers as well as the control replicate chambers. The error bars in the averages are due to the varied metabolic response of neurons in individual chambers in the MAMP. As with Figure 5., this figure illustrates the temporal resolution of the MAMP technique, as well as the importance of control chambers in the MAMP. Despite the decrease in metabolism, some trends can be observed in the real-time data. Glucose and oxygen consumption appear unchanged, and the shift in glucose consumption observed in Figure 10. appears to be due to shifts in baseline current at the glucose electrode as glucose is removed and then returned to the sensing chamber. The interesting trends in this study are those observed in lactate and

acid production. In both 60 and 90 min GD, lactate production drops to null levels during deprivation, and then partially recovers at a steady rate. While the lactate production of the control chambers continue to decline over the course of the experiment, those of deprived chambers appear to reach a lower steady-state of production after deprivation.

Changes in extracellular acidification is also interesting, as those cultures receiving 60 min GD appear to mostly recover, while those receiving 90 min GD exhibit no recovery at all, with extracellular acid levels remaining low.

The real-time data was then normalized to the control chambers and grouped to find average levels of the analytes at different time points during the deprivation and recovery (Figure 11). Oxygen consumption remained unchanged from control during GD, as well as during the recovery period (Figure 11b). This suggests that aerobic respiration is not irreversibly altered in mixed cultures, even after 90 min GD. Upon GD, extracellular lactate release (Figure 11a) and acidification (Figure 11c) immediately decreased to negligible levels. Once glucose was restored, extracellular release of lactate resumed, returning to control levels within an hour for cultures deprived of glucose for 60 min. However, after 90 min GD, recovery was incomplete, reaching only 0.62 ± 0.19 of control levels. Notably, neither group fully recovered extracellular acidification, with those deprived for 60 min reaching 0.81 ± 0.13 of control levels, and those deprived for 90 min reaching only 0.24 ± 0.18 of control levels. In order to further explore the metabolic differences of mixed and pure neuronal cultures following GD, we directly compared the metabolic activity of both culture systems during 90 min GD and recovery.

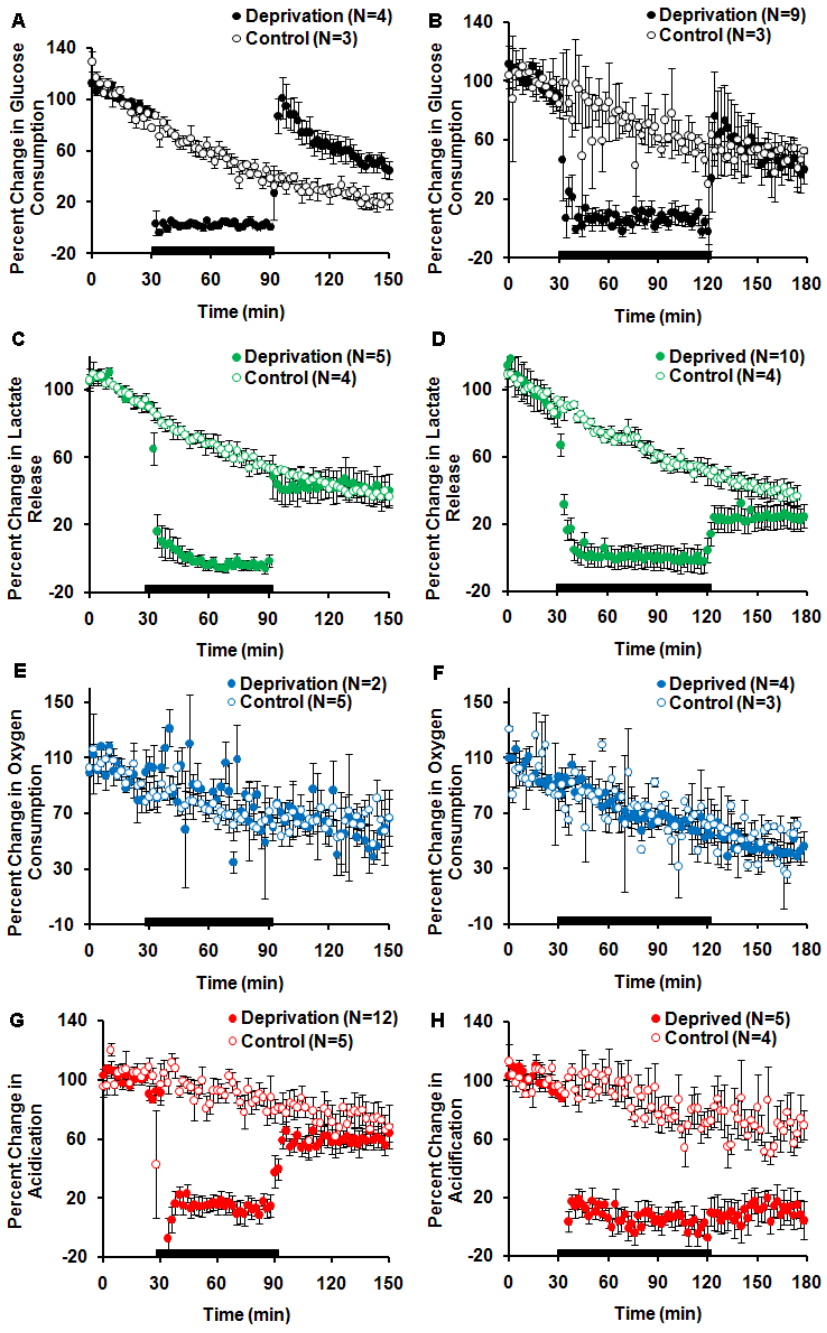

Figure 10. Percent Change in Mixed Cultures Consumption and Production of Metabolites in Real-time. Average of replicate for deprived and control chambers ± SEM. Black bar represent GD. (A) Glucose Consumption, 60 min GD. (B) Glucose Consumption, 90 min GD. (C) Lactate Production 60 min GD. (B) Lactate Production, 90 min GD. (E) Oxygen Consumption, 60 min GD. (F) Oxygen Consumption, 90 min GD. (G) Acidification, 60 min GD. (H) Acidification, 90 min GD.

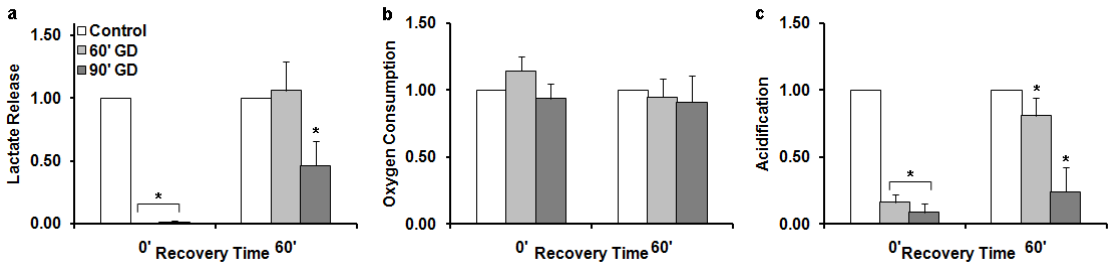

Figure 11. Changes in Mixed Neuronal Metabolism due to Glucose Deprivation. Extracellular metabolites of mixed cultures were measured continuously during 60 or 90 min GD. Some signal decay is observed due to sensor and cellular changes, therefore all following deprivation experiments are expressed as normalized to control chambers. Replicate chambers were grouped into two groups: 0' denotes measurements during GD and 60' denotes the average metabolic levels 60 min after GD. (a) Lactate Release (b) Oxygen Consumption and (c) Acid Release were measured using microphysiometry. *denotes statistical significance as compared to control cells with $p<0.05$.

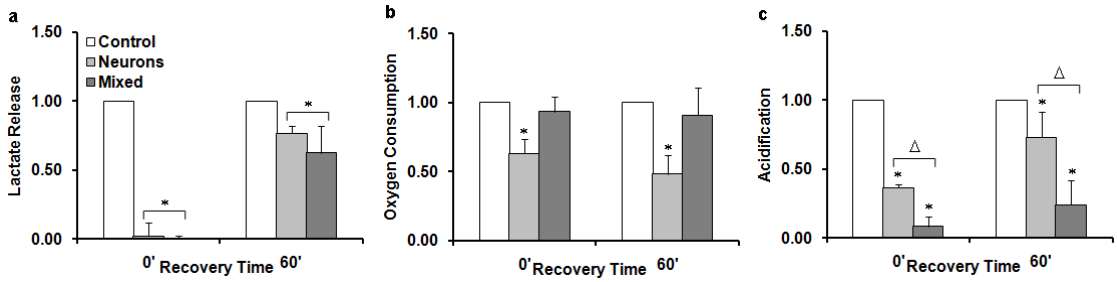

Figure 12. Comparison of 90 min GD in Mixed and Neuronal Cultures(a) Lactate Release (b) Oxygen Consumption and (c) Acid Release were measured continuously following 90 min GD using microphysiometry. Replicate chambers were grouped into two groups: 0' denotes measurements during GD and 60' denotes the average metabolic levels 60min after GD. Data were normalized to control cell measurements at the corresponding time point and represent the mean from at least 3 independent experiments. *denotes statistical significance as compared to control cells with $p<0.05$. Δ denotes statistical significant difference between mixed and neuronal cultures in the specified group.

After one hour of recovery, lactate release, as compared to respective control chambers, for both mixed cultures and pure neurons reaches equivalent levels (Figure 12a). This reveals that handling of lactate is no different between pure neuronal cultures and those with glia. We know that mixed cultures fare better after insults due to the efforts of glial cells, and these results show that the mixed cultures are not concerned with extracellular lactate after extended nutrient deprivation. This is in stark contrast to clinical methods, which strive to control lactate levels following ischemia.

While lactate release is surprisingly similarly affected by 90 min GD in both neuronal and mixed cultures, oxygen consumption and acid release were not. Oxygen consumption remains unchanged in mixed cultures; while a downward trend is observed in pure neuronal cultures (Figure 12b). Extracellular acid release from mixed cultures is significantly lower than neuronal cultures (Figure 12c). Based on the lack of change in oxygen consumption, coupled with the limited recovery of extracellular acidification even after mild stress, the mixed cultures may be undergoing an adaptive measure to prevent acidosis-based ischemic damage by keeping acid levels low and in turn preventing ASIC activation.

The ASIC blocker Psalmotoxin 1 was added to mixed cultures and pure neuronal cultures undergoing preconditioning to explore the importance of ASIC channels in neuronal survival. LDH toxicity assays revealed that neuronal cultures lost protection from preconditioning when ASICs were blocked (Figure 13.). In contrast, there was no statistically significant change in preconditioning of mixed cultures due to blocked ASICs (Figure 13.). This difference may be due to the presence of different protein families of ASIC channels in neurons and glia. Psalmotoxin blocks only ASIC1a, and the

availability of different ASICs in glia may have contributed to the ability of mixed cultures to maintain protection despite blockage of ASICs. Compounding this effect is the observation that relatively more acid is present in the extracellular space of neurons as compared to mixed cultures. ASICs of neurons would then be further activated as compared to ASICs in mixed cultures, and a blockage of ASICs would then have a larger impact on neuronal cultures. This study confirms the hypothesis that preconditioning is directly related to control of extracellular acidification through the use of ASIC sensing.

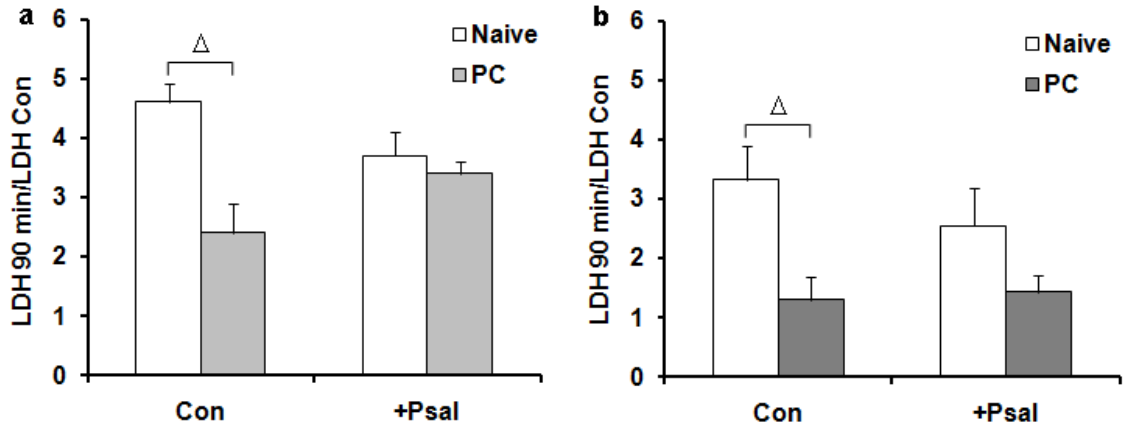

Figure 13. LDH Release Assays of Neurons and Mixed Cultures with Blocked ASICs.Pure neuronal cultures (a) and mixed cultures (b) were preconditioned with and without the addition of the ASIC blocker, Psalmotoxin 1. Cell death was assessed 24h later via LDH release. Despite blocking ASIC1a, no significant effect was observed in mixed cultures, while protection typically afforded by preconditioning was lost in pure neurons. *denotes statistical significance as compared to control cells with $p<0.05$. Δ denotes statistical significant difference between mixed and neuronal cultures in the specified group.

Incorporation of New Sensor Provided Acid Detection with Improved Sensitivity

The emerging importance of extracellular acid in determining neuronal fate led us to incorporate a new pH sensor into the microphysiometer sensor head. Recently we have developed a new module for the VIIBRE potentiostat to allow for simultaneous amperometric and potentiometric sensing independent of the LAPS. This addition was desired due to the amount of instrumental cross-talk observed between the high-frequency LAPS and the low-frequency amperometric sensors, which results in increased noise in the LAPS signal. The new potentiometric module allows for measurement of all four analytes without the addition of cross-talk between the LAPS circuit and VIIBRE potentiostat. A pH-sensitive IrOx electrode was fabricated on the sensor head, as described in methods, to allow for acid sensing from the top of the cell chamber. IrOx sensors were chosen due to functionality at physiological pH and the simplicity with which a film may be formed on platinum electrodes. OCP was measured simultaneously using this new sensor and the LAPS, in addition to the amperometric sensors, to compare signal noise, stability, and response of both acid sensors.

Figure 14A shows the first 5 min of data collection for each sensor in one representative chamber. Data collection begins at the end of a 40 s stop-flow period and a change in potential is observed in both sensors as accumulated acid is washed out of the cell chamber. After 80 s of flow, the baseline has been re-established. The flow is then halted for 40 s, completing the 2 min flow/stop-flow cycle. As discussed in methods, the accumulation of acid results in a decrease in potential at the LAPS and an increase in potential at the IrOx sensor. The noise in the baseline signal of both sensors was determined for multiple electrodes. The average noise in the baseline signal was 0.08 mV

for the IrOx sensor and 0.34 mV for the LAPS. As the total potential shift during a stop-flow can be as low as 1mV, the four-fold decrease in noise from the LAPS to the IrOx sensor can drastically lower the limit of detection for changes in acid in the microphysiometer. This improvement is crucial to allow for detection of smaller changes in cellular metabolism.

While the improved signal-to-noise is the significant feature of the new sensor, it would also be beneficial if the IrOx sensor had equivalent or improved sensitivity to changes in pH when compared to the LAPS. Consistent sensors are also important, as the relevant information, acidification, is calculated from the change in slope during stop-flow, and not the calibrations performed at the end of the experiment.

When calibrated within the chamber without cells, the LAPS were found to have a sensitivity of 43 ± 2 mV per pH unit (N=15). This response is low compared to expected Nerstian response for the LAPS sensor, which should yield a change of 59.1 mV per change in pH unit. These LAPS have been in circulation for several years, and it would appear that the initial Nerstian response has diminished over time.

During microphysiometry experiments, IrOx and LAPS were simultaneously calibrated after zero metabolic activity had been achieved, as described in methods, and sensitivity to pH changes calculated with best-fit linear curves. The IrOx sensors yielded an average sensitivity of 42 ± 3 mV per pH unit (N=11), while the LAPS yielded an average sensitivity of 34 ± 1 mV per pH unit (N=20). Representative calibration plots for the LAPS and IrOx sensor illustrated in Figure 14A are shown (Figure 14B).

The LAPS calibrated in the presence of dead cells yielded a significantly lower sensitivity, which may be due to partial blocking of acid to the LAPS by the dead cells or

by a natural buffering that occurs by the dead cells. The IrOx sensor was originally integrated in order to determine whether the confluent glia were blocking the flux of acid from the neurons to the LAPS sensor, which is situated below the glia. On average, the IrOx sensors were significantly more responsive the changes in pH than LAPS sensors when dead cells were present. There are three possible contributions that this may explain this result. The first theory assumes that IrOx sensors are super-Nerstian, with possible sensitivities as high a 90 mV per pH unit. [66] Super-Nerstian characteristics are common in IrOx sensors, and are highly depending on fabrication method and the pH range tested. While super-Nerstian sensitivities have been achieved with the fabrication method described in methods, these occurred on a different type of Pt electrode. Pre-experiment calibrations were not performed on the IrOx films to limit damage, so it is unclear what the no-cell response of the sensors would have been.

The second hypothesis assumes the IrOx sensor displays Nerstian characteristics, and that the dead glia are in fact blocking the movement of acid from the flow inlet at the sensor head. Due to its location on the sensor head, the IrOx sensor would be able to detect the changes in pH from the calibrant solutions. The LAPS would not be able to sense these changes if the glia were partially blocking the movement of acid to the sensor.

The third hypothesis assumes that the dead cells retain a small amount of natural buffering capacity, resulting in sub-Nerstian responses from both the LAPS and the IrOx sensors. This would result in the sensors measuring smaller changes in pH than what was prepared in the calibrant solutions. It is possible that all three hypotheses contribute to the sub-Nerstian sensitivities of both sensors Without further investigation, including

calibration of the IrOx sensors prior to cell experiments, none of the hypothesis can be eliminated. Future work with glia should be careful to fully characterize both acid sensors prior to experiments in order to answer this question.

Sensor stability over the course of the experiment is also crucial to achieving reliable results. The drift in the baseline signal of both sensors was determined for multiple electrodes. The average drift of the LAPS and IrOx sensor were comparable, and were 0.95 μV/s and 1.2 μV/s, respectively. A drift of this magnitude is well within acceptable limits.

The resulting IrOx sensor exhibited four-fold lower noise over the LAPS sensor, while maintaining comparable sensitivity and stability, and demonstrates that the IrOx sensor is an excellent addition to the multi-analyte microphysiometer to improve the sensitivity of acid detection.

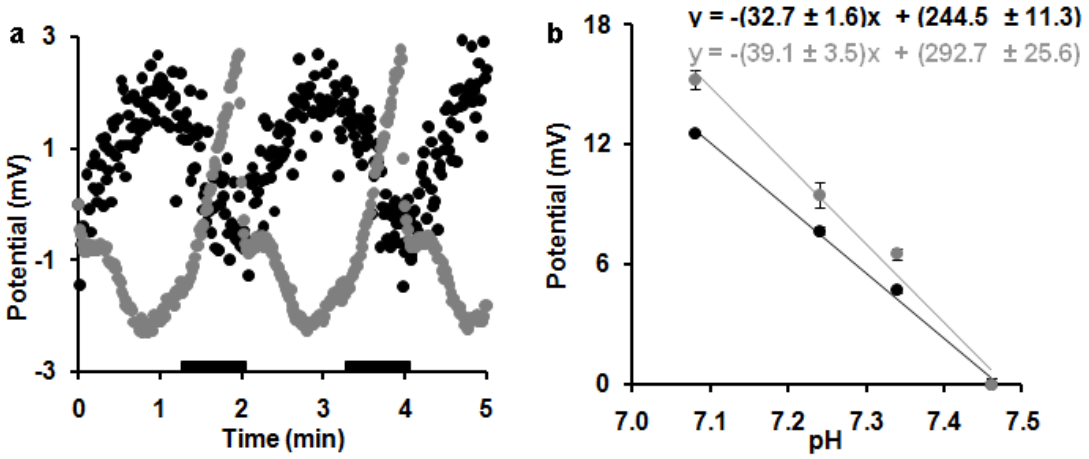

Figure 14.Comparison of LAPS and IrOx Sensor in the MAMP Black lines and symbols represent the LAPS, and grey lines and symbols represent the IrOx sensor. (a) This representative figure illustrates the first 5 min of data collection for each sensor in one chamber. The potential is sampled once per second (b) Calibration curves for the sensors illustrated in (A).

Conclusion

After ischemia, damage is assessed using advanced imaging techniques such as MRI. Currently, the clinical approach to increasing neuronal survival is management of extracellular and intracellular levels of key metabolites. Imaging of glutamate and lactate within neuronal tissue allows for the development of personalized treatment strategies for individuals after ischemic damage, but does not focus on the metabolite poised to cause the most neuronal damage. Unlike traditional toxicology, which uses static measures to measure cellular biomarkers, multi-analyte microphysiometry is a powerful technique which revealed that extracellular acid, not lactate, is the superior predictor of neuronal survival after an ischemic event. This new insight is critical to understanding the effects of neuronal damage following ischemia. Investigation and development of new models using microphysiometry techniques will further understanding of real-time events during stroke, and will be helpful in preliminary testing of new clinical methods for preventing neuronal damage prior to stroke.

These new insights were made possible through the coupling of powerful preconditioning models and multi-analyte microphysiometry. Microphysiometry further confirmed how glia are involved in controlling the metabolic environment of neurons to increase neuronal survival after stress. The emergence of acid as the essential mediator of neuronal survival led to further improvement of the already powerful MAMP through the addition of a new sensor which yielded a near four-fold decrease in noise.

In addition to providing continuous monitoring of metabolism, our method allows for multi-parameter sensing with the ability for adaptation through the addition of new and

novel biosensors. We have repeatedly shown that this platform is the ideal method for observing interesting metabolic issues with high temporal resolution. Future investigations with the MAMP exploring alternative models of ischemia or preconditioning are essential to furthering our understanding of the involvement of metabolism in neuronal stress and survival.

Acknowledgements

The authors would like to thank Dr. Rachel Snider and Dr. Jeannette Stankowski for helpful comments and suggestions. We also thank Ms. Lauren Koenig for editorial assistance. This work was supported by NIH grants NS050396 (BM) and U01 AI 061223 (DC), as well as the Vanderbilt Institute for Integrative Biosystems Research and Education and the Vanderbilt Brain Institute. Statistical and graphical support was provided by P30HD15052 (Vanderbilt Kennedy Center).

CHAPTER III

DIFFERENTIATION OF AFFECTED PATHWAYS IN THE MAMP – A STUDY OF CHOLERA TOXIN MECHANISM OF ACTION

Cholera toxin (CTx), secreted by the gram negative bacterium *Vibrio cholera*, causes the symptoms observed in cholera, a life-threatening infectious disease in the developing world.[72, 73] The seventh cholera pandemic that continues today began in the 1960s when the El Tor strain of cholera emerged as the most prevalent form of the disease.[72-74] This strain entered the Western hemisphere in 1991 in Peru and has since caused more than a million cases in Central and South America.[73] The animal reservoirs of *V. cholerae* are shellfish and plankton, and infection can be caused by consuming contaminated water or food.[72, 73] Those vibrios that survive passage through the stomach can adhere to the mucosal surface of microvilli of the small intestine where they secrete CTx[72, 73] as well as other toxins.[74] The concentration of vibrios on the mucosal surface rapidly increases from 10^7 to 10^8 cells per gram of tissue.[72] After an incubation period that can vary from 6 hrs to 5 days, the onset of symptoms is abrupt and is characterized by severe diarrhea that can reach a rate of 1 L/hr. This fluid contains large amounts of sodium, chloride, bicarbonate, and potassium, as well as mucus; the loss of these electrolytes causes blood volume depletion, low blood pressure, and shock.[72, 73, 75] The fluid loss can be so great that without proper rehydration, death can result within hours of onset.[72]

These clinical effects arise from the action of CTx on both the epithelial and nervous cells of the intestine. CTx is an 84 kDa hexameric protein (AB_5) consisting of a catalytic A subunit (A1 and A2 chains) and a pentameric B subunit. Each B subunit has a binding

site specific for a single ganglioside GM1 glycolipid with a total capacity of five for each CTx protein complex. CTxB binds tightly to GM1 receptors at the cell surface, and the glycolipid directs the toxin to the endoplasmic reticulum. It has been repeatedly demonstrated the GM1 receptors specifically bind CTxB.[76] Additionally, increasing GM1 receptors in cell membranes through incubation of cells with exogenous GM1 prior to CTx exposure has resulted in enhanced response and shortened lag period compared to control cells.[22, 26] After endocytosis, the CTx-GM1 complex is trafficked retrograde from the plasma membrane to early endosomes, the Golgi, and finally to the endoplasmic reticulum (ER) where the A1 chain of the toxin is able to utilize the ER-associated degradation pathway to enter the cytosol (Figure 15).[77] After separation, the A subunit is free to enter the cytosol.

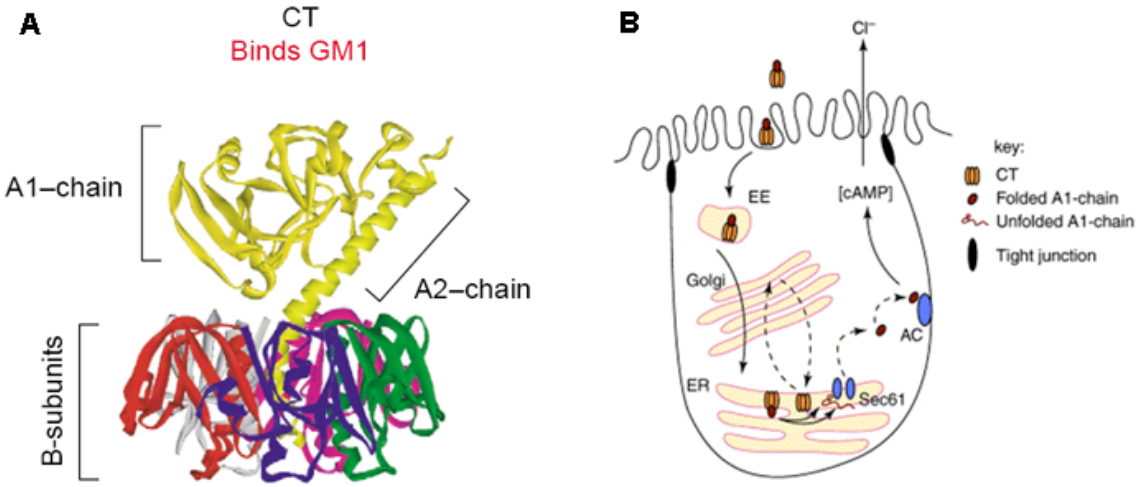

Figure 15. CTx Gains Access to the Cytosol Through Binding and Transport of CTxB to the Endoplasmic Reticulum.[78] (A) Both subunits of cholera toxin. (B) Transport of CTx through the cell, leading to cAMP activation and release of Cl^- ions in polarized intestinal epithelial cells.

The mechanism of action of CTx to activate cAMP production is well known. The A subunit of the toxin activates the heterotrimeric G-protein, GSα, via ADP-ribosylation. The modified Gsα loses its GTPase activity, but remains constitutively active in its GTP-bound state, causing a continuous stimulation of adenylate cyclase. Continuous adenylate cyclase activation results in excessive production of cAMP.[79] The result is the secretion of chloride ions from the cell which can be measured using electrophysiology. Time-course studies using this methodology indicate CTx takes approximately 30 min to increase intracellular cAMP and induce chloride secretion in the T84 intestinal epithelial cell line.[80] As shown in Figure 16, cAMP-dependent PKA is involved in several signaling pathways, all of which may be activated by continued cAMP production. This mostly commonly discussed downstream effects of this activation is increased Cl^- release.[16, 17]

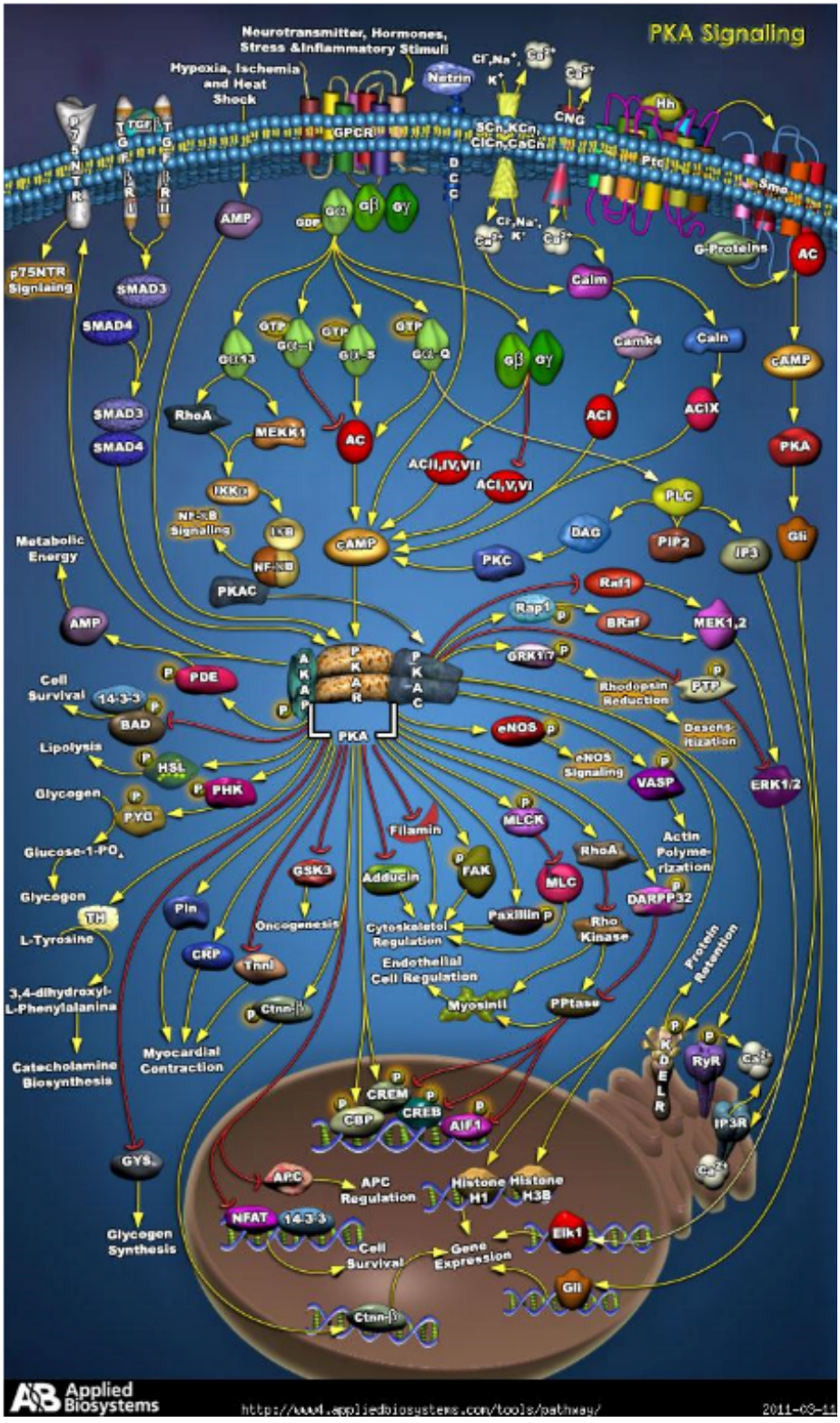

Figure 16.Signaling controlled by cAMP-dependent PKA.

An initial MAMP study of toxin effects on metabolism showed different metabolic processes were triggered in cell lines in response to botulinum neurotoxin A, ricin, and CTx. [6] After preliminary studies using a range of cell types (fibroblast, ovary, and hepatocyte, and intestinal), in tandem with literature that suggested the diarrheal response to CTx has a significant neurological component (up to 50%),[81] neuronal-like cells were chosen for more in depth study in the MAMP. PC-12 pheochromacytoma cells were selected as a useful neuronal model for our studies,[82] as they possess GM1 ganglioside receptors capable of binding CTx[83] as well as a demonstrated increase in cAMP production in response to forskolin, a direct activator of adenylate cyclase.[11]

Initial studies by Dr. Rachel Snider revealed that a single 2 min exposure to 100 nM CTx was sufficient to cause an increase in extracellular acidification and lactate production to 170% of basal levels (Figure 17). She hypothesized that the metabolic responses observed in these studies were due to increases in intracellular cAMP concentrations caused by continuous stimulation of adenylate cyclase.[6]

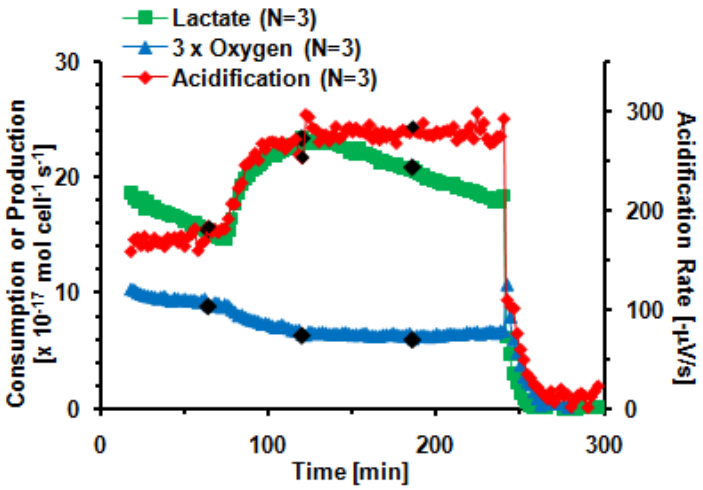

Figure 17. The average metabolic rates and acidification of PC-12 cells due to 100 nM CTx exposure. The average metabolic rate (mole·cell^{-1}·s^{-1}) of each stop-flow is shown. Oxygen is graphed as consumption, lactate is graphed as production, and acid production is graphed as the acidification rate. Cell necrosis is triggered at 220 min.

Dr. Snider then used H-89, a cAMP-dependent protein kinase inhibitor, to inhibit cAMP-activated protein kinase A (PKA), which is involved in the regulation of glycogen and lipid metabolism.[84] PC-12s were treated with 30 µM H-89 for 1 hr followed by a single 2 min exposure to 100 nM CTx (Figure 18). H-89 appeared to have successfully inhibited further lactate and acid increase, as no statistically significant changes occurred after CTx exposure. This suggested that the increase in lactate and acid production is mediated by PKA. However, during H-89 exposure, the oxygen consumption rate decreased to 50% of pre-exposure rates. Upon treatment with 100 nM CTx, the rate continued to decrease to 33 ± 3% of pre-inhibitory rate. This decrease is within the range expected for 100 nM CTx, however the results seem to indicate that this decrease was due to H-89 exposure. However, H-89 also inhibits a number of additional protein

kinases to 25% or less of their normal activity including MAPKAP-K1b, MSK1, PKBα, SGK, S6K1, ROCK-II, AMPK, and CHK1.[85, 86]

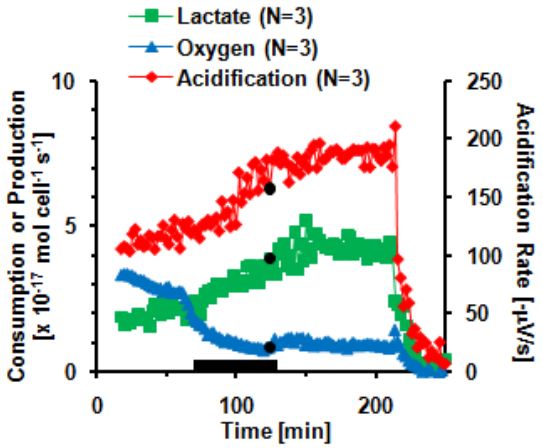

Figure 18. The average metabolic rates and acidification of PC-12 cells exposed to thirty minutes 30 µM H-89 (black bar) and a single two minute dose of 100 nM CTx (♦). 5 x 10^5 PC-12 cells were perfused with low-buffered 5 mM glucose RPMI for 60 min before H-89 was introduced. The average metabolic rate (mole·cell^{-1}·s^{-1}) of each stop-flow is shown. Oxygen is graphed as consumption, lactate is graphed as production, and acid production is graphed as the acidification rate. Cell necrosis is triggered at 220 min.

Inhibition with H-89 proved to be inconclusive, so additional inhibitors were applied to track the movement of CTx through the cell toward the ER and prove that the measured increase was in fact due to stimulation of adenylate cyclase by the CTx A subunit.

To investigate the proposed mechanism behind the metabolic responses to CTx, the cholera toxin B subunit (CTxB) and two inhibitors, oxamate and brefeldin A (BrA), were used. CTxB is structurally similar to CTx, retaining the ability to bind to ganglioside GM1 receptors and retrograde traffick back to the ER. It has been shown that CTxB is required for entry of whole toxin into the cell, and the cholera toxin A subunit (CTxA) is

only able to cause cAMP activation in cell lysates without transport by CTxB-GM1 complexes to the ER. While CTxB fails to induce toxicity without the catalytic A subunit, it has been shown to have its own effect on some cell lines. This includes differentiation of PC-12s upon CTxB exposure, and immediate (10 s) increase of intracellular Ca^{2+}, as well as induction of tyrosine phosphorylation.[22] Exposure to CTxB will demonstrate the increase in anaerobic respiration was not due to the entry and trafficking of the B subunit to the ER or cellular changes induced by CTxB exposure.

BrA reversibly disrupts vesicular transport in eukaryotic cell systems, thus preventing retrograde trafficking of the toxin to the ER and ultimately delivery of CTx A1 to the cytosol in epithelial and neuronal cell lines.[87, 88] If the observed response is due to interactions of whole toxin prior to retrograde trafficking to the ER and stimulation of adenylate cyclase, simultaneous treatment with BrA will not block the increase in acidification and lactate production upon CTx stimulation. However, if the increase in anaerobic respiration is due to stimulation of adenylate cyclase, treatment with BrA will prevent it by blocking toxin transport.

Finally, oxamate inhibits LDH, the enzyme which converts pyruvate to lactate and H^+. Our current hypothesis states that continuous activation of cAMP, leading to activation of PKA drives the increase in anaerobic respiration and the increase in co-release of lactate and acid into the extracellular space. However, extracellular acidification is a combination of products from anaerobic and aerobic respiration, as well as fluctuation in ion channels and other cellular processes. Treatment with oxamate during and after CTx exposure will demonstrate that the increase in extracellular acid is due to co-release of lactate, and not to changes in other pathways involved in cellular metabolism.

The following demonstrates the ability demonstrate the utility of the MAMP to investigate the underlying mechanisms for observed cellular metabolic responses to toxins through the use of inhibitors and other effectors.

Experimental

Chemicals and Instrumentation

All materials were used as obtained unless otherwise noted. CTx and the CTxB subunit from *Vibrio cholerae*, GOx (Type IIS from *Aspergillus niger*), BSA, glutaraldehyde (glutaric dialdehyde, 25 wt % solution in water), and oxamate were purchased from Sigma. Stabilized LOx was purchased from Applied Enzyme Technology (Pontypool, UK). Nafion (perfluorosulfonic acid-PTFE copolymer, 5% w/w solution in ethanol) andPt wire was purchased from Alfa Aesar. Sterile glucose solution and (L)-lactic acid were purchased from Fisher Scientific. Lyophilized alamethicin was obtained from A.G. Scientific, Inc. (San Diego, CA). Custom RPMI 1640 media modified to be 1 mM phosphate, bicarbonate-free, and glucose-free was purchased from Mediatech (Herndon, VA). All MAMP consumables including cell inserts, spacers, and membranes were obtained from Molecular Devices Corp. (Sunnyvale, CA).

Cell Culture

Loosely adherent rat pheochromacytoma cells (PC-12, CRL-1721.1 ATCC) were maintained in continuous culture in Corning CellBIND® flasks with F12K media (Mediatech, Inc.) supplemented with 15% donor horse serum and 2.5% FBS (Atlanta Biologicals, Inc), pH 7.40 in a 5% CO_2, 37 °C atmosphere. Subculturing was performed

by washing twice with Dulbecco's Phosphate Buffered Saline (DPBS) without calcium and magnesium salts from Atlanta Biologicals Inc., and then adding 4-6 mL of culture media to the flask. A cell scrapper was then used to remove cells from the collagen-coated flask. PC-12s were seeded 5×10^5 per insert in Corning Costar® Transwell® collagen coated cell culture inserts (PTFE, 3 μm pores) and allowed to grow overnight in growth media.

An adherent human epithelial hepatocellular carcinoma cell line (HepG2, HB-8065, ATCC), was maintained in continuous culture with Eagle's Minimum Essential Medium (EMEM) (Mediatech, Inc), supplemented with 10% FBS, pH 7.40 in a 5% CO2, 37 °C atmosphere. Subculturing was performed by washing twice with DPBS and rinsing the cells with .25% (w/v) Trypsin- 0.53 mM EDTA for 5 min at 37 °C. HepG2 cells were seeded 5×10^5 per insert in Corning Costar® Transwell® cell culture inserts (polycarbonate, 3 μm pores) and allowed to grow overnight in growth media.

Preparation of Solutions for Cholera Experiments

In all experiments modified RPMI 1640 media containing 5 mM glucose was used. CTx is sold by Sigma Aldrich as a lyophilized powder that is reconstituted as a 11.75 μM solution containing 0.05 M Tris buffer salts, pH 7.5, 0.2 M NaCl, 0.003 M NaN3, and 0.001 M sodium EDTA. For this reason, all experiments with CTx and controls were run with 5 mM glucose modified RPMI 1640 media supplemented to contain the appropriate concentration of these compounds.

Experimental protocol

Cells were seeded into inserts and allowed to adhere overnight. Once placed in the instrument, measurement of amperometric and potentiometric signals began. The cells were allowed to equilibrate for a period to determine their rate prior to exposure. The cells were treated with various inhibitors and toxins for a period of time, and then returned to the running media to allow a period of recovery prior to treatment with alamethicin. Alamethicin induced cell necrosis via the formation of voltage-gated pores in the cell membrane, causing the metabolic rates of all signals to rapidly decrease. This cell necrosis enables the determination of the effective zero metabolic activity level for calibrating the sensors and for conversion of the raw electrochemical data into metabolic rates of $mol \cdot cell^{-1} \cdot s^{-1}$. In all experiments the sensors were calibrated with modified RMPI media with no glucose and no lactate, with 0.05 mM lactate and 1 mM glucose, with 0.1 mM lactate and 3 mM glucose, with 0.2 mM lactate and 5 mM glucose, and in some cases with 0.3 mM lactate, before being returned to the running media.

Data Analysis

Acidification rates were determined by the Cytosoft program as described by Owicki.[36] Amperometric signals were analyzed by comparing the stop-flow results for live and dead cells. The current response of a given stop flow period, i_p, is defined as the difference between the steady state current and the current at the end of the stop flow. Data is then analyzed by subtracting the response with dead cells from the response with live cells to obtain the current response due to cellular activity, Δi_p.

The concentration in the chamber at the end of the stop flow is calculated from Δi_p using the calibration at the end of the experiment. By accounting for the microfluidic

volume, the number of cells present, and the length of the stop flow period, metabolic rates can be calculated in terms of $mol \cdot cell^{-1} \cdot s^{-1}$. Statistical analysis was performed by grouping stop-flow rates from each replicate chamber into basal, exposure, and various post exposure groups. Values are reported as average ± standard deviation. Statistical significance was determined by a two-tailed paired *t*-test with $p < 0.05$.

Results and Discussion

Metabolic Response of Hepatic Cells to Cholera Toxin

Multiple cell types, including intestinal, ovary, and hepatic cells, were exposed to CTx in the MAMP. As CTx is expected to stimulate cellular processes that increase ATP utilization, our initial goal was to identify cell lines in which CTx exposure resulted in an increase in extracellular acidification as measured by a conventional Cytosensor microphysiometer.

Based on these preliminary experiments, the multi-analyte metabolic response of hepatocytes to cholera was further explored. In this experiment, the basal metabolic rates of acidification, lactate production and oxygen consumption of 5×10^5 HepG2 cells were measured. At 82 min, the hepatocytes were exposed to 1000 nM CTx for 30 min, before returning control media to the cells. The cells were allowed to recover for 90 min before treatment with 101 μM alamethicin. Figure 19 shows the average metabolic rates of HepG2 cells as they were exposed to CTx. Three traces are shown, illustrating the calculated metabolic rates of lactate, oxygen, and acidification for each 2 min stop-flow cycle.

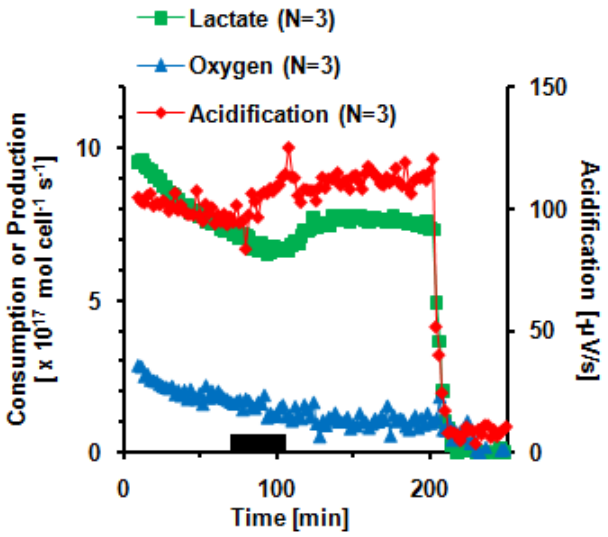

Figure 19. Average metabolic response of 5×10^5 HepG2 cells to 30 min exposure to 1,000 nM CTx. The black bar indicates the 30 min 1,000 nM CTx was being perfused through the cell chamber. Cell necrosis is triggered at 200 min.

Oxygen is graphed as consumption, with a decrease in rate indicating a decrease in metabolic consumption of oxygen. Lactate is graphed as production, with an increase in rate indicating a increase in metabolic production. Acid production is graphed as the acidification rate on the secondary axis, or slope of the change in potential during each stop-flow cycle in -µV/s, as provided by the Cytosensor software. Ten min after exposure, lactate production increased to 104 ± 4% from basal levels, however based on the rate of decrease in production prior to exposure; the actual effect on CTx on lactate production was probably larger. Acid production increased to 120 ± 8% during CTx exposure, and remained elevated until necrosis was triggered. No significant change was seen in oxygen consumption. This metabolic change was not as significant compared to the response of fibroblasts and neuronal cells. A study of CTx on fibroblasts had been performed previously,[6] and the hepatocytes were not as responsive or relevant as the

neuronal PC-12 cell line to the specific toxicological target in vivo of CTx, so all further MAMP experiments used PC-12 cells.

Comparative Metabolic Response of PC-12 Neurons to CTx and CTx B Subunit

To confirm that the metabolic response due to CTx exposure was caused by the irreversible activation of adenylate cyclase and production of cAMP, the metabolic changes caused by binding and internalization of the toxin had to be determined. To achieve this, the response of CTx was directly compared to that of CTxB, which binds to the GM1 receptors and trafficks to the ER. CTxB is know to cause differentiation in PC-12 cells, an immediate (10 s) increase of intracellular Ca^{2+}, as well as induction of tyrosine phosphorylation,[22] but does not have any inherent toxic ability.[76]

In order to confirm that CTx and CTxB subunit have different effects on the PC-12s, the exposure paradigm of three 2 min pulses spaced 1 hr apart two chambers of cells was used, with two chambers receiving 100 nM CTx and two chambers receiving 500 nM CTxB subunit; This experiment was performed twice. A five-fold increase in concentration of CTxB was chosen to be equivalent to the amount of CTxB in 100 nM CTx, which is comprised of five CTxB subunits for each CTxA unit.

Figure 20 compares the average metabolic response of both CTx and CTxB subunit for lactate production (Figure 20A), and oxygen consumption (Figure 20B), and acidification (Figure 20C). For CTxB, a gradual increase in lactate to 116 ± 4% and acid production to 118 ± 11% over the combined 3 hr exposure and recovery period can be seen, but does not cause the initial response seen in the CTx metabolic profiles. In addition, a smaller gradual change was seen in oxygen consumption due to CTxB with a decrease to 84 ± 6%. The decrease of oxygen due to CTx occurred within minutes of the first pulse, with

consumption reaching 53 ± 7% of basal rates at its peak, and 66 ± 6% of basal rates at the end of three hours. While cellular metabolism appears to be affected by the CTxB subunit, it is clear that the binding of the B subunit to the GM1 ganglioside is not the cause of the immediate changes seen when PC-12 cells are exposed to whole CTx. This supports our theory that the A subunit is reaching the cytosol and adenylate cyclase is getting stimulated without an appreciable lag-time. The changes due to CTxB may be a result of the previously discussed cellular changes induced by the protein, including differentiation.

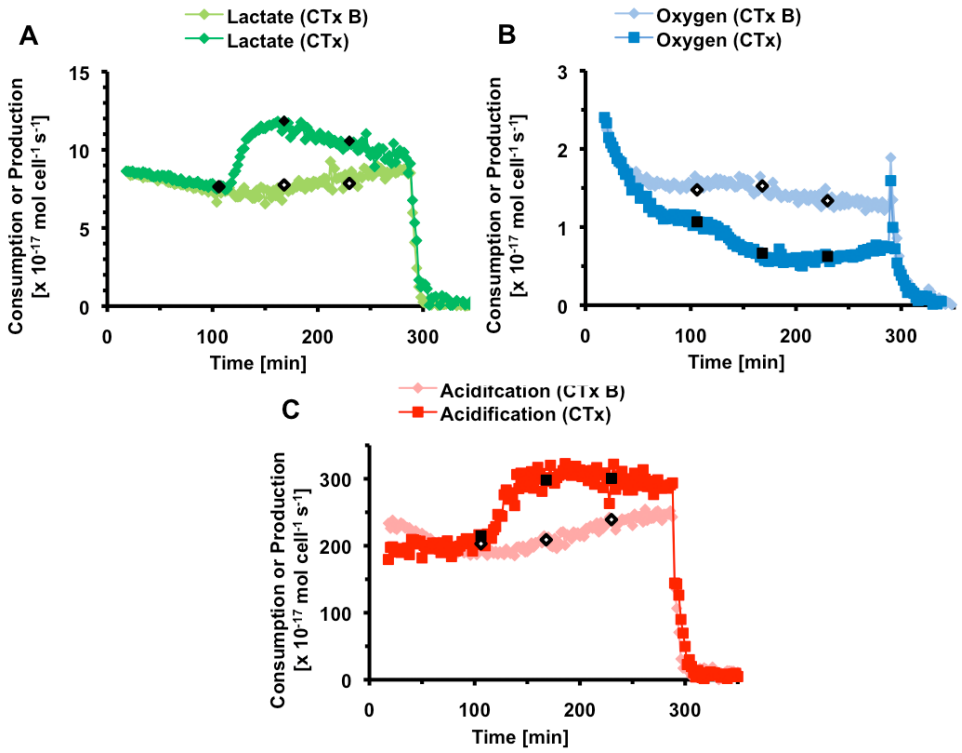

Figure 20. Average metabolic responses of PC-12 cells exposed to either 100 nM CTx or 500 nM CTxB subunit.Cell necrosis is triggered at 300 min. (a) Lactate production. The average of four chambers (♦) treated with three 2 min pulses of 500 nM CTxB (◊). The other trace is the average of four chambers (♦) treated with three 2 min pulses of 100 nM CTx (♦). (b) Oxygen Consumption. The average of four chambers (♦) treated with three 2 min pulses of 500 nM CTxB (◊). The other trace is the average of three chambers (■) treated with three 2 min pulses of 100 nM CTx (■). (c) Acid production. The average of four chambers (♦) treated with three 2 min pulses of 500 nM CTxB (◊). The other trace is the average of four chambers (■) treated with three 2 min pulses of 100 nM CTx (■).

Brefeldin A Successfully Blocks Transport of Cholera Toxin

After confirming that GM1 binding was not the cause of the switch to anaerobic respiration, BrA was used to disrupt vesicular transport and prevent retrograde trafficking of the whole toxin to the ER, thus preventing activation of adenylate cyclase and increase in cAMP in epithelial and neuronal cell lines (Figure 21).[87,88] In this experiment, two chambers were pre-treated with 1 µg/mL BrA for 30 min prior to 10 nM CTx exposure. Due to the inhibitor's reversibility, treatment continued throughout the course of the experiment, and can be seen in Figure 22. As shown, BrA successfully inhibited the increase in lactate and acid production.

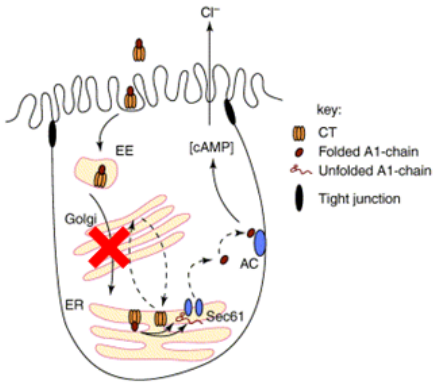

Figure 21. Brefeldin A Disrupts Trafficking to the ER. Treatment of cells with BrA blocks the ability of the CTx A subunit to reach the cytosol and stimulate adenylate cyclase.

No significant changes were seen in oxygen consumption. The metabolic rates of all three analytes of the control chamber receiving only BrA did not change in a statistically significant manner throughout the course of the experiment (data not shown), indicating that BrA does not have a measurable effect on cellular metabolism, unlike H-89.

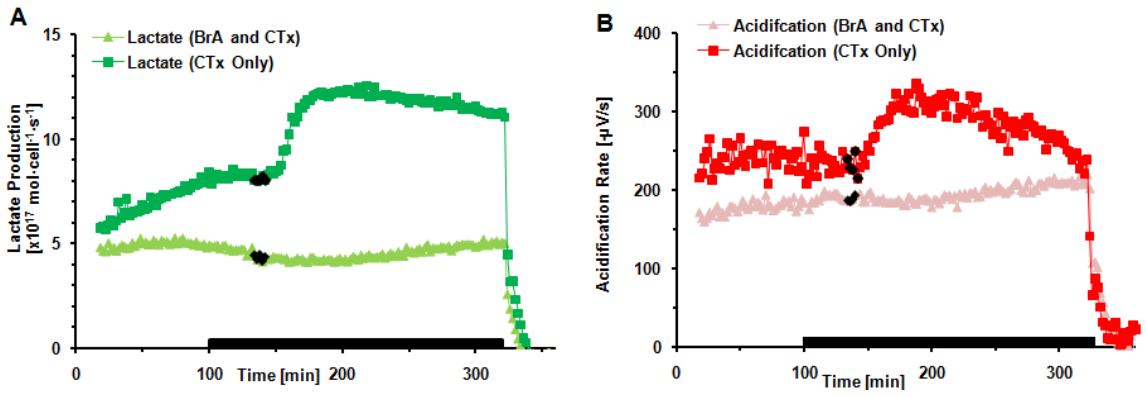

Figure 22The metabolic response of PC-12 cells pre-treated with 1 µg/mL BrA. Necrosis is triggered at 330 min. (a) Lactate production. One chamber (▲) treated with brefeldin A (black bar), and then exposed to ten minutes of 10 nM CTx (♦). The lactate sensor in the replicate chamber failed to calibrate, so N=1. The other chamber (■) received only CTx. (b) Acid production. The average of two chambers (▲) treated with brefeldin A (black bar), and then exposed to ten minutes of 10 nM CTx (♦). The other chamber (■) received only CTx.

Treatment with Oxamate Confirms That Acid Increase is Due to Anaerobic Respiration

Oxamate was used to confirm that changes in acid are roughly equivalent to lactic acid production. If inhibition of lactic acid formation causes an equal decrease in acid production, it indicates that other pathways affecting only acid production were activated by CTx. So far we have shown that vesicular transport and PKA activity are essential to cause the metabolic changes of CTx, which we have interpreted as proof of adenylate cyclase activation leading to cAMP production and a switch to anaerobic respiration. However, it is possible that other pathways are affected, which may cause acid to increase independent of lactic acid production. Oxamate can be used to inhibit the conversion of pyruvate to lactic acid via inhibition of lactate dehydrogenase. If acid production is increasing through another pathway, then acid production should not be inhibited as much as lactate production.

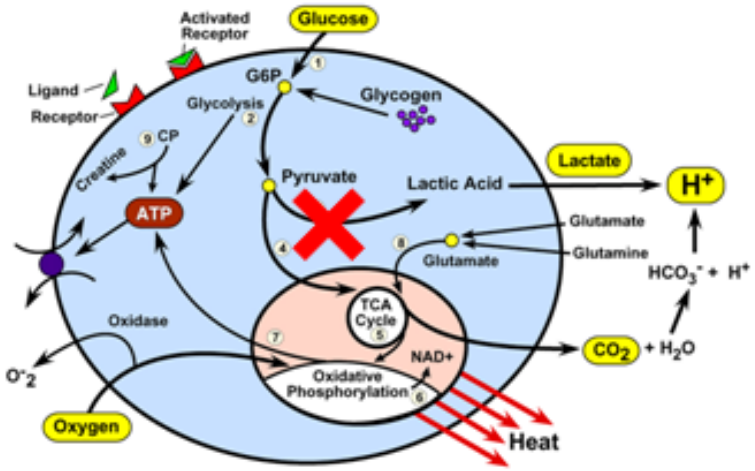

Figure 23. Oxamate Inhibits Lactate Dehydrogenase from Catalyzing the Conversion of Pyruvate to Lactic Acid. Treatment of Cells with Oxamate will show whether lactate and acid releases are coupled.

In this experiment, the cells are exposed to the 15 mM oxamate for 30 min prior to exposure, which was continued during a single pulse of 100 nM CTx and for 90 min after CTx exposure (Figure 24). As controls, one chamber received only CTx, and one chamber received only 15 mM oxamate. The remaining two channels received both oxamate and CTx. In these channels, lactate production was reduced to 36 ± 7% of basal activity and acidification was reduced to 39 ± 4%, suggesting that release of the acid and lactate are indeed coupled. Once the inhibitor was removed, lactate production increased to 134 ± 6% of basal rates and acidification increased to 126 ± 5% of basal rates. These increases in acid and lactate production were within the range of increases seen in the CTx-only control chamber at the same time point.

No change in oxygen consumption was observed during oxamate exposure, but was followed by a decrease to 42 ± 5% of basal levels after CTx exposure. As with lactate and acid, this change was not significantly different than the CTx-only control chamber. All of the rates in the oxamate-only control chamber returned to basal or near-basal rates (data not shown).

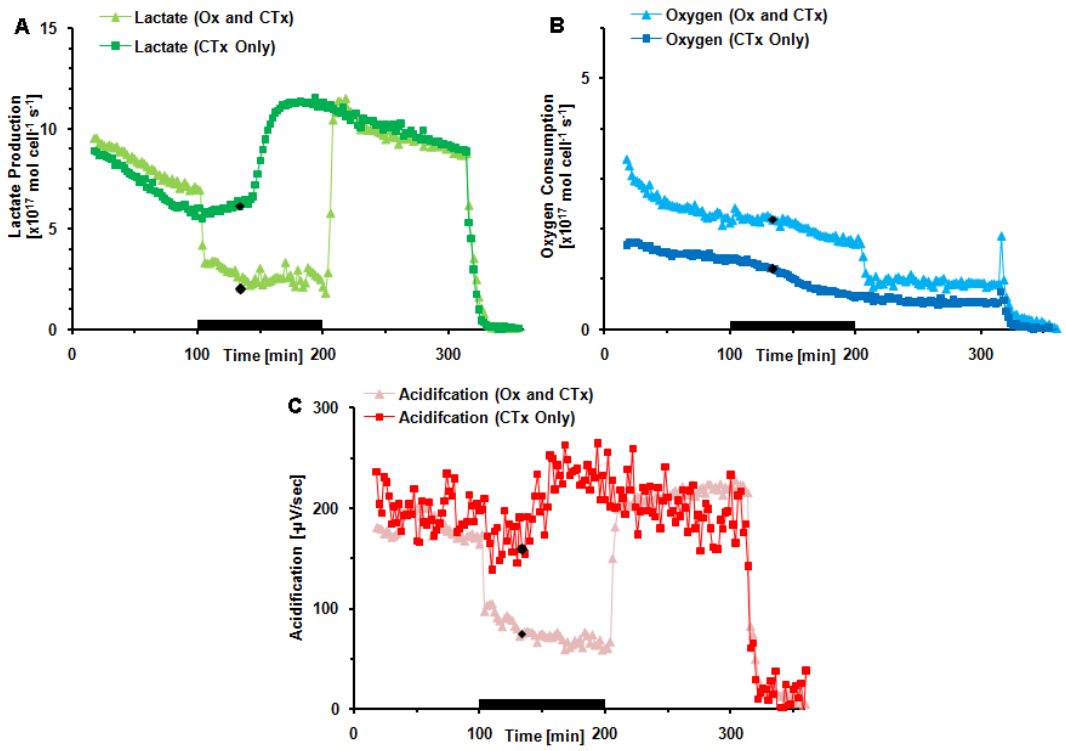

Figure 24.The metabolic rates and acidification of PC-12s pre-treated with 15 mM oxamate and exposed to CTx. 5 x 10^5 PC-12 cells were perfused with low-buffered 5 mM glucose RPMI for 100 min before Ox (black bar) was introduced and then exposed to a 2 min pulse of 100 nM CTx (♦). Oxamate was removed at 200 min to determine how lactate, acid, and oxygen rates would compare to the CTx-only control. Necrosis is triggered at 330 min. A) Lactate production. The average of two chambers (▲) treated with oxamate. The other chamber (■) received only CTx. B) Oxygen Consumption. The average of two chambers (▲) treated with oxamate. The other chamber (■) received only CTx. C) Acid production. The average of two chambers (▲) treated with oxamate. The other chamber (■) received only CTx.

Conclusions

Multianalyte microphysiometry was successfully used to determine the metabolic response of several cell types to CTx. When cells were treated with CTx, changes in cellular metabolism were seen in as little as 10 min as increases of extracellular acidification and lactate production, and decreases in oxygen consumption. Using the MAMP and targeting specific cellular functions with inhibitors demonstrated that cAMP production is the cause for this effect. The lack of immediate response of cells to the B subunit of CTx showed that binding of toxin to GM1 receptors was not the cause of the large changes in metabolism. Disruption of vesicular transport with brefeldin A showed that transport of the toxin to the ER is required for the metabolic response. These experiments together show that the metabolic response seen occurs only after the toxin has been transported. Inhibition of LDH with oxamate indicated that the increases in lactate and acid were coupled, and that other sources of acid from the cell were not responsible for the increases. These experiments show that the MAMP is a useful tool for determining the acute metabolic effects of biological toxins in real-time and for exploring the signaling pathways triggered by exposure to a toxin or other agent.

Acknowledgements

This work was supported by NIH grant U01 AI 061223, and the Vanderbilt Institute for Integrative Biosystems Research and Education.

CHAPTER IV

FOLLOWING AN INFECTION PATHWAY: THE EFFECTS OF SEB ON THE METABOLISM OF INTESTINAL AND IMMUNE CELLS

Staphylococcal Enterotoxin B (SEB), is one of thirteen toxins produced by the bacteria *Staphylococcus aureus* and is a category B toxin of interest to the Center for Disease Control (CDC). As defined by the CDC, a category B toxin, "can be easily spread, results in moderate illness rates, low death rates, and requires specific enhancements of CDC's laboratory capacity and enhanced disease monitoring."[19, 89] Ingestion of SEB by humans can result in food poisoning symptoms within 1 to 6 hrs of exposure, manifesting as acute salivation, nausea, and emesis, followed by abdominal cramps and diarrhea.[90] Inhalation has been shown to be more dangerous, with symptoms including fever, respiratory complaints, and gastrointestinal symptoms; severe intoxication results in pulmonary edema, shock, and death.[90] In laboratory exposure cases, most symptoms are resolved in 3 to 4 days. With the rise of *Staphylococcal aureus* resistance to the antibiotic vancomycin, as well as other common antibiotics,[91] metabolic studies to further understanding of the effects of SEB on the cellular level may help to elucidate new treatments.

Infection typically begins via ingestion of contaminated food leading to the release of *Staphylococcus aureus* toxins in the gut. SEB has been shown to activate the mitogen-activated protein kinase (MAPK) cascade, causing activation of the extracellular signal-regulated kinase (ERK1/2) and delayed activation of p38 in two different murine intestinal epithelial cell (IEC) lines.[91] Each of these pathways leads to activation of

transcription, and the synthesis of specific proteins, which would require an increase in ATP production to provide energy. In a study involving two other IECs, these pathways were activated, and an increased level of heat shock proteins Hsp 25 and Hsp 72 was observed, as well as altered jejunal architecture, increased chemokine synthesis, and immune cell activation.[24] The accumulated heat shock proteins were detected within 4 hrs of exposure, indicating that acute changes to IECs are occurring due to SEB exposure.

While production of these specific proteins may not be induced in all IECs, it is probable that similar pathways would become activated to produce specific proteins in response to the presence of SEB. For this reason, it is hypothesized that any IEC exposed to SEB would activate transcription of proteins, driving ATP synthesis, and resulting in increased metabolic flux, as measured by glucose and oxygen consumption, and acid and lactate production. Two IECs were chosen for this study, the human colorectal adenocarcinoma cell line, Caco-2, and the human colorectal carcinoma T84 cell line.

Superantigens (SAgs), such as SEB, often reach the immune system by transcytosing though epithelial cell membranes or traveling through damaged epithelium. At low doses, SEB reaches only the local T cells near the epithelium, but at high SEB levels, transcytosis rates increase, and are able to gain access to the systemic immune system, causing greater activation and damage.[19] Caco-2 contains bidirectional receptors which can transcytose SEB from either side of the intestinal wall (apical or basolateral).[18, 19] T84 cells form polarized cell walls, leaving receptors capable of transcytosing SEB only on the apical membrane of the cells.

Upon reaching the immune system, SEB may directly bind to Major Histocompatibility Complex Class II (MHC II) molecules expressed on antigen-presenting cells (APCs) to

be delivered to the Vβ region of T cell receptors (TCR). Typical antigens, which require processing by APCs prior to delivery to TCR, may bind to only 0.001% of the available TCRs, due to variability in the Vβ region.[92] SAgs can bind to up 20% of available T cells, resulting in overstimulation of the immune system, which contributes to the symptoms of SEB exposure. SAgs may also bind to the Vβ region of TCRs without direction by MHC II molecules, as have been shown in MHC II-negative mice.[27] The affinity for non-MHC II binding is much lower, and the use of MHC II helps the SAgs to overcome the affinity threshold for activation.

Immune cells, such a B cells and macrophages are common APCs. RAW 264.7 macrophages stimulated with interferon gamma (INF-γ) have been shown to upregulate production of MHC II molecules, improving their role as APCs.[30] Upon treatment with SEB, macrophages primed with INF-γ have been shown to increase F-actin production within 30 s.[20] F-actin is a vital component in the cellular cytoskeleton, and is important to early signal transduction. In this study, both normal and INF-γ stimulated macrophages were exposed to SEB with the hypothesis that toxin binding would lead to an increase in metabolic activity as the APC prepared to transport the toxin.

When SAgs, such as SEB, bind to the TCR, it stimulates massive T cell activation, resulting in cytokine release and cell death. The TCR is a heterodimer composed of α and β chains. As stated, antigens may only bind to a very small population of available TCR. This occurs because normal antigens need to bind to both the α and the β chains of the TCR. SAgs only need to bind to the β chain, and are able to bind to several variations.[93] Jurkats were chosen as a model immortalized T lymphocyte, and were exposed to SEB to induce changes in metabolism due to activation.

This study explores the metabolic changes that occur as SEB transcytoses through the intestinal walls, binds and is transported by APCs, and finally binds to T cells, initiating activation and production and release of harmful cytokines.

Experimental

Materials and Instrumentation

Lyophilized alamethicin was obtained from A.G. Scientific, Inc and reconstituted with 1 mL pure ethanol. Nafion® (perfluorosulfonic acid-PTFE copolymer was purchased from Alfa Aesar. LOx as purchased from Applied Enzyme Technology. Phosphate-buffered solution (PB; 50mM in phosphate, pH 7) and sodium chloride solid were obtained from Fisher Scientific. All cell culture media and supplements were purchased from Mediatech. All Cytosensor® materials were obtained from Molecular Devices Corporation (Sunnyvale, CA) or bought at auction. GOx, BSA, fraction V, 96%), and glutaraldehyde (glutaric dialdehyde, 25 wt % solution in water), and a 1 M L-(+)-Lactic acid standard were purchased from Sigma. Sterile 20% glucose solution was purchased from Teknova (Hollister, CA). Lyophilized SEB (98% purity) was obtained from Toxin Technology, Inc. (Sarasota, Fl) and reconstituted with 1 mL deionized water.

Cell Culture

Adherent human epithelial colorectal adenocarcinoma cells, (Caco-2, HTB-37, ATCC), was maintained in continuous culture with EMEM supplemented with 20% FBS, pH 7.40 in a 5% CO_2, 37 °C atmosphere. Subculturing was performed by washing twice with DPBS and rinsing the cells with 0.25% (w/v) Trypsin- 0.53 mM EDTA for 5 min at 37

°C. After subculturing, cells were concentrated via centrifugation for 5 min at 2000 rpm. Cells were then counted and seeded at a density of 4×10^5 cells per insert and allowed to grow overnight in growth medium.

Adherent human epithelial colorectal carcinoma cells, (T84, CCL-248, ATCC), were maintained in continuous culture with a 1:1 mixture of Ham's F12 medium and DMEM with 2.5 mM L-glutamine (Mediatech, Inc), supplemented with 5% FBS, pH 7.40 in a 5% CO_2, 37 °C atmosphere. Subculturing was performed by washing twice with DPBS, and rinsing the cells with 0.25% (w/v) Trypsin- 0.53 mM EDTA for 6 min at 37 °C. After subculturing, cells were concentrated via centrifugation for 6 min at 2000 rpm. Cells were then counted and seeded at a density of 5×10^5 cells per insert and allowed to grow overnight in growth medium.

Both epithelial cell lines were grown to confluence in 75 cm^3 flasks, and then transferred to 150 cm^3 flasks and grown to confluence to achieve enough cells for MAMP experiments.

The adherent mouse monocyte/macrophage cell line, (RAW 264.7, TIB-71, ATCC), was maintained in continuous culture with DMEM supplemented with 10% FBS, pH 7.40 in a 5% CO_2, 37 °C atmosphere. Subculturing was performed by washing twice with DPBS, and then adding 5 mL of culture media to the flask. A cell scrapper was then used to dislodge cells from the flask.

Macrophages were seeded at 2.5×10^5 in inserts and allowed to grow overnight in culture media. Alternatively, macrophages were seeded at 2.5×10^5 in inserts and allowed to grow for 48 h in culture media containing 200 U/mL INF-γ.

Non-adherent T lymphocyte cells (Jurkat E6-1 clone, TIB-152, ATCC), were maintained in continuous culture with ATCC-formulated RPMI-1640 Medium supplemented with 10% FBS, pH 7.40 in a 5% CO_2, 37 °C atmosphere. Subculturing was performed by transfer of 0.5-5 mL cell suspension to fresh media in a 75 cm^3 culture flask. Inserts were coated with 0.5 mL 10 µg/mL fibronectin (Invitrogen). After several hours, excess fibronectin solution was aspirated off, and cells seeded in the inserts at 5 x 10^5 cells per insert and allowed to grow overnight in culture media. If fibronectin coated inserts were prepared a day prior to cell seeding, coated inserts were stored overnight a 4 °C. Another adherence strategy was attempted by encapsulating the cells in an agarose droplet in the center of the cell culture insert. Jurkats were concentrated via centrifugation for 5 min at 2000 rpm and media was added to bring the cell density to 2 x 10^7 cells/mL. 300 uL of this cell suspension was added to 100 µL melted agarose to achieve 1.5 x 10^5 cells in a 10 uL drop at the center of the cell cup and allowed to solidify for 30 min. Modified RPMI was added to the cell cup and immediately placed in the instrument.

Preparation of SEB Solutions for the MAMP

Highly purified SEB was purchased in 1 mg amounts from Toxin Technology (Sarasota, Fl). Preliminary MAMP experiments showed massive decreases in acidification rate while toxin was perfused through the chamber. This shift was determined to be due to the increase in buffer with the addition of SEB to the running media. When 1 mg lyophilized SEB (98% purity) is dissolved in 1 mL of water, the resulting solution is 980 µg/mL SEB, 10 mM phosphate buffer, and 150 mM NaCl. Based on the buffer in the stock SEB solution, dilute solutions of SEB prepared in 1 mM phosphate buffered RPMI media were subject to a small increase in total buffer

concentration depending on the concentration of toxin added. If not accounted for, the increased concentration of buffer in dilute SEB solutions results in a shift in ECAR when introduced to the microfluidic chamber. To prevent this shift, additional buffer and NaCl were added to all other 5 mM glucose, 1 mM phosphate buffered RPMI media prepared for the experiment to be equivalent to amounts present in running media with SEB, and will be referred to as "adjusted RPMI". The total concentration of buffer and NaCl in adjusted RPMI was dependent of the concentration of SEB to be tested, and will not be discussed in further detail.

Experimental protocol

Cells were seeded into inserts and allowed to adhere overnight. Once placed in the instrument, measurement of amperometric and potentiometric signals began. The cells were allowed to equilibrate for a period to determine their rate prior to exposure. The cells were treated with various concentration of SEB for a period of time, and then returned to the running media to allow a period of recovery prior to treatment with alamethicin. Alamethicin induced rapid cell necrosis via the formation of voltage-gated pores in the cell membrane, leading to the release of intracellular contents. This cell necrosis enables the determination of the effective zero metabolic activity level for calibrating the sensors and for conversion of the raw electrochemical data into metabolic rates of $mol \cdot cell^{-1} \cdot s^{-1}$. In all experiments the sensors were calibrated with modified RMPI media with no glucose and no lactate, with 0.05 mM lactate and 1 mM glucose, with 0.1 mM lactate and 3 mM glucose, with 0.2 mM lactate and 5 mM glucose.

MTT Assays to Determine Maximal Response with Minimal Exposure Dose and Time for Caco-2

Caco-2 cells were the first studied in the MAMP in conjunction with SEB. As will be discussed in results, high dosages of toxin were required to elicit a metabolic response. MTT assays were performed to determine the minimal dose which would yield the maximal response due to SEB exposure for Caco-2 cells. This assay also helped to confirm that Caco-2s were undergoing changes due to toxin exposure. MTT assays were not performed with any other cell line.

For each specific exposure and recovery time, 100 µL of 4 x 10^5 Caco-2 cells/mL were added to 32 wells of a 96 well plate and the cells adhered overnight. The next day, cells were washed and the media was replaced with media containing either 500 ng/mL, 1 µg/mL, 10 µg/mL, 25 µg/mL, 50 µg/mL, 75 µg/mL, or 150 µg/mL SEB, with four replicates of each dosage. Control wells receiving no toxin, and wells containing only media were used. After the required exposure time, all media was removed from the cells and replaced with control media to begin the recovery period.

After the recovery time, 10 µL of 5 mg/mL MTT reagent was added to each well and incubated for 4 hours. The reducing power of the mitochondria of the cells is linked to the amount of MTT that is converted to insoluble formazan during incubation. After the 4 hour incubation, 100 µL of 0.04 N HCl in isopropyl alcohol was added to the cells to solubilize the formazan. The plates were then left in the dark for an additional 2 hrs.

Typically, absorbance could then be measured to achieve quantitative data for the assay; however, the SEB could not be removed from the approved location, and the use

of a plate reader was not possible. Instead, the relative intensity of the wells was observed to determine which cells had the highest mitochondrial activity.

Results and Discussion

Metabolic Effects of SEB on a Unpolarized Human Epithelial Intestinal Cell Line

The immortalized Caco-2 cell line was selected as the best candidate for exploring the metabolic effects of SEB due to its presence in the literature in conjunction with SEB, suitability for use in the MAMP due to adherence, and commercial availability. It was hypothesized that the transport of SEB into the cell would require excess energy usage, thus driving an increase in cellular metabolism. Preliminary experiments used toxin ranges from 1 ng/mL SEB to 1 µg/mL in short exposures (20 min), however no changes were observed. At this point, larger concentrations of toxin were used to see if a response could be elicited. Figure 25A shows the increase in lactate response in three different microfluidic chambers (Ch) when Caco-2 cells were exposed to 75 µg/mL SEB (Ch 1), 50 µg/mL SEB (Ch 2), and 25 µg/mL SEB (Ch 3) for 20 min. Cells receiving the largest dose increased lactate release 343 ± 52% over pre-exposure levels. Cells receiving the median dose increased lactate release 166 ± 12% over pre-exposure levels. No significant change was observed in Caco-2 cells exposed to 25 µg/mL SEB. Due to these encouraging results, another experiment was run where three replicates of the largest dose were performed (Figure 25B). In this instance, an increase of only 105 ± 1% in lactate release during SEB exposure was observed. After toxin was removed, lactate production did not remain elevated. In both experiments, sensors and solutions were

prepared in the same manner, but due to the demands of other projects, these two experiments were run months apart, and the changes observed must be due to differences in the cells themselves. No changes were made to the culture or plating methods and the relative passages were similar, with the first experiment performed with passage 38, and the second being performed at passage 31.

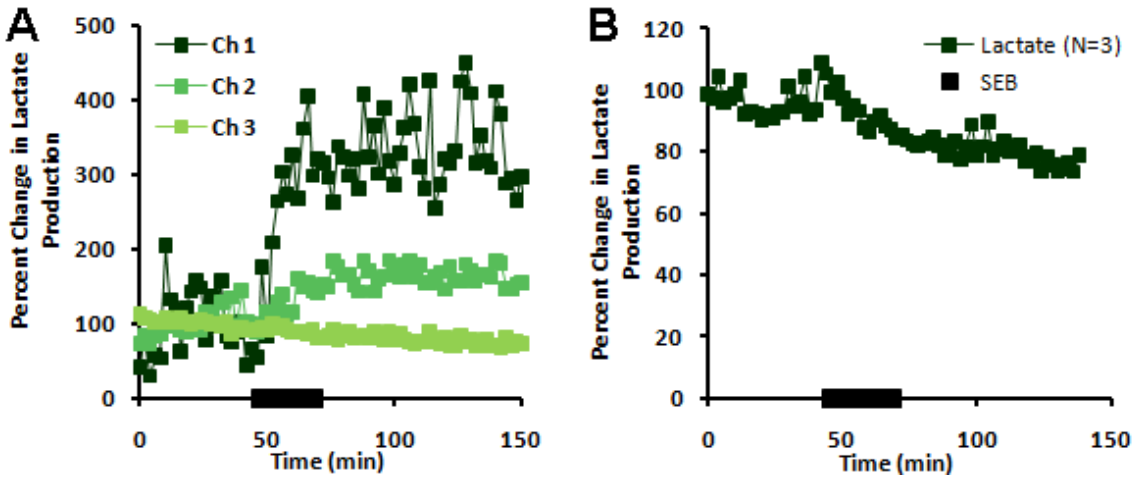

Figure 25. Percent Change in Lactate Release of the Caco-2 Cell Line from Two Independent SEB Exposures (A) Caco-2 cells were exposed to 75 µg/mL SEB (Ch 1), 50 µg/mL SEB (Ch 2), and 25 µg/mL SEB (Ch 3) for 20 min.(black bar) (B) Three channels of Caco-2 cells were exposed to 75 µg/mL for 20 min.

The extracellular acidification recorded during the two previously discussed experiments is shown in Figure 26. Again, Ch 1 received 75 µg/mL SEB, Ch 2 received 50 µg/mL SEB, and Ch 3 received 25 ug/mL SEB. During exposure to 75 µg/mL SEB in Ch1, ECAR increased to 120 ± 2% of pre-exposure rates. ECAR remained slightly elevated at 108 ± 5% of pre-exposure rates after toxin was removed, but is not significant when compared to the ECAR of the control chamber. A constant drift in the ECAR can

be observed, and is largely due to instrumental drift, although cellular changes may play a role as well. During the recovery period of the other chambers, the control chamber has an ECAR that is 109 ± 3% compared to basal rates. Therefore, the slight elevation of ECAR in the chamber receiving 75 µg/mL is likely due to instrumental drift, and is not significant.

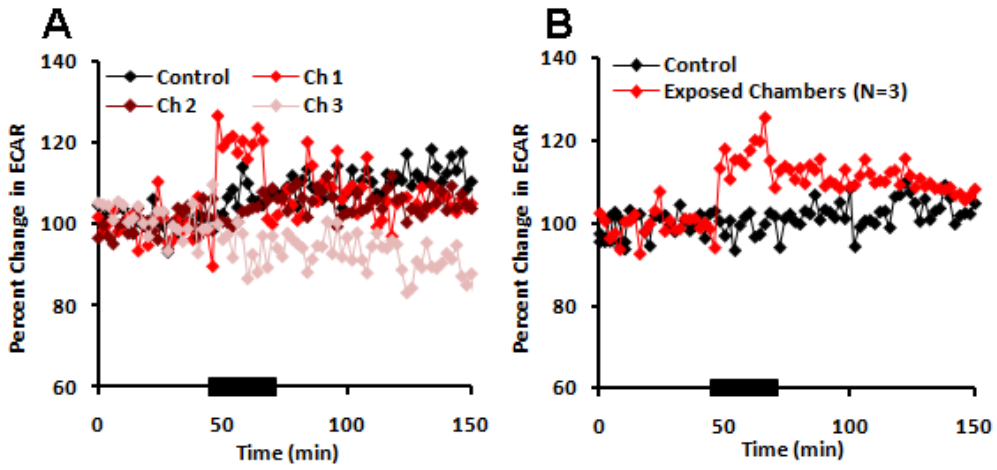

Figure 26. Acidification Response during Two Independent SEB Exposures on the Caco-2 Cell Line(A) Caco-2 cells were exposed to 75 µg/mL SEB (Ch 1), 50 µg/mL SEB (Ch 2), and 25 µg/mL SEB (Ch 3) for 20 min. (B) Three channels of Caco-2 cells were exposed to 75 µg/mL for 20 min.

This effect was seen again when the experiment was repeated (Figure 26B). Additional experiments over several cell lines suggest that the large increase observed when 75 µg/mL SEB is present is due to effects of SEB on the LAPS sensor. This could be due to actual interference of the protein, or due to difference in buffer. ECAR remains elevated to 113 ± 2% of pre-exposure rates for the 20 min after exposure. Unlike the previous experiment, the control chamber is not undergoing significant drift, and the ECAR is 101

± 3% of basal rates. This strongly suggests that although SEB does affect the sensor, there is some increase in cellular acidification due to SEB exposure.

This sensor effect at high concentrations of toxin made it was clear that exposure times and dosages needed to be optimized to achieve the maximal change in metabolism possible with the minimal dosage and exposure time. MTT viability assays were performed on the Caco-2 cell line covering seven doses between 500 ng/mL SEB and 150 µg/mL SEB, five exposure times between 1 and 24 hrs, and five recovery times between 1 and 24 hrs.

The darkest wells, or those with the highest activity, were those receiving the highest concentrations of toxin. It was found that if any recovery time was allowed, no wells appeared different than control cells, indicating that the activity of the mitochondria were only increased when toxin was present, and did not remain activated very long after toxin was removed. This is consistent with the hypothesis that IECs are activated as they transcytose SEB. Once removed, the transport ceases and activation is no longer required. Additionally, dosages below 50 µg/mL required over 3 hrs of exposure to achieve increased mitochondrial activity. To this end, MAMP experiments were performed with 6 hour exposures of 10 µg/mL and 25 µg/mL SEB. Despite the increased exposure times, the MAMP did not reveal any changes in metabolism due to toxin. While clearly activated as shown by the viability assays, the changes that occur in the Caco-2 cell line do not occur consistently, as evidenced by the dosages at 75 µg/mL SEB. Alternatively, metabolic changes are occurring, but are too small to be observed with the MAMP. This study could be continued if a lower noise MAMP was developed and if the cell culture could be normalized to yield consistent behavior.

Metabolic Effects of SEB on a Polarized Human Epithelial Intestinal Cell Line

Another cell line prominent in the study of SEB is the T84 intestinal cell line. These cells were plated at 5 x 10^5 cells/mL to achieve optimal ECAR between 100 and 200 - µV/s and exposed to 25 µg/mL SEB for 1 hr (Figure 27A). Within a few minutes of exposure a marked increase in lactate and acid release occurred. No change in glucose or oxygen consumption was observed.

After about 30 min of exposure, lactate acid production began to climb rapidly, as expected from metabolic activation. Lactate release increases to 125 ± 3% of basal rates and peaks at 116 min, before declining. ECAR increases to 147 ± 3% of basal rates and peaks at 106 min, before declining gradually.

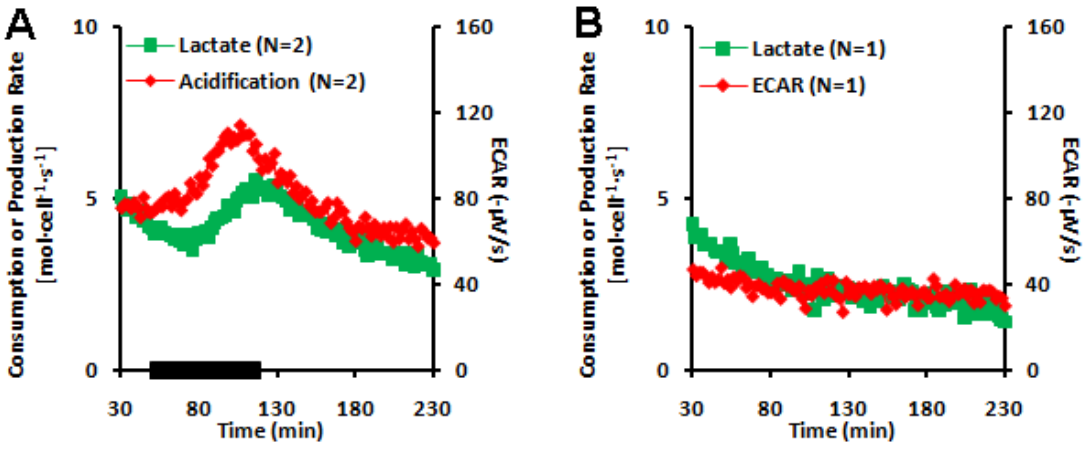

Figure 27. The average metabolic rates and acidification of T84 cells due to 25 µg/mL SEB exposure (black bar).The average metabolic rate (mol·$cell^{-1}$·s^{-1}) of each stop-flow is shown. Oxygen is graphed as consumption, lactate is graphed as production, and acid production is graphed as ECAR. (A) Exposed Chamber (B) Control Chamber

Two months later, a seed frozen down from the seed used in the previous experiments was brought back up, allowed to grow for over a week, and the experiment with 1 hr exposure of 25 µg/mL SEB was repeated (Figure 28). In this experiment, metabolic activation occurred within 10 min of SEB exposure. Lactate release increases to 159 ± 5% of basal rates and peaks at 90 min, before declining. ECAR increases to 172 ± 3% of basal rates and peaks at 86 min, before declining gradually. In this instance, the cells responded to SEB faster, and exhibited larger increases in lactate and acid production. These differences are most likely due to experiment to experiment variability in cell culture. It may be that the cells in the second experiment expressed more receptors for transcytosis of SEB, thus increasing the binding of toxin and cellular activation.

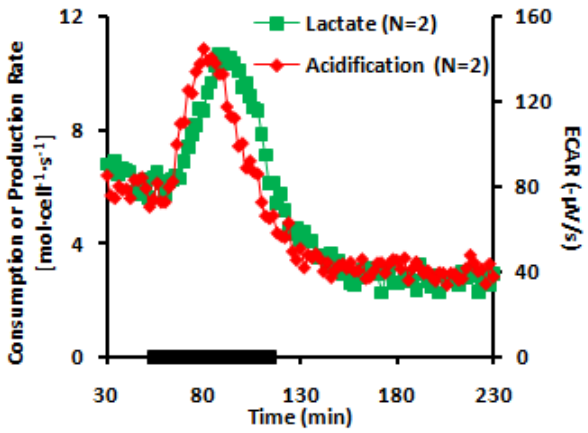

Figure 28 The average metabolic rates and acidification of T84 cells due to 25 µg/mL SEB exposure (black bar).The average metabolic rate (mol·cell^{-1}·sec^{-1}) of each stop-flow is shown. Oxygen is graphed as consumption, lactate is graphed as production, and acid production is graphed as ECAR.

The experiment was then repeated with 5 µg/mL SEB, and resulted in no changes. When the experiment was repeated with 20 µg/mL, the basal ECAR rates were much lower than observed in previous experiments. This prompted several attempts to improve

the cell culture of the T84 cell line to increase activity, including increasing growth time between passages, shortening incubation with trypsin during subculture, ordering fresh growth media, bringing up cells from storage, and ordering a new seed from ATCC. While these changes, most notably the increased time between subculturing, improved the ECAR of the T84 cells, no dosage and exposure time of SEB (from 1 μg/mL to 25 μg/mL) was able to elicit any changes in metabolism. Once again, the variations in cell passages and behavior led to inconsistent results while studying cellular metabolism in the MAMP with SEB.

Metabolic Effects of SEB on a Immune Cells

After exploring the metabolic effects of SEB on intestinal cell lines, where an increase in metabolic rates was expected due to transport of toxin, the metabolic effects of SEB on immune cells was explored. Naïve macrophages did not change metabolism due to toxin exposure, although the sensor effects on the LAPS were once again observed. RAW 264.7 macrophages were then seeded and primed with INF-γ for 2 days prior to 20 min exposure to 75 μg/mL SEB. As shown in Figure 29A, all three replicate chambers exhibited an increase in ECAR of approximately 120%, which has been shown to be due to the effect of the toxin on the LAPS. Figure 29B shows the small increase in ECAR when INF-γ stimulated macrophages from the same cell seeding respond to treatment with the bacterial protein, LPS. Successful activation of INF-γ stimulated macrophages with LPS demonstrates that the cells were indeed primed to maximize activation upon treatment with a bacterial toxin. Lack of response due to SEB exposure suggests that RAW 264.7 macrophages, a well studied murine cell line, to not undergoing measurable metabolic activation when treated with SEB.

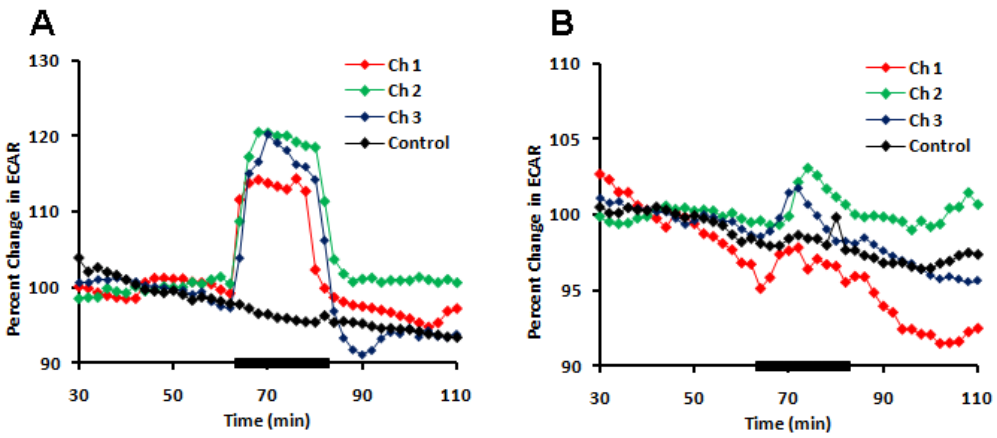

Figure 29. INF-γ stimulated macrophages treated with SEB or LPS. 2.5 x 10^5 RAW 264.7 stimulated with INF-γ for two days (A) Macrophages were treated with 75 µg/mL SEB for 20 min beginning at 66 min. (B) Macrophages were treated with 10 µg/mL LPS for 20 min beginning at 66 min.

Another immune cell line was explored, the non-adherent T lymphocyte Jurkat. It is unclear what the immediate metabolic effects of SEB on Jurkats may be, as toxin binding leads to T cell activation to produce cytokines, as well as T cell deletion.[94] Cells were seeded on fibronectin-coated cell cups and the metabolic rates measured during a 90 min exposure to 75 µg/mL SEB. Upon treatment with toxin, metabolic activity began to decrease in all analytes. As this dosage was obviously very potent, and resulted in rapid decline of cellular metabolism, experiment was then repeated using only 25 µg/mL SEB The exposed cells are shown in Figure 30A, while the control chamber is shown in Figure 30B. Within 30 min, the metabolic activity of the Jurkats dropped to null levels as seen with the higher dosage, suggesting cell death. The cells failed to recover after toxin was removed.

The experiment was then repeated with cells receiving 120 min exposure of 5 µg/mL SEB. In this instance, exposure to SEB failed to elicit a response. After several attempts

at recreating the successful experiment, the cells failed to achieve ECAR high enough to run the MAMP. Experiments using only the LAPS were attempted until this issue could be resolved. Visual inspection revealed that the Jurkats did not appear to be adhering to the fibronectin layer, so another method of adhering cells to the cell insert was attempted.

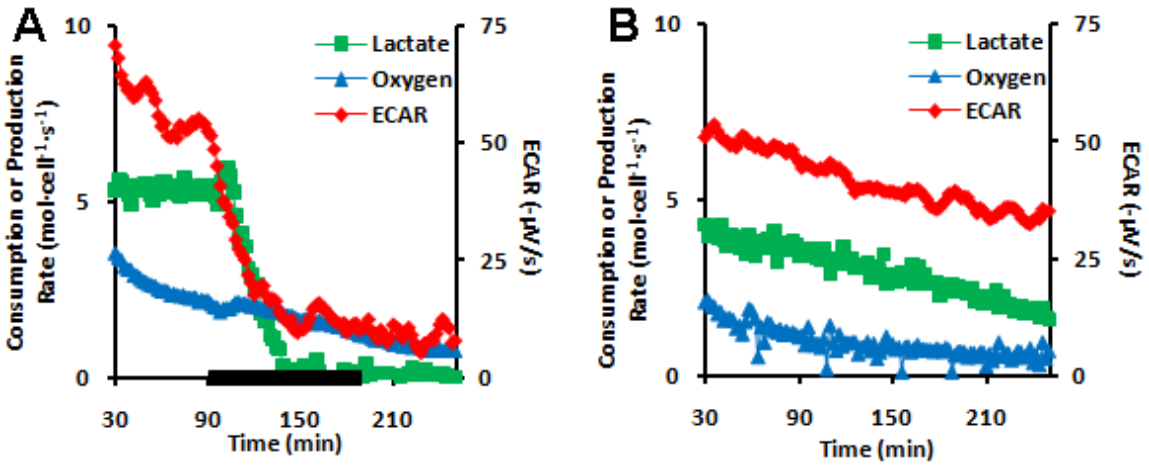

Figure 30. The average metabolic rates and acidification of Jurkats due to 25 µg/mL SEB. exposure (black bar). The average metabolic rate (mol·cell^{-1}·s^{-1}) of each stop-flow is shown. Oxygen is graphed as consumption, lactate is graphed as production, and acid production is graphed as ECAR. (A) Exposed Chamber (B) Control Chamber

Jurkats were encapsulated in an agarose/media mixture sold by Molecular Devices. Figure 31 shows the ECAR of two control chamber, two chambers receiving 10 µg/mL SEB (Ch 2, Ch 4), and two chambers receiving 25 µg/mL SEB (Ch 1, Ch 3). The agarose did allow for steady ECAR to be measured, but once again, no changes were seen in metabolism due to SEB exposure.

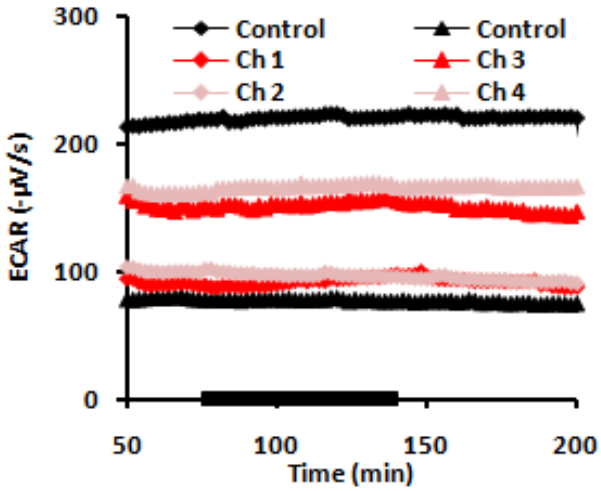

Figure 31. Jurkats Encased in Agarose and Exposed to SEBfor 1 hr (black bar). ECAR of two control chambers, two chambers receiving 10 µg/mL SEB (Ch 2, Ch 4), and two chambers receiving 25 µg/mL SEB (Ch 1, Ch 3).

Conclusions

Both the Caco-2 and T84 intestinal cell lines responded to SEB exposure by increasing production of lactate and acid due to exposure. This supports the original hypothesis suggesting that transcytoses through the intestinal cells would lead to increased demands on the cell, in this case causing an increase in anaerobic respiration. If consistent changes in metabolism could be achieved, further study of SEB-epithelial interactions could have been performed, including blocking SEB from binding with the trancytosis receptor expressed on the cellular membrane.

Naïve and INF-γ stimulated macrophages did not exhibit any immediate changes to cellular metabolism due to treatment with SEB. Treatment of INF- γ stimulated macrophages with LPS, another bacterial toxin known to induce activation in

macrophages,[25] did elicit an increase in extracellular acidification, proving that the macrophages were successfully primed. While RAW 264.7 macrophages did not respond to SEB with a change in cellular metabolism, it is possible that another macrophage or B cell line may be more responsive. In future studies, cell line selection could include human, as opposed to murine, macrophages, which have been shown to have a stronger response to SEB exposure.[28]

Jurkats were chosen as a model T lymphocyte due to its extensive use in the VIIBRE program. Additional T cells should have been selected to exposed SEB to cell lines with different Vβ regions on the TCR. Additional literature searches suggest the Jurkats possess the Vβ 8,[95] which is responsive to staphylococcal enterotoxin E rather than any of the other SAgs produced by *Staphylococcal aureus.*[93]

Acknowledgments

This work was supported by NIH grant U01 AI 061223, Defense Threat Reduction Agency grant HDTRA1-09-1-0013, the Vanderbilt Institute for Integrative Biosystems Research and Education, and DOE fellowship Graduate Assistance in Areas of National Need.

CHAPTER V

DEVELOPMENT OF THE NEXT-GENERATION MAMP BASED ON MULTIANALYTE SCREEN-PRINTED ELECTRODES

Real-time monitoring of cellular metabolism has the potential to enhance the knowledge gained from traditional toxicology by providing the rapid detection of metabolic changes as they occur, rather than waiting hours or days as the status quo mandates.[96] Performing these studies in a microfluidic environment increases sensitivity by allowing smaller changes in analyte concentrations to be seen and reduces required amounts for costly materials. To this end, the MAMP was developed and has been applied to the detection of insulin secretion from pancreatic islets,[97] the discrimination of toxins based on their metabolic effects,[6] studying the metabolic pathways affected by cholera toxin exposure,[7] and the effects of glucose deprivation on neuronal metabolism.[8]

The appeal of studying cellular metabolism with the MAMP is that it allows for an endless list of possibilities, including the exploration of metabolic flux of bacteria or screening potential drug targets. In order to meet the demands of future research, it is necessary to adapt the MAMP for a wider range of studies, as well as miniaturize and improve sensitivity.

In order to improve the capabilities of the MAMP, a new platform is needed to reduce noise, allow for a wider range of studies, and allow for simplified, high-throughput experiments. The LAPS technology on the Cytosensor measures at a high frequency, while the potentiostat used to amperometrically measure glucose, lactate, and oxygen measures at a lower frequency. The combination of the two technologies results in

electronic noise due to cross-talk between the instruments. The combination of multichannel potentiometric and amperometric detection in one multi-chamber potentiostat (Appendix A) will allow all four analytes to be measured with the same instrument, eliminating noise due to cross-talk. Moving away from the Cytosensor-based MAMP opens up many novel platform options for multi-analyte detection.

Screen-printed electrodes (SPEs) have found utility in environmental and food analysis methods due to their simple fabrication, versatility, high reproducibly, and low-cost.[98] In addition, SPEs are planar, simplifying the creation of suitable housing for a microfluidic chamber. Screen-printing is possible on a variety of substrates, including paper, plastic, glass, wood and ceramics, and electrodes can be created using many conductive materials, including carbon, platinum, and gold.[99, 100] This fabrication process means that almost any electrode design can be created with high spatial control at low cost, making possible the creation of a sensor that can detect glucose, lactate, oxygen, and acid simultaneously.

The conductive layer is printed onto the substrate through the use of a stencil to create the electrode design. The remaining steps are to modify the conductive surface with a sensing element and to insulate the rest of the conductive surface to protect against reactions away from the electrode area. Typically, if a carbon paste is to be applied to the conductive surface, it would be beneficial to screen-print the entire surface to ensure smooth and consistent layers before applying an insulating layer.[100] In the case of ceramic or polymer-insulated electrodes, coating prior to insulation may damage the sensing layer, and should be applied prior to sensor modification.

One such ceramic electrode was designed by Pine Research Instrumentation using a 3-electrode configuration (working, counter, and reference electrode) available with screen-printed platinum electrodes. The electrodes are fabricated by printing platinum ink onto a ceramic substrate, and then printing a protective ceramic layer to define the exposed area of the electrodes. A Ag/AgCl reference was formed by plating silver unto the platinum surface.

Towards the goal of creating a next-generation MAMP, a SPE with five modifiable platinum electrodes was designed to be printed by Pine. Four of the electrodes were modified to measure key analytes of the cellular energy cycle, where glucose, lactate, and oxygen were measured amperometrically and pH was measured potentiometrically via a pH-sensitive metal oxide film. The remaining electrode was modified as a Ag/AgCl quasi-reference. Alternatively, this electrode was left unmodified to be used as a counter electrode, with an aqueous Ag/AgCl reference placed downstream of the microfluidic chamber.

Using a custom designed SPE, glucose, lactate, and oxygen will be measured as with the current MAMP. However, it is not possible to use the LAPS technology to monitor pH changes with a SPE, so other options were explored. In order to create a true on-chip system, the pH electrode must use the remaining platinum electrode of the multi-analyte SPE. Glass electrodes are most commonly utilized for pH detection; however, they are not suitable for this platform. Ion-selective field effect transistors (ISFET) are another option, but would require the use of silicon dioxide, not platinum.[66] Metal/metal oxide films are commonly used to detect pH, the most common being antimony and iridium oxide.[64] Antimony electrodes have been shown to be suitable for pH detection, as they

can be easily fabricated, and some methods have lead to pH sensors with fast response times and stable potentials.[64] However, the disadvantages of antimony in physiological systems include sensitivity to oxygen concentration changes, the presence of carboxylic and amino acids, and temperature changes over the physiological range.[101]

In contrast, IrOx has been shown to be successful in physiological systems.[64, 65] There are multiple techniques that can be used to form IrOx films onto conductive substrates, including sputter deposition, thermal oxidation of iridium salt or wire, electrochemical oxidation of iridium onto electrodes using potential cycling, anodic iridium oxide film electrodeposition in galvanostatic mode, and simply applying a potential until a film of desired thickness is formed.[66] The electrochemical methods are preferable because the films can be formed on non-iridium substrates, such as carbon or platinum, without restrictions on the shape or design of the substrate, and only require minimal amounts of iridium to form the film.[66, 67] In addition, the techniques can be performed at room temperature and do not require working with brittle and expensive iridium wire.

Anodically electrodeposited iridium oxidation films (AEIROFs) have been reported using numerous methods, including cycling potential or current, or holding current or potential constant.[64, 66, 67] Differences in solution preparation, electrodeposition methods, and substrate results in variations in the formed iridium film, therefore care should be taken to choose the method that is appropriate for the sensor. The mechanism of response of IrOx films to pH changes is as shown in Equation 3,[102] where the values of n, q and r vary with oxide preparation, and are not usually integers:

Equation 3 $\text{Ir(IV) oxide} + q\text{H}^+ + n\text{e}^- \leftrightarrow \text{Ir(III) oxide} + r\text{H}_2\text{O}$

In addition to a new sensor platform, independence from the Cytosensor-based MAMP necessitates an alternate system that will allow for pumping, temperature control, and cell housing. Most microfluidic systems employ poly(dimethylsiloxane) (PDMS) for the microfluidic housing. PDMS is widely used due to its many advantages, as it is inexpensive, flexible, and optically transparent.[103] Liquid PDMS is formed from the mixture of a prepolymer and curing agent, which is then poured to form the desired device. Masters formed from deposition of SU-8 on silicon wafers allow for the formation of a wide variety of devices and channels. The compound is further desirable in biological applications as it is impermeable to water, nontoxic to cells, and permeable to gases, allowing for additional oxygen exchange for cells within the chamber.[104] Microfabrication techniques employing PDMS as novel bioreactors could be designed to meet the needs of the next-generation MAMP. To achieve real-time analysis, the cells will need to be adhered to the roof of the chamber.

Cell culture on PDMS has been successful, including culture on unmodified PDMS, plasma-treated PMDS, as well as PDMS treated with various adhesion agents, such as collagen, fibronectin, and poly-L-lysine.[105-107] Situating cells onto PDMS directly over the electrodes will form the next-generation MAMP based on SPEs. Once the SPE is integrated into a microfluidic device and all parameters optimized, the system will be validated by comparison to the current MAMP.

Experimental

Materials

Lyophilized alamethicin was obtained from A.G. Scientific (San Diego, CA). Nafion® (perfluorosulfonic acid-PTFE copolymer, 5% w/w solution) and Ir(IV) chloride (99.95 %) were purchased from Alfa Aesar (Ward Hill, MA). Stabilized GOx and stabilized LOx were purchased from Applied Enzyme Technology (Pontypool, UK). PDMS elastomer composed of prepolymer and curing agent (Sylgard 184 kit) was purchased from Dow Corning (Midland, MI). White epoxy was Hysol Epoxi-Patch from Dexter and silver epoxy was from Epoxy Technology, Inc. (Billerica, MA). Potassium chloride, phosphate-buffered solution (PB; 50 mM in phosphate, pH 7), sodium chloride, potassium carbonate, oxalic acid dihydrate, sodium hydroxide, potassium ferricyanide, sulfuric acid, and 30% hydrogen peroxide were obtained from Fisher Scientific (Pittsburg, PA). All cell culture media and supplements were from Mediatech and the Vanderbilt Cell Culture Core. All Cytosensor® materials were purchased from Molecular Devices Corporation (Sunnyvale, CA). BSA, and glutaraldehyde (glutaric dialdehyde, 25 wt % solution in water), and a 1 M L-lactic acid standard were purchased from Sigma (St. Louis, MO). Sterile 20% glucose solution was purchased from Teknova (Hollister, CA). Technic Silver Cy-less II electroplating solution was obtained from Technic Inc (Cranston, RI).

Design and Characterization of the Multi-analyte SPE

Preliminary research was performed with the Pine Research Instrumentation single-analyte SPE. A Pt SPE containing five electrodes was designed using the AutoCAD

design program, and was designed by melding components of the MAMP sensor head and the commercial sensor. The SPE features three Pt disk electrodes with areas of 1.8 mm^2 intended for glucose, lactate, and pH detection, one band electrode with a total area of 0.08 mm^2 intended for oxygen detection, and an electrode with an area of 19 mm^2 to be modified to act as a Ag/AgCl quasi-reference in a 2-electrode system or a counter coupled with an external or downstream Ag/AgCl (2 M KCl) aqueous reference. The electrode was printed by Pine Research Instrumentation. The areas of the three disk electrodes are defined by the insulating ceramic layer. Due to the small area of the oxygen electrode and the 100 μm resolution of the ceramic printing process, the oxygen electrode area was not defined by the ceramic layer.

The SPE consists of three layers; a ceramic substrate, a printed Pt layer, and a printed insulating glass layer. A VEECO Profilometer was used to determine the thickness of each layer, as well as the contours of the sensor, in order to design an effective microfluidic chamber. The thickness of the following items was measured: isolated Pt contacts, the insulating layer covering the Pt circuits, the height difference between the glass layer and the Pt disk electrodes, the thickness of the glass layer and metal layer around the larger Pt electrode, as well as the thickness of the Ag/AgCl layer of a fabricated reference.

Cyclic voltammetric measurements were carried out using a CHI 660A electrochemical analyzer (CH Instruments, Inc., Austin, TX). The four working electrodes were scanned in 5 mM ferricyanide with 100 mM KCl at a scan rate of 0.1 V/s. The largest electrode on the SPE was used as a counter electrode, and measurements were against an external Ag/AgCl (2 M KCl) reference electrode.

Formation of Ag/AgCl quasi-reference

Initially, a quasi-reference was desired to incorporate a reference electrode into the microfluidic chamber. To achieve this, the Pt electrode with an area of 19mm^2 was electrochemically cleaned by cycling in 0.5 M sulfuric acid. The SPE was immersed in Technic Silver Cy-less II electroplating solution, and a chronopotentiometry program was used to reduce Ag onto the electrode surface with a current density of 7 mA/cm^2 for 80 s. A Ag/AgCl quasi-reference was formed by anodizing the Ag electrode in 1M KCl for 120 s. The sensors were stored for 2 to 3 days in PB with 100 mM KCl to stabilize the reference. The stability of the reference was determined by monitoring the OCP against a Ag/AgCl (2 M KCl) reference using a CHI 660A. The newly formed reference was then used to electrochemically clean the SPE working electrodes by cycling in 0.5 M sulfuric acid, as well as taking CVs of the working electrodes in 5mM $FcTMAPF_6$ with 100 mM KCl for ionic strength, in order to test the reference's effectiveness. When not in use, each sensor is stored in the dark in PB with 100 mM KCl at room temperature to maintain reference stability.

Preparation of Enzyme Films for Planar Electrodes.

Enzyme films were prepared similarly to those previously described.[7, 42] To extend sensor lifetime, stabilized GOx was used instead of GOx. Briefly, 4 mg of GOx was dissolved in 700 µL of the BSA-buffer solution described in previous chapters, then quickly mixed with 7 µL of 25% glutaraldehyde. 1.8 mg of LOx was dissolved in 100 µL of a BSA-buffer solution then quickly mixed with 0.8 µL of 25% glutaraldehyde. Electrode films were cast by allowing a droplet of the enzyme solution to dry on the

platinum electrode surface. A droplet of the 5% Nafion solution was also applied to the oxygen electrode to reduce biofouling as shown in the literature.[41, 71, 79]

Calibration of Electrodes in Bulk Solution

GOx and LOx film electrodes were calibrated amperometrically by stepwise addition of glucose or lactate solutions to low-buffered no-glucose RPMI (pH 7.40, 1 mM PO_4^{3-}). The glucose biosensor was calibrated between 0 mM and 5 mM with 0.5 mM steps and the lactate biosensor was calibrated between 0 mM and 0.3 mM with 0.03 mM steps. Time stability studies were performed with each sensor. Once the electrode was coated, calibrations were performed periodically. When not in use, the sensors were stored at 4 ºC in the low-buffered RMPI.

Iridium Oxide Synthesis and Electrode Fabrication

The synthesis described to create the IrOx solution was adapted from Ges.[66] 75 of mg $IrCl_4$ was dissolved in 50 mL of deionized water and stirred for 15 min. 500 µL of 30% H_2O_2 was added, then stirred for an additional 10 min. 250 mg oxalic acid dihydrate was then added and stirred for 10 additional min. Potassium carbonate was then added to adjust the pH of the iridium oxalate solution to 10.50. The solution was stored in an amber bottle at room temperature for 3 days to allow the solution to stabilize. The solution was then stored at 4 ºC for up two weeks, and filtered with a 0.2 µm syringe filter prior to electrodeposition.

Initially, it was attempted to form IrOx films using the galvanostatic method described by Ges et al. In this method, the electrode was held at a current density of 1.5 mA/cm^2 for 500 s. Eventually, a constant potential method was adopted where the electrodes were electroplated with IrOx by holding the potential constant for a period time. Films were

attempted at +0.45 V, +0.55 V, and +0.6 V. Additionally, film formation times of 7 min, 10 min, and 15 min were attempted.

The potential was set at +0.6 V *vs* Ag/AgCl (2 M KCl) for 420 s using the CHI 660A potentiostat. A Pt wire mesh was used as a counter electrode. In later experiments, the electrodes were first preconditioned by holding the potential at -0.6 V *vs* Ag/AgCl (2 M KCl) for 60 s prior to electroplating at + 0.6 V. After film formation, the sensor was stored in 50 mM PB with 100 mM KCl for 2 days at 4 °C to stabilize. While cold storage is not necessary for film stabilization, the lifetime of SPEs also containing enzyme films were extended by this storage method, so it became standard for any modified SPE.

Development of PDMS Microfluidic Devices for the SPE

A microfluidic device was designed in AutoCAD. Since both the glucose and lactate sensors produce hydrogen peroxide, and byproducts are commonly produced at the counter electrode, the device was designed to prevent cross-flow from one electrode to another. While a design featuring symmetrical binary splitting at the entrance and exit would have been preferable, the limited footprint of the SPE restricted this addition. The microfluidic network was fabricated from PDMS by replica molding, using photoresist on a silicon wafer as a master. The PDMS polymer was prepared by mixing PDMS pre-polymer with curing agent in a 10:1 ratio by weight. The master was fabricated by spinning a thick layer of photoresist (SU-8 2025) on a silicon wafer and by exposing it to UV light through a chrome mask. Initially a height of 80 μm was used, but this was eventually increased to 150 μm. The master was placed in a Petri dish, which was filled to a height of approximately 1 cm with PDMS polymer and cured in an oven for 4 hrs at 70 °C. After curing, the elastomer was mechanically separated from the master and cut

into discrete devices. Since PDMS could not be bonded to the ceramic Pine Instruments electrode, it was necessary to find a different way to create a seal between the PDMS channel and the electrode. A friction fitting was proposed and designed to account for this sealing issue. Two acrylic plates were milled which could be tightened, using nuts and bolts at the four corners, to create enough pressure to seal the channel over the electrode.

Calibrations of the Multi-analyte Screen Printed Electrode

Fabricated electrodes and microfluidic housing were assembled. Calibration solutions were prepared to allow for simultaneous calibration of glucose, lactate, and pH. In the calibration of the SPE in the traditional PDMS housing, the sensors were calibrated with 50 mM PB with 100 mM KCl with no glucose and no lactate (pH 7.32), with 0.05 mM lactate and 1 mM glucose (pH 7.22), with 0.1 mM lactate and 3 mM glucose (pH 7.05), and with 0.2 mM lactate and 5 mM glucose (pH 6.76). Solutions were pumped into the chamber at 100 μL/min with a syringe pump.

After further sensor and housing development, the sensors were calibrated with modified RPMI media with no glucose and no lactate (pH 8.00), with 0.025 mM lactate and 1 mM glucose (pH 7.50), with 0.05 mM lactate and 2 mM glucose (pH 7.00), with 0.1 mM lactate and 3 mM glucose (pH 6.50), and with 0.2 mM lactate and 5 mM glucose (pH 6.00). These ranges are appropriate to measure changes in ~1 x 10^5 cells in the 3 μL volume of the original MAMP. As the volume of the current microfluidic device is 23 μL, the planar electrodes must be sensitive enough to detect change in metabolism which is about seven times smaller than those observed in the microphysiometer. For this reason, the sensors were further calibrated with modified RPMI media with no glucose

and no lactate (pH 7.39), with 0.01 mM lactate and 0.2 mM glucose (pH 7.35), with 0.02 mM lactate and 0.4 mM glucose (pH 7.28), with 0.03 mM lactate and 0.6 mM glucose (pH 7.23), and with 0.04 mM lactate and 0.8 mM glucose (pH 7.18). Solutions were pumped into the chamber at 100 μL/min with a syringe pump with a dual holder to allow two solutions to be pumped simultaneously to avoid the introduction of bubbles into the tubing. Fluid switching was performed using a Valco valve switching device.

Cell Culture

The adherent human hepatocellular carcinoma cell line, (HepG2, HB-8065, ATCC), was maintained in continuous culture with EMEM, supplemented with 10% FBS, pH 7.40 in a 5% CO_2, 37 °C atmosphere. Subculturing was performed by washing twice with DPBS and rinsing the cells with 0.25% (w/v) Trypsin- 0.53 mM EDTA for 5 min at 37 °C.

Pheochromacytoma cells (PC-12, CRL-1721 ATCC) was maintained in continuous culture with in F12K media supplemented with 15% donor horse serum and 2.5% FBS. Subculturing was performed by washing twice with DPBS, and then adding 4-6 mL of culture media to the flask. A cell scrapper was then used to remove cells from the collagen-coated flask.

Cell Growth on the Roof of Microfluidic Devices

PC-12 cell growth on PDMS was achieved on the roof of the PDMS microfluidic device. After curing, the PDMS devices were trimmed with a scalpel in the biosafety cabinet, and holes punched for tubing. Since the device is only 150 μm deep, a 5 mm-thick sacrificial block of PDMS was temporarily sealed via pressure to the inverted PDMS device to create a well into which cells and adhesion agents could be deposited.

The sacrificial block of PDMS had an approximate area of 1cm^2 cut out of the center to create a fluid well. The block was aligned on the PDMS device to direct cell growth over the open area of the device, so that the cells are directly situated over the electrodes as shown in Figure 32.

For PC-12 cells, several adherence methods were attempted. Unmodified PDMS was used as a control, collagen Type I (500 µg/mL) in 0.01M HCl, collagen Type I (50 µg/mL) in 0.01 N HCl, and poly-L-lysine (50 µg/mL) diluted in Hank's Balanced Salt Solution.

Poly-L-lysine and collagen were pipetted into the wells and allowed to adhere at room temperature for 1 hr. At this time, the solutions were aspirated off and washed twice with DPBS. PC-12 cells (4 x 10^5) were pipetted into each chamber. The devices were then placed in the incubator at 37 °C and 5% CO_2 atmosphere overnight. Cell growth and confluency were affirmed 12 hrs later through visual microscopic inspection. Cells could be grown in the devices for several days as long as culture media was replaced every day. HepG2 cells, an adherent cell line, were grown in a similar manner on unmodified PDMS.

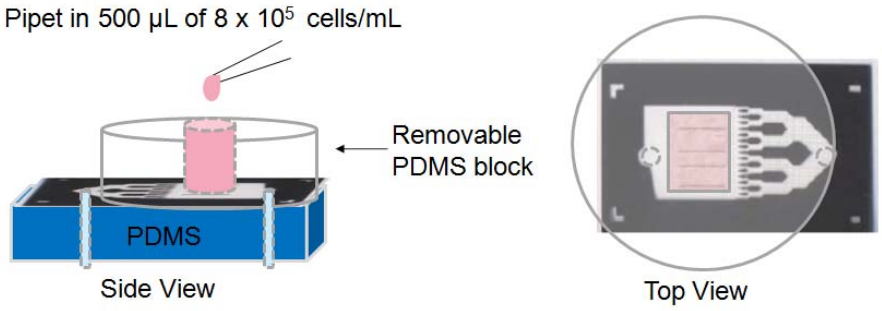

Figure 32. Side and Top View of Devices During Cell Culture. Two pieces of PDMS (microfluidic and sacrificial layer) were sandwiched together to create a well to contain cells. After plating, the devices are incubated for at least 4 hrs to allow cellular adhesion.

Testing Cellular Responses with PDMS Microfluidic Devices

Prior to cell experiments, multi-analyte SPEs were modified with IrOx, GOx, LOx, and Nafion films and stored in PBS at 4 °C. Prior to cell experiments, the sensor was removed and allowed to return to room temperature in air. Modified RPMI with 5 mM glucose is warmed to 37 °C in a water bath, and maintained at temperature with syringe heaters. The media in the well/microfluidic devices is aspirated, and the device inverted onto the sacrificial PDMS block. This block provided a cushion to prevent smashing of the cells as tubing is inserted into the microfluidic device. After tubing had been inserted, the microfluidic was immediately assembled with the multi-analyte SPE. After suitable sealing had been achieved, media was pumped through the chamber until the media has reached the waste tubing of the reference electrode. Due to tubing length and pump speed, this could take up to 30 min, but applying increased pumping or pressure may cause the cells to become non-adhered. Once complete movement of the media had been achieved, the potentiostat is turned on and four-analyte detection was initiated.

Results and Discussion

Characterization of the Multi-analyte Screen Printed Electrode

The multi-analyte SPE was developed to provide the features of both the single analyte SPE developed by Pine Research Instrumentation (Figure 33A) and a MAMP sensor head (Figure 33B). The resulting sensor is shown in Figure 33C, including a close-up of the electrodes. The intended use for each electrode is labeled in the figure; however, any modifications can be made to any of the sensors.

The multi-analyte SPE was studied with profilometry to determine the contours of the surface. A scan location and resulting profile in shown in Figure 34 . By dragging the tip over the surface, it was observed that the areas with ceramic were relatively smooth compared to the exposed electrode areas (Figure 34 .B). The rough surface of the electrode areas is not unexpected, as the conductive surface is formed from printed Pt nanoparticles. An interesting curved pattern was also observed when scanning over the areas where Pt was present under the ceramic layer. Repeated scans over the entire sensor surface were performed to characterize this pattern, and are shown in Figure 35.

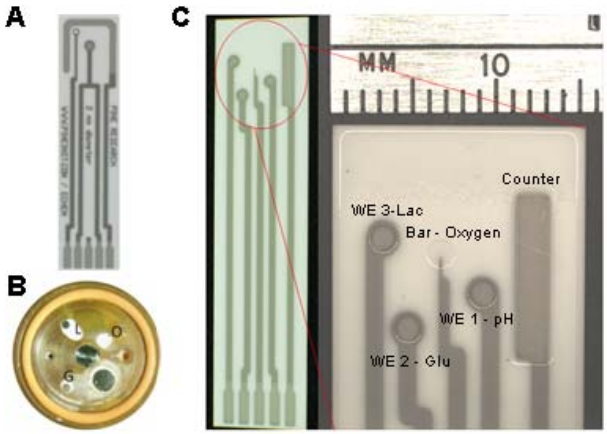

Figure 33. Image of the multi-analyte SPE as compared to the Pine SPE and the MAMP sensor head (not to scale). (A) Single-analyte Pine electrode (B) MAMP sensor head (C) Full image of multi-analyte SPE with close up of electrode areas.

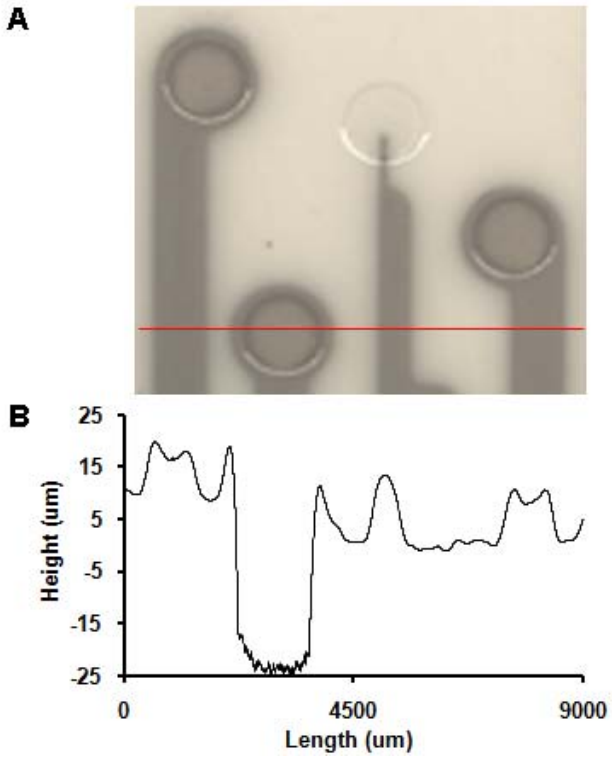

Figure 34 . Profilometry Scan of a Portion of the Multi-analyte SPE (A) Profilometry tip was scanned from left to right across the surface of the SPE as indicated by the red line. (B) The resulting scan plotted in µm.

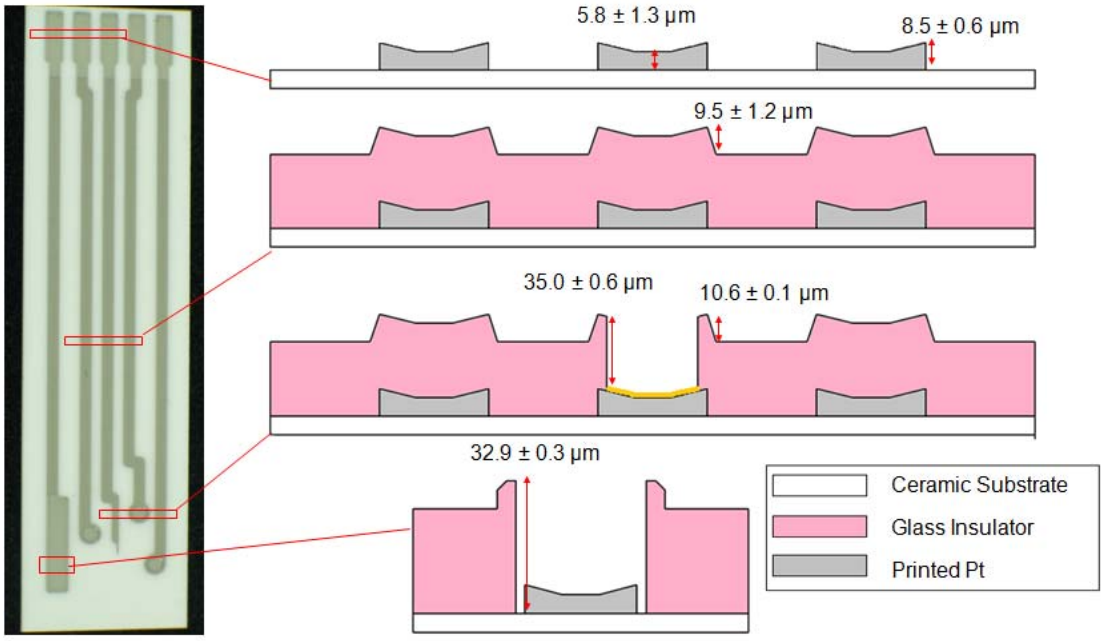

Figure 35.Contours of the SPE based on Profilometry

The Pt contacts at the top of the SPE were found to have a curved surface, with the edge of the contact has a height of 8.5 ± 0.6µm, and the center has a height of 5.3 ± 1.3µm. Apparently, the surface tension of the printed Pt nanoparticles suspended in liquid forms a meniscus, and this shape is maintained after baking to remove the solvent. While this feature does not affect the electrochemical properties of the Pt, or the ease with which an edge card connector establishes contacts to the printed Pt, it does have an multiplicative effect on the ceramic layers printed on top. This can be seen in the scan of the chip over the Pt wires between the contacts and exposed electrodes, where the contours of the printed Pt are still observed, and are in fact slightly increased to 9.5 ± 1.2 µm. These ridges pose a great obstacle in the creation of an effective microfluidic device.

These devices are often sealed to smooth glass, and height difference on the order of 10 μm may not be conducive to proper sealing.

The printed ceramic layer was used to define the electrode areas of the three 1.5 mm diameter disk electrodes. In this case, the liquid ceramic beaded up at the edges of the layer, or the electrode, prior to baking. This effect, in conjunction with the thickness of the ceramic layer, formed a 35 μm well with the electrode at the bottom. This well will be the largest obstacle to creating a successful microfluidic design. If the height of the channel is large compared to the electrode well, fluid should be easily washed out at the electrode surface. The ideal channel height is 100 μm, the approximate height between the sensor head and the cells in the MAMP. With the electrode wells being 35 μm, or approximately 30% of the intended channel height, it is not likely that much fluid exchange will occur at the electrode surface.

Electrochemical testing of the quality of the printed electrodes was performed by cyclic voltammetry in $Fe(CN)_6^{3-/4-}$. As shown in Figure 36A, the three Pt disk electrodes (Ele 1,2, and 3) are identical, showing the reproducibility of electrodes formed by screen-printing. Figure 36B shows the scan at the oxygen electrode, which conducts much less current than the larger electrodes. The average cathodic peak potential, E_{pc}, was 0.182 ± 0.001 V, and the average anodic peak potential, E_{pa}, was 0.253 ± 0.003 V, exhibiting good reversibility (ΔE_p = 70.5 mV).

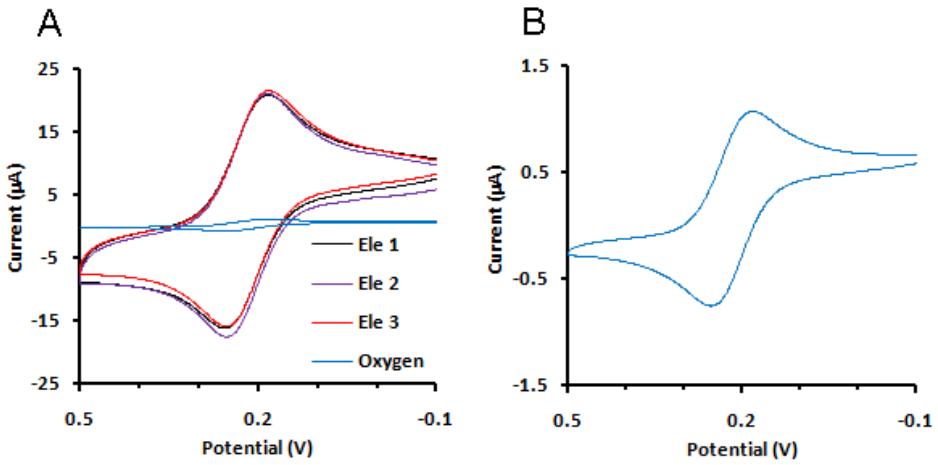

Figure 36. Cyclic voltammogram of four electrodes on the SPE demonstrating the reproducibility of the platinum electrodes.

Formation of Ag/AgCl quasi-reference

The Ag/AgCl quasi-references were found to be stable after 1 to 3 days storage in PB with 100 mM KCl. The additional layers of Ag and AgCl can be seen on the surface of the electrode (Figure 37). The average drift of the sensors was found to be 3.3 ± 1.7 µV/sec. A constant drift on the scale of a few µV per second scale is acceptable because the drift is predictable and the potential would only drift hundredths of a volt in the positive direction for every hour of use. Measuring at a potential of +0.6 V, this amounts to only a 2% drift per hour, meaning the validity of the data would not be greatly affected. The OCP for each reference were not identical; however, all OCPs were between 0 and 300 mV. These results show that reproducible and stable Ag/AgCl quasi-references can be fabricated on the multi-analyte SPE. They also indicate that, although drift on the potential does occur, it is predictable and can be accounted for during data analysis.

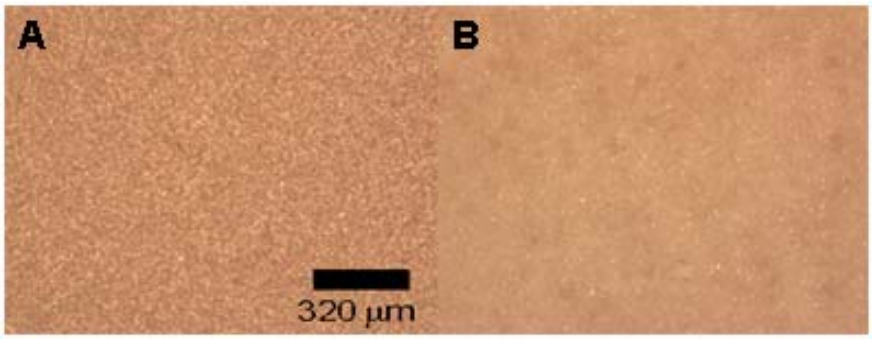

Figure 37. Images of Formed Ag/AgCl quasi-reference electrode Image of electrodes that were (A) unmodified and (B) modified with Ag/AgCl. (Bright field, 50x magnification).

While the reference was functional, for simplicity and increase stability, the large 19 mm^2 electrode was relegated to counter electrode, with the MAMP Ag/AgCl (2 M KCl) reference acting as the reference and placed downstream of the microfluidic chamber. This serves to prevent any reaction products that might be produced at the reference electrode from interfering with the working electrodes.

Calibration of Electrodes in Bulk Solution

In order to characterize the multi-analyte SPE enzyme-based biosensors, calibrations were performed for the GOx and LOx electrodes. The glucose sensor had an average sensitivity of -3.96 ± 0.13 mM/µA and was stable up to six days (Table 1 and Figure 38). In the current MAMP, the enzyme films are only used for one day, however, in future MAMP experiments, it may be necessary to run experiments that span several days, so it is advantageous to have a sensor that is stable for longer periods of time.

Table 1. Calculated Sensitivity of GOx electrode over a week of use.	
	Sensitivity (mM/nA) x 10^{-3}
Day 1	-3.88±0.04
Day 2	-4.12±0.03
Day 3	-3.80±0.03
Day 6	-4.03±0.04

In Figure 38, the life of the enzyme film is shown, showing the SPE before and after coating with GOx and Nafion, the film after use in RPMI, and finally the state of the electrode after undergoing manual cleaning with water and ethanol. In Figure 38D, you can see the film begin to degrade. Figure 38E shows the weathered state of the electrode after manual cleaning, indicating that some of the platinum has been removed from the electrode. The similarity of the acid cleaning scans (Figure 39) from before the electrode was coated and after the film was removed indicates that the electrochemical properties of the electrode are not greatly affected by light cleaning, despite the appearance of the electrode surface in Figure 38E.

Figure 38. Progression of GOx film on the Electrode Surface Over Time.(A) Unmodified (B) 30min after GOx and Nafion are applied (C) After first calibration in RPMI (D) Film after 3 days use and storage (E) Electrode surface after lightly scrubbing with water and ethanol.

The lactate electrode had a sensitivity of -1158 ± 159 µA/mM and was utilized for five days. In this case, the sensitivity of the lactate sensor decreased each day (Table 2). The gradual loss in sensitivity highlights the need for calibration of the sensor during measurement. Although sensitivity loss is not ideal, if it does occur, automatic calibrations will ensure that the change is taken into account.

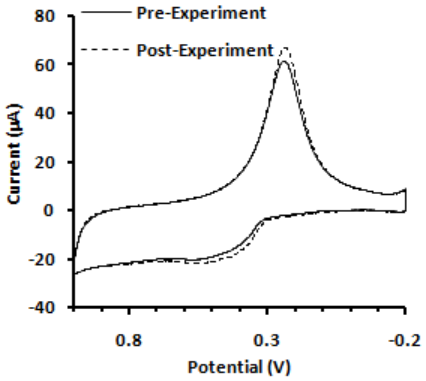

Figure 39. Scans of the electrode in 0.5 H_2SO_4 before and after glucose calibration study.

Table 2. Calculated Sensitivity of LOx electrode over a week of use.	
	Sensitivity (nA/mM)
Day 1	-1370±21
Day 2	-1151±35
Day 3	-1126±20
Day 5	-985±21

Development of the Iridium Oxide pH Sensor on the SPE

Initially, the galvanostatic method IrOx film deposition was applied to the SPE, as previously developed by Dr. Igor Ges.[66]. A light purple film was formed, however, the measured OCP was not stable or reproducible. After a few days, the film had disappeared completely. This method was abandoned for some time and a constant potential method adopted.

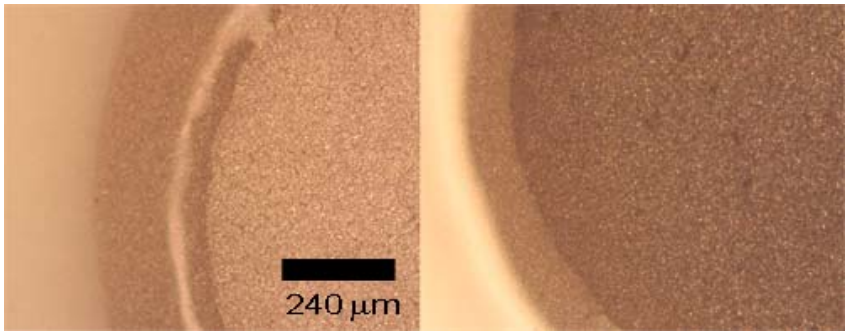

Figure 40. IrOx films formed through constant potential method on the SPE

Dark-blue IrOx films were successfully adhered to 2 mm Pt disk electrode purchased from CHI, as well as the SPE, using the constant potential method at +0.6 V. No visible films were formed at lower potentials. Each attempted plating time afforded dark blue films, with the 10 min plating time forming the film darkest in color. Despite being plated longer, the 15 min film appeared the same as the 7 min film, suggesting that at some time point, additional plating is detrimental to film formation.

Table 3. Drift of Sensor for pH Detection		
	Potential (mV)	Drift (μV/s)
Pt Disk	331 ± 5	-3.50
SPE with External Reference	293.2 ± 0.2	-0.04
SPE with Internal Reference	49 ± 3	1.87

OCPs were measured over 5000 s to determine the stability of the films formed at +0.6 V *vs* Ag/AgCl (2 M KCl) for 420 s in pH 7.00 PB. The results can be seen in Table 3. The OCP and drift of the SPE pH sensing electrode was measured versus an aqueous Ag/AgCl reference (2 M KCl) as well that the internal reference featured on the SPE. The OCP of the Pt disk electrode was 331 ± 5 mV, with a drift of -3.5 μV/s. The SPE with the external reference had an OCP of 293.2 ± 0.2 mV, and a drift of -0.04 μV/s, while in the IrOx film using the SPE internal reference film, the OCP was 49 ± 3 mV and the drift 1.87 μV/s. The large discrepancy between the drift of the SPE film when an internal and external reference was used is most likely due to the drift in the quasi-reference electrode. The drift of the reference on the SPE used for this study was found to be 4.4 ± 1.8 μV/s on the days leading up the experiment. The small drift in voltage during detection of pH indicates that a stable IrOx film was able to be formed on the disk electrode of the multi-analyte SPE, and that it will be possible to use IrOx films to replace the LAPS in the next-generation MAMP.

Development of PDMS Microfluidic Devices for the SPE

Several microfluidic devices specific to the SPE as described in Methods were designed by Phil Samson and Dr. Dmitri Markov and corresponding SU-8 masters

created by David Shaffer. Two designs are shown in Figure 41. Dark areas represent where PDMS will be in contact with the multi-analyte SPE, with lighter areas representing where fluid will flow. The designs are largely identical, with a binary splitter distributing flow over the width of the channel as the fluid is pumped into the chamber.

Figure 41. Designs of two microfluidic devices

The main difference in the designs is the method used to support the PDMS roof over the width of the multi-analyte SPE. The design featured on the left is composed largely of 100 μm posts, while the design on the right supports the roof with four bars. Initially, the "post" design was tested using a master with 80 μm features. With a height of 80 μm, the chamber has a volume of ~12.5 μL. Figure 42 shows images of the assembled device as green dye is flushed from the chamber (left to right). As water is flushed into the chamber via syringe, the dye is first removed from the center of the chamber, while the edges are not receiving flow. Even the electrodes receiving flow are dark, as it takes longer for the electrode wells to be washed out. In the third image, the center electrodes are further washed out, while the disk electrode in the corner is still covered in dye. Finally, most of the dye has been removed, although some remnants can be seen in the electrode wells and part of the counter electrode. This pattern of fluid replacement shows the uneven flow achieved in this microfluidic design. An electrode design that would

allow for binary splitting on both ends of the device would achieve even flow to all of the electrodes.

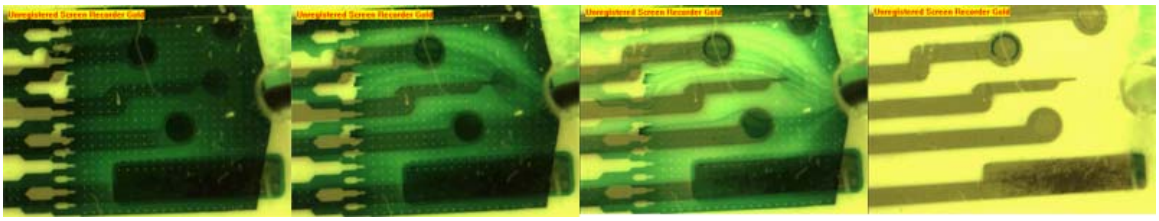

Figure 42.Video shots as dye is flushed out of the 80 µL tall microfluidic chamber. Green dye is replaced in the chamber by water (left to right).

Preliminary testing showed that achieving sufficient flow over the recessed disk electrodes at 80 µm was difficult, and calibration experiments were not successful for this reason. Additionally, bubbles introduced to the chamber stuck to the posts, further inhibiting flow. For this reason, the second microfluidic design, which featured bars to support the roof, at a height of 150 µm was used for the remaining experiments. Figure 43 shows the assembled device with the downstream Ag/AgCl (2M KCl) reference electrode.

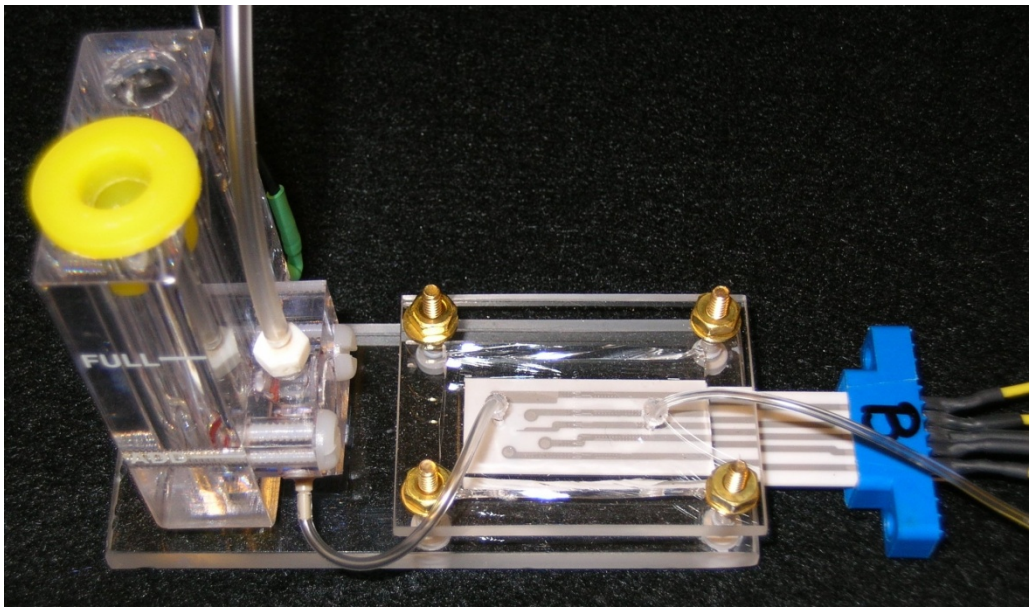

Figure 43. Assembled microfluidic device with SPE, connector, inlet and outlet tubing, and downstream reference electrode

Calibration of the Multi-analyte Screen Printed Electrode

When the PDMS device was first created and optimized to a height of 150 μm, all four analytes were simultaneously measured while the glucose, lactate, and pH sensors were calibrated using solutions in 50 mM PB with 100 mM KCl. Four solutions of increasing concentrations were perfused through the chamber at 100 μL/min. Figure 44 shows the amperometric and potentiometric signals collected during this calibration, as well as calibration curves for glucose, lactate, and pH. Oxygen was not calibrated. The spikes seen prior to each changing signal were due to bubbles introduced when changing the syringes containing the calibration solutions. Introduction of bubbles continued to occur, and this was addressed by purchasing dual-channel syringe pumps and employing a valve switching device to direct different solutions to the chamber. In this calibration, detection of glucose, lactate, and pH occur with low noise and high sensitivity over the selected

concentration ranges. The glucose sensor calibration was plotted in a Lineweaver-Burke plot using Michaelis-Menton enzyme kinetics, as the linear range of the glucose sensor did not extend to 5 mM glucose. The resulting curve can be used to calculate metabolic rates of glucose in MAMP stop-flow experiments, as well as to calculate the K_m and V_{max} of the GOx film. The change in current at the glucose electrode is well above the noise of the signal. Additionally, the sensitivity is within the range calculated when calibrating the glucose-sensing electrodes in bulk solution.

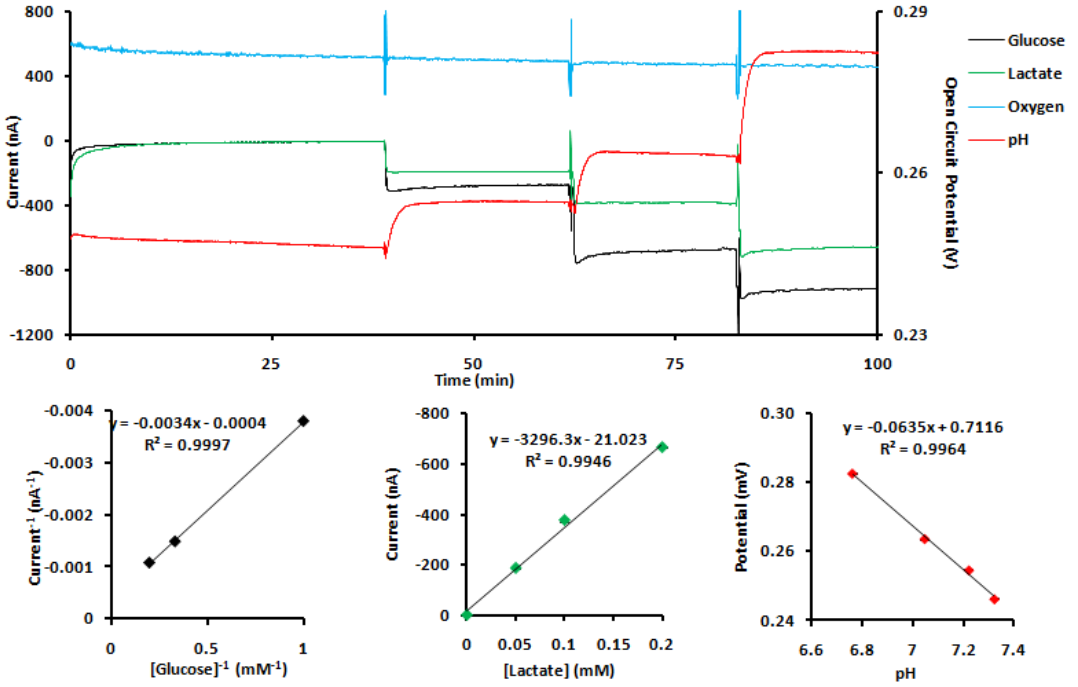

Figure 44. Calibration of Multi-analyte SPE in Phosphate Buffer. The modified SPE was assembled as shown in Figure 43. PB with 100 mM KCl with increasing concentrations of glucose and lactate, and decreasing pH were pumped via syringe pump through the chamber at 100 µL/min to as all four analytes were sampled by the multi-chamber multipotentiostat (A). (B) Glucose calibration curve (C) Lactate calibration curve (D) pH calibration curve.

While the lactate sensor employs an oxidase enzyme for detection, the concentrations expected for lactate are lower, and the linear range of the sensor is not exceeded. Thus, the calibration curve can be plotted linearly. The sensitivity of the lactate sensor in the microfluidic device was higher than that of bulk solutions; however more enzyme was used for this film, so a larger response is expected. The sensitivity of the electrodes in highly subject to enzyme loading, actual microfluidic volume, and flow rate, to name a few. Until the SPE and microfluidic devices are fully optimized, it is difficult to compare sensitivities calculated from calibration curves to other experiments.

The response time of the sensors in the chamber was about 10 s, which may be connected to the large device volume (~23 μL) as well as the topography of the SPE. The amount of time required to completely wash the previous solution out of the recessed electrodes and out of the chamber increases the apparent response time of the sensor, despite the rapid response time that the individual electrodes may be capable of achieving.

The IrOx sensor yielded a supernerstian sensitivity of -66 mV/dec, which is within the range of -60 – 90 mV/dec which may be expected for AEIROF-formed films. The response time of this sensor was closer to 40 s. The increased response time of the IrOx sensor over the lactate and glucose sensors is probably due to the constant potential method used to form the films. This method forms very dark films, consisting of several layers, which may lower the responsiveness of the sensor.

Another set of calibration experiments were performed using flow rates appropriate for cell experiments, in this case, 20 μL/min and RPMI media. The glucose, lactate, and pH electrodes on the SPE were simultaneously calibrated using concentrations ranges used in the original MAMP, as well as a smaller concentration range to reflect the smaller changes in metabolism that would be expected in a chamber with larger volume and similar cell density as the MAMP. Figure 45 shows the amperometric and potentiometric signals collected during this calibration, as well as calibration curves for glucose, lactate, and pH. Oxygen was not calibrated. Again, the glucose sensor calibration was plotted in a Lineweaver-Burke plot. The change in current at the glucose electrode is well above the noise of the signal. Despite the increased noise, the lactate sensor responded linearly, and the smaller steps (0.025 mM and 0.05 mM) were statistically different. The response time

for the glucose and lactate sensors also seems to have increased as compared to the previous calibration, which is certainly due to the five-fold decrease in pump speed, slowing down the exchange of solutions in the chamber.

The IrOx sensor yielded a sensitivity of -76 mV/dec, which is within the range of -60 – 90mV/dec which may be expected for AEIROF-formed films, and is increased as compared to the previous calibration. These films were formed in the same manner as the previous calibration, with the following changes. The iridium oxalate solution was passed through a 0.2 μm syringe filter and the electrode was preconditioned at -0.6 V for 60 s prior to plating the film. The response time of this sensor was closer to 40 s.

Without disassembling the device, the SPE was then calibrated over a smaller range of concentrations which might be expected in a chamber which is roughly seven times larger than the MAMP microfluidic chamber. Figure 46 shows the amperometric and potentiometric signals collected during this calibration, as well as calibration curves for glucose, lactate, and pH. Oxygen was not calibrated. Glucose was again plotted as a Lineweaver-Burke plot to allow comparison to previous calibrations. The change in current at the glucose electrode is still well above the noise of the signal, indicating it is sensitive enough to measure physiologically relevant changes in glucose consumption within the chamber. The increase in current due to increased lactate concentration was linear, however the noise in the signal at this concentration suggests that the lactate electrode would not be sensitive enough for cellular measurements in the device. If the source of the noise in the chamber could be removed or reduced, the sensitivity of this method would be vastly improved.

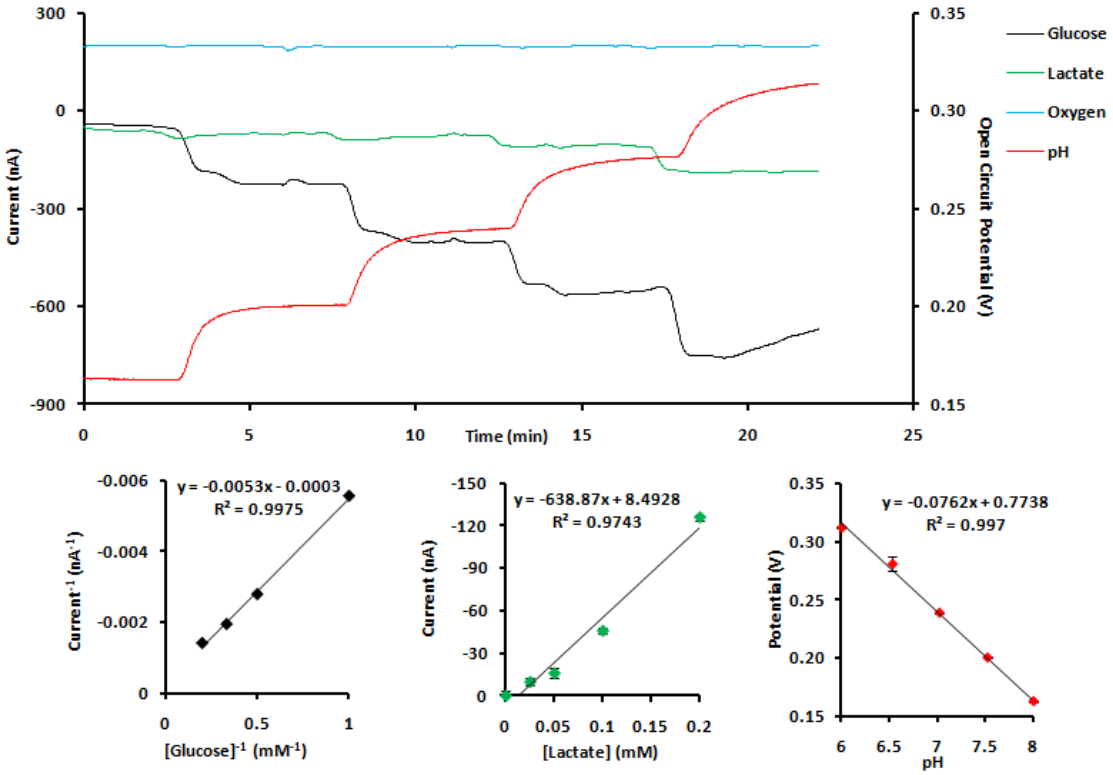

Figure 45. Calibration of SPE in Microfluidic Device with RPMI The modified SPE was assembled as shown in Figure 43. Low-buffered RPMI with increasing concentrations of glucose and lactate, and decreasing pH were pumped via syringe pump through the chamber at 20 µL/min to as all four analytes were sampled by the multi-chamber multipotentiostat (A). (B) Glucose calibration curve (C) Lactate calibration curve (D) pH calibration curve.

The IrOx sensor yielded a sensitivity of -66 mV/dec, which is within the range of 60 – 90mV/dec which may be expected for AEIROF-formed films, but is less than found for the sensor in the previous calibration. The linear response of the electrode can depend on the range over which it is tested, and it is possible if larger changes had been included in this calibration, the calculated sensitivity would have increased.

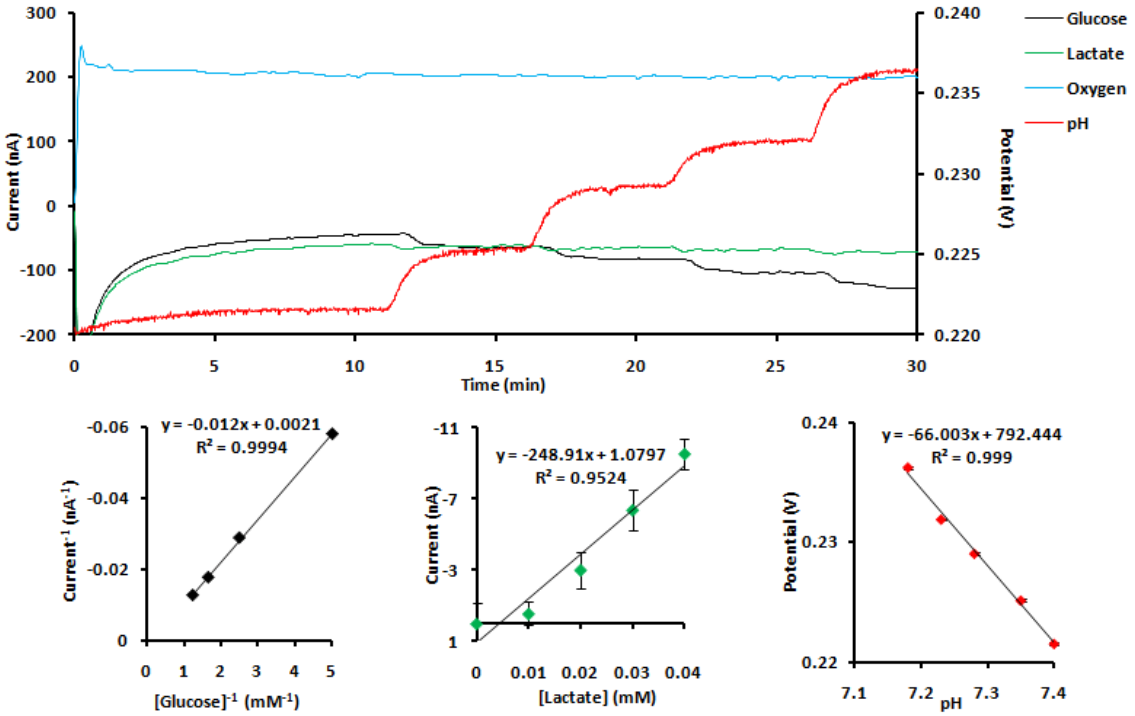

Figure 46. Calibration of SPE in microfluidic device with RPMI over a smaller concentration range shows chamber volume will not affect ability to measure metabolic flux The modified SPE was assembled as shown in Figure 43. Low-buffered RPMI with increasing concentrations of glucose and lactate, and decreasing pH were pumped via syringe pump through the chamber at 20 µL/min to as all four analytes were sampled by the multi-chamber multipotentiostat (A). (B) Glucose calibration curve (C) Lactate calibration curve (D) pH calibration curve.

Testing Cellular Responses with PDMS Microfluidic Devices

PC-12s and HepG2 cells were cultured on the roof of PMDS microfluidic devices as described in methods. PC-12s were found to be unsuited for adherence to PDMS, as even low flow rates < 2 µL/min resulted in removal of cells from the roof of the chamber.

Two microfluidic devices with 8 x 10^5 HepG2 cells cultured on the roof were assembled with SPEs and all four analytes measured (Figure 47). RPMI media with 5 mM glucose was pumped through the chamber at 15 µL/min for 1 hr. At this point, the

flow was stopped for 40 s every 5 min to observe the current change during stop-flow periods.

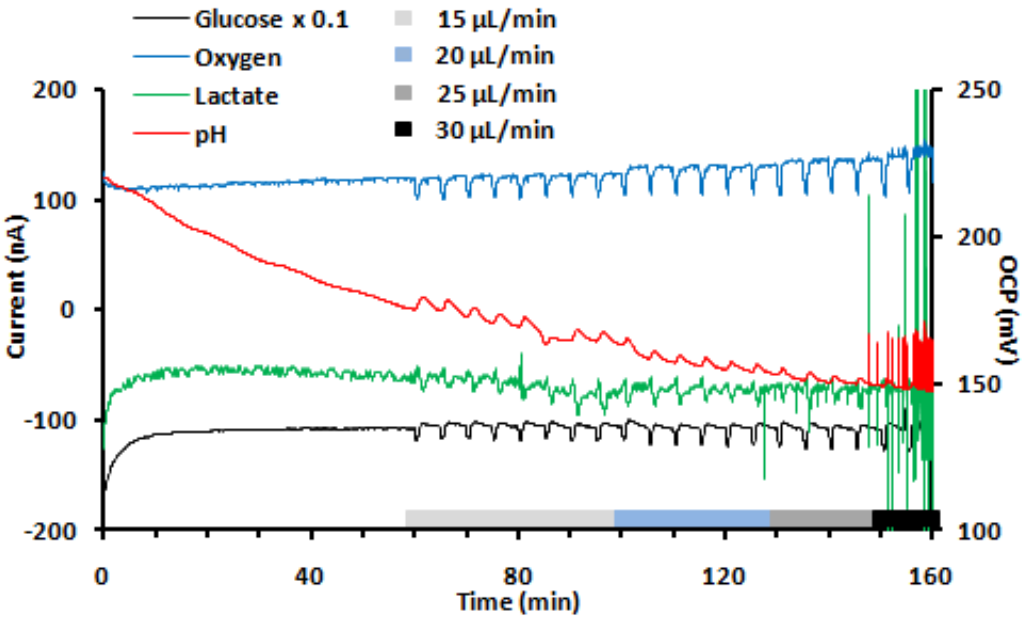

Figure 47. Flow Rate Test of HepG2 cells in Microfluidic Device Glucose, lactate, and oxygen are plotted on Axis 1. Glucose is shown as 10% of actual current. OCP is plotted on Axis 2. Flow rates throughout the experiment are shown on the x-axis. Flow was stopped every 5 min for 40 s.

Glucose is plotted at 10% of the actual current to allow all three amperometric signals to be shown together. Once sampling of current begins, all three signals reach a steady baseline within 10 min. Once stop-flows begin, oxygen consumption can be observed. The enzyme electrodes do not display their characteristic peak directions as seen in the MAMP. This is due to the flow in the chamber, as possibly the enzyme films as well. A significant oscillation can be seen in the lactate signal, and is commonly seen in this device when the electrodes are not receiving significant flow. As the flow rate is

increased, a slight shift in baseline of the currents is observed. This is expected, as the current is affected by the rate at which analyte flow past the electrode.

OCP is plotted on the 2nd axis. A significant drift in the OCP is observed, especially in the first hour of measurement. The IrOx electrode often required at least an hour of equilibration to reduce drift in the signal.

As the flow rate increased to 30 μL/min, the noise increased drastically in all four signals. This is likely the rate at which the HepG2s begin to strip off the roof of the chamber, interfering with electrodes and partially blocking the flow of media through the chamber. Further experiments with HepG2 cells should use a flow rate of 20 μL/min.

Only one chamber is shown in Figure 47, but two replicate chambers were tested in this experiment. The replicate chambers of glucose, lactate, and pH are shown in Figure 48. The oxygen signal in Ch 1 was not operational. Comparable currents and potentials were measured in replicate chambers, showing that the electrodes were modified reproducibly, and that the chambers were assembled in the same manner. This shows that the changes in current observed at the enzyme electrodes during the stop-flow are due to the fluid dynamics occurring in the chamber. It is likely that the use of stop-flow in the SPE-based MAMP will not be feasible, as the dynamics of fluid in the chamber does not allow for straightforward analysis of the stop-flow peaks.

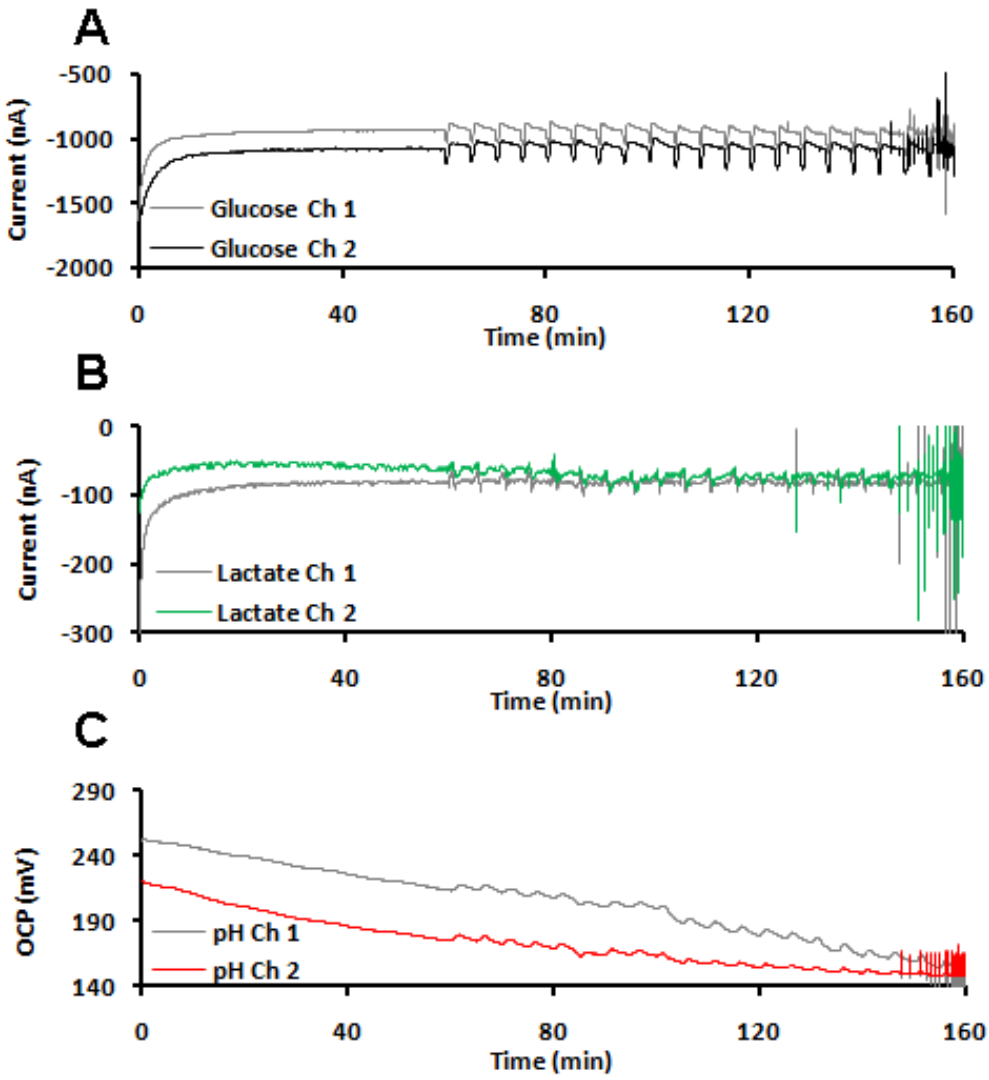

Figure 48. Replicate chambers of Flow Rate Test of HepG2 cells. Measurement of glucose (A), lactate (B), and pH (C) in two replicate microfluidic chambers with HepG2 cells.

Conclusions

The feasibility of using a screen-printed electrode as a component of the next-generation MAMP was explored in this study. The resulting sensor was reliable, disposable, highly adaptable, but ultimately unsuited for incorporation with a microfluidic device. The contours of the sensor surface made sealing to a device difficult, and even when successfully sealed, reproducibility was not achieved. Several options are feasible moving forward including SPEs polished to diminish the contours, planar platinum electrodes vacuum deposited on glass substrates, and instrumented electrodes for microfluidic well plates. These options will be discussed further in the following chapter.

Acknowledgments

This work was supported by NIH grant U01 AI 061223, Defense Threat Reduction Agency grant HDTRA1-09-1-0013, the Vanderbilt Institute for Integrative Biosystems Research and Education, and DOE fellowship Graduate Assistance in Areas of National Need. This work would not have been possible without collaborations with and use of instruments associated with Vanderbilt's Institute of Integrative Biosystem Research and Education. Collaborations with and assistances from Dr. Leslie Hiatt, Ron Reiserer, Dr. Igor Ges, David Schaffer Dr. Jason Greene, Dr. Dmitri Markov, and Phil Samson were essential.

CHAPTER VI

CONCLUSIONS AND FUTURE DIRECTIONS

In Chapter II, new insights indicating acid as the essential mediator of neuronal survival were made possible through the coupling of powerful preconditioning models and multi-analyte microphysiometry. Further work could focus on how modulation of extracellular acid through stimulation with exogenous agents further effects neuronal survival. This work, in conjunction with traditional biochemical assays, may help to identify the mechanism by which the glia are able to mediate neuronal protection.

The capabilities of the MAMP were further improved during this study through the addition of a new pH sensor which yielded a near four-fold decrease in noise. This decrease in noise was made possible by the development of the potentiometric module for the multi-channel multi-chamber potentiostat. Prior to its development, only acid could be measured potentiometrically in the MAMP, and only through the LAPS of the Cytosensor. The new modules expand the current capabilities of the MAMP beyond the four analytes discussed within the body of this dissertation. The freedom of the new potentiometric module will allow for real-time sensing of other important cellular analytes which are commonly detected with potentiometric sensors, including K^+, Ca^{2+}, and other ions. In the context of studying ischemia, the development and integration of a sensor for real-time K^+ flux from astrocytes and glia, to be measured simultaneously with the other analytes, would provide further insight into neuronal responses.

The new potentiometric sensor could also find utility in the further investigations of CTx on cellular metabolism through the addition of a Cl^- sensing electrode. Previously investigation of the effects of CTx on intestinal cells revealed a lag-time significantly longer that the 10 minutes observed in this study, with a lag of almost an hour.[16, 17, 78] This conclusion was based on the delayed release of Cl^- as measured by electrophysiology methods. [16]

Electrophysiology techniques are better suited to measuring changes in ion fluxes, and the addition of a Cl^- sensor which could selectively measure chloride through potentiometric methods could prove to have improved selectivity.[108] A simple chloride sensor can be fabricated by the anodizing a Ag wire embedded in the MAMP sensor head in concentrated KCl to form a stable AgCl layer. Alternatively, a layer of Ag may be first be deposited on Pt, and then anodized in KCl, as discussed in Chapter V in the creation of a Ag/AgCl quasi-reference for the multi-analyte SPE.

The potential measured at the electrode is sensitive to changes in Cl^- in a logarithmic manner, and these changes due to chloride flux would be measured potentiometrically. Examples of Ag/AgCl-based sensors, as well as other Cl^- sensors based on alternative conductive platforms, are widely available in the literature. One potential complication of Cl^- sensing is the high background concentration of Cl^- ions present in common RPMI media. Nair *et al* observed that stimulation of epithelial cells with ATP and phorbol-myristate acetate resulted in a 5 mM increase in extracellular Cl^- from 1.2×10^6 cells, but used a specially-formulated buffer solution which only contained 2.3 mM Cl^-.[108] It is likely that the stop-flow method will increase the sensitivity of the method by allowing a build-up of ions, but if relevant changes in Cl^- concentration cannot be observed over the

large background concentration of ~120 mM Cl^- in RPMI media, it may be necessary to further modify the media formulation to perform sensing of chloride ions. In addition, the chloride electrode must be insensitive to changes in pH during stop-flow periods as well as during continuous flow.

Addition of a Cl^- sensor is just one of the future directions possible in the study of the effects of CTx on cellulal metabolism. In Chapter III, only the PC12 cell line was utilized due to the large response seen when dosed with CTx. This response is believed to be due to the high level of GM1 receptors present in the PC12 cellular membrane, but no quantification of these concentrations has been performed. Quantification of GM1 receptors could be performed by treating cells with FITC-labeled CTxB, which binds specifically with that receptor, in conjunction with flow cytometry to quantify the fluorescence. The levels of GM1 receptors could then be correlated to observed responses the CTx in order to relate GM1 levels with response time and magnitude of metabolic response.

In addition of quantification of GM1 receptors in the PC12 cell line, other cell lines could be studied. Increased membrane concentration of GM1 receptors is easily achieved by incubation of plated cells with exogenous GM1.[22] After pre-incubation, excess GM1 is washed away, and CTx exposure performed. Increased GM1 levels results in a stronger and faster response to CTxB and CTx. As with the flow cytometry study proposed above, quantification of GM1 could be correlated to the time and magnitude of cellular response.

Quantification of receptors for the binding and transcytosis of SEB could also be performed using the Caco-2 and T84 intestinal cell lines. In Chapter IV, it was shown that both cells lines were responsive to SEB exposure, causing a temporary increase in

anaerobic respiration as hypothesized. Unfortunately, the response was not reproducible, a result which was attributed to variations in cellular membrane receptors which may vary during culture. Quantification of the processes responsible for binding of SEB may help to elucidate the reason for the irreproducible findings, and improve future MAMP investigations with SEB. Once achieved, a possible follow-up experiment could include using exogenous agents to block SEB from binding to the trancytosis receptor expressed on the cellular membrane of T84 cells.

While RAW 264.7 macrophages, a murine cell line, did not respond to SEB with a change in cellular metabolism, it is possible that another macrophage or B cell line may be more responsive. The selection of a human macrophages would be beneficial, as they have been shown to have a stronger response to SEB exposure.[28]

Jurkats were chosen as a model T lymphocyte due to its extensive use in the VIIBRE program, but ultimately lack the Vβ regions on the TCR which are responsive to SEB. Additional literature searches suggest the Jurkats possess the Vβ 8,[95] which is responsive to staphylococcal enterotoxin E (SEE) rather than any of the other SAgs produced by *Staphylococcal aureus.*[93] Future work should focus on immune cells expressing one of the Vβ regions for SEB, and explore the use of SEE rather that SEB.

Chapters II, III, and IV focused on the use of the MAMP technology to specific biological applications, including ischemia and bacterial toxins. Chapter V and the accompanying appendices outline a majority of the work that has been performed to expand the current capabilities of the MAMP method. In Chapter V, a multi-analyte screen printed electrode was designed, modified for detection of extracellular metabolites, and incorporated into a microfluidic environment for the real-time

measurement in a cellular environment. The ultimate conclusion of that study was that the SPE was a stable, reproducible platform that was easily modified for a range of applications, but that the contours of the surface made sealing to the microfluidic device more difficult. The difficulty of this method hampered reproducibility and often resulted in cell death. It may be possible to further modify the chip by polishing down the edges of the ceramic insulating layer, thus improving sealing and reducing the depth of the electrode wells formed by the welling up of the ceramic layer around the disk electrodes.

Appendix A discussed the possibility of using evaporated Pt electrodes for MAMP studies. While more complicated to fabricate than the SPEs, due to the microfabrication methods employed, these electrodes could be further miniaturized with several sensors present on one substrate, allowing for smaller sample volumes, as well as increased parallelization.

Finally, while not discussed in this work, the use of instrumented sensor heads which may be suspended in a well plate would be a viable method for real-time monitoring of cellular metabolism. The suspension of a sensor head into a well of cells is what is done in the current MAMP, however, the current instrument utilized the LAPS below the well to monitor pH changes. With the development of the new potentiometric module, which was tested in Appendix B, and IrOx-based acid sensors, discussed in Chapters II, V, and Appendix A, it is feasible to eliminate the LAPS. This would removed the requirement for specialized well plates for acid sensing, and allow for any well plate system to be used, provided an instrumented sensor head of the appropriate dimensions was created. One version of this sensor has already been designed by Ron Reiserer at *VIIBRE*.

The research discussed in this work have significantly contributed to the study of ischemic neurons, and provided new insights into the role of bacterial toxins on cellular metabolism. Additionally, the wealth of techniques possible with the MAMP has been expanded through the design and implementation of new sensor platforms, sensing elements, and instrumentation for multi-analyte data collection from current and future sensors. Based on these advancements, the future of the MAMP technology will continue to expand and provide new and exciting insights into the role of metabolism in cellular disease and stress.

APPENDIX A

DEVELOPMENT OF A MICROFABRICATED PLATINUM ELECTRODE FOR THE NEXT GENERATION MAMP

In order to improve the capabilities of the MAMP, a new platform is needed to reduce noise, allow for a customization, and have a smaller bench-top footprint. Our study of SPEs as a platform for a next-generation MAMP concluded that while the electrochemical capabilities of the SPE were robust and suited for MAMP measurements, the contours of the SPE surface made it unsuited for coupling with a microfluidic device without further modification to reduce the contours.

Microfabricated Pt electrodes can be formed on silicon or glass substrates, and like SPEs, can be customized to form an endless variety of electrode patterns. These electrode patterns are formed by vacuum depositing the Pt onto the entire substrate, and then using photolithography methods to remove all the Pt not required for the electrode.[99] Adhesion of platinum onto glass substrates is increased by depositing a thin layer of titanium prior to platinum. The thickness of the deposited Pt is controlled by deposition time.

After Pt has been deposited substrates are coated with a standard photoresist, and treated with UV light while covered with a mask featuring the intended design on the electrode. Appropriate masks are designed in AutoCAD, and allow for the formation of microelectrodes. This method has allowed for the formation of 500 μm^2 electrodes for measuring the metabolism of single cells in a nanophysiometer.[35, 66]

Depending on the photoresist and mask used (either a negative or positive image of the design), the photoresist is then developed, with the final result that only the desired metal

is covered in photoresist. This layer protects the deposited Pt during ion etching, which removes the Pt from the rest of the substrate. The electrodes can then be insulated with a variety of materials. As with the SPEs, which were insulated with printed ceramic, only the contacts and electrode areas are left uncovered.

This work discusses the work performed to create microfabricated platinum electrodes for the next-generation MAMP. Once complete and optimized, the smooth glass substrate combined with the photo-curable PDMS microfluidic devices designed by Dr. Leslie Hiatt may form the first successful next-generation MAMP.

Experimental

Materials

Ir(IV) chloride (99.95 %) were purchased from Alfa Aesar (Ward Hill, MA. PDMS elastomer composed of prepolymer and curing agent (Sylgard 184 kit) was purchased from Dow Corning (Midland, MI). Potassium chloride, phosphate-buffered solution (PB; 50 mM in phosphate, pH 7), sodium chloride, potassium carbonate, sulfuric acid, and 30% hydrogen peroxide were obtained from Fisher Scientific (Pittsburg, PA). Glutaraldehyde (glutaric dialdehyde, 25 wt % solution in water) was purchased from Sigma (St. Louis, MO). Titanium (99.95%) and platinum (99.95%) were purchased from Goodfellow Corp. (Oakdale, PA).

Design and Characterization of the Microfabricated Platinum Electrode

Based on results with the multi-analyte SPE, it was clear that electrodes with a smaller profile would be required to achieve a proper seal and perform microphysiometry. Planar

electrodes printed on 2” x 3” glass substrates to allow for a larger footprint for the microfluidic channel, and the configuration of the metal electrodes was altered slightly to take advantage of this. The insulating layer was not used to define the disk electrode size, so the diameter of the electrodes was reduced from 2 mm to 1.5 mm. Additional configurations were created, including one with a reduced area between the contacts and the electrodes. This was to move the active electrode area closer to the center of the glass slide, simplifying sealing of the microfluidic channel.

Formation of Microfabricated Platinum Electrodes

Thin film metal electrodes were fabricated using e-beam vacuum evaporation of Ti and Pt from carbon crucible liners. The deposition rate and the thickness of the films were monitored with a controller MDC-360 (Maxtek, Inc.). The glass substrates were thoroughly cleaned prior to deposition. The planar metal electrodes consist of two layers: a Ti adhesion layer and a Pt layer. Thin film electrodes were deposited by e-beam vacuum evaporation of Ti and Pt in a single process without breaking vacuum. This process was performed by Igor Ges.

The planar electrodes were fabricated by patterning the Ti–Pt films using a standard photolithography process with a 1 μm thick photoresist (Futurex NR7-1000P). Futurex is a positive photoresist, which means that areas exposed to UV wavelengths through the mask will be cured, and not wash away when the slides are developed. Prepared platinum substrates were spun at 4000 rpm and cleaned with acetone and isopropyl alcohol under a stream of nitrogen. Once dry, Futurex photoresist was added drop-wise from a 5 mL disposable syringe with a 0.2 μm syringe filter. The substrate was then spun for 10 s at 500 rpm to spread the photoresist, and then for 45 s at 4000 rpm. The substrate was then

baked at 3 min at 150 °C. This bake time is longer than what would be used for silicon wafers, due to the thickness and insulating properties of the glass slide. Once the slide had cooled, the slide was exposed to UV light (320-500 nm) with a 5 mm light guide attached to a collimating adapter. The set intensity was set to 4900 mW with an exposure time between 10 and 20 s. The expanded light circle had a 5 cm diameter. The exact procedure had day to day variability due to changes in the intensity available from the Novacure lamp, so substrates should be prepared one at a time to optimize the method for that day.

After exposure, the slides are baked at 100 °C for 3 min. Once cool, the slides are developed in Futurex developing solution to remove the photoresist that was not exposed to UV light. The unprotected Ti–Pt film was removed by ion beam etching. This process was performed by Igor Ges.

Fabrication of an Insulation Layer for the Planar Electrode

After removal of the photoresist, a layer of photoresist (SU-8 2005) was used to cover the glass slide with the exception of the desired active electrode areas and contacts. Substrates were spun at 2000 rpm and cleaned with acetone and isopropyl alcohol under a stream of nitrogen. Once dry, SU-8 was added drop-wise from a 5 mL disposable syringe with a 0.2 μm syringe filter. The substrate was then spun for 5 s at 500 rpm to spread the photoresist, and then for 30 s at 2000 rpm, based on the instructions for a 6 μm layer on silicon.

The prepared slide was then placed on a hotplate while the temperature was ramped to 97 °C, baked at that temperature for 3 min, and cooled back down to room temperature. Once cool, the slide was exposed to UV wavelengths with an intensity of I = 18000

mJ/cm^2 for two exposures of 10 s each. SU-8 is a negative resist, so only the areas where SU-8 was not desired (electrode area and contacts) were covered on the mask.

After exposure, the slides were placed on the hot plate as it was ramped to 97 °C at a rate of 2 °C/min, and then cooled back to room temperature. The slides were then developed in SU-8 developing solution for 1 min, and rinsed with IPA and spun dry. To hard-bake the SU-8 onto the slide, it is placed on the hot plate and covered with a glass dish. The hot plate is ramped to 180 °C as a rate of 1 °C/min, baked 20 min, and allowed to cool back to room temperature. After adhesion of the SU-8 layer, the multi-analyte planar electrode is ready for use. The VEECO profilometer was used to determine thickness of evaporated platinum and SU-8 layers.

Cyclic voltammetric measurements were carried out using a CHI 660A electrochemical analyzer (CH Instruments, Inc., Austin, TX). The four working electrodes were scanned in 5 mM ferricyanide with 100 mM KCl at a scan rate of 0.1 V/s. The largest electrode on the SPE was used as a counter electrode, and measurements were against an external Ag/AgCl (2 M KCl) reference electrode.

Iridium Oxide Synthesis and Electrode Fabrication

IrOx was synthesized as described in Chapter 5 and published procedures.[65, 66] Evaporated platinum electrodes fabricated by Ges[66] utilized the galvanostatic, or constant current, mode of IrOx film formation. Both constant current and constant potential methods were explored for the microfabricated Pt electrodes. For the constant potential method, the electrodes were first preconditioned by holding the potential at -0.6 V *vs* Ag/AgCl (2 M KCl) for 60 s, and then electroplated with IrOx by holding the potential at

+0.6 V *vs* Ag/AgCl (2 M KCl) for 600 seconds using the CHI 660a potentiostat. A Pt wire mesh was used as a counter electrode.

In the constant current method, the electrode was held at a current density of 1.5 mA/cm^2 *vs* Ag/AgCl (2 M KCl) for 600 s using the CHI 660A potentiostat. A Pt wire mesh was used as a counter electrode. Several electrodes on each multi-analyte planar sensor were coated to simplify IrOx sensor evaluation. After film formation, the sensor was stored in 50 mM PB for 2 days at 4 °C to stabilize.

Evaluation of Iridium Oxide Films on Evaporated Platinum

The effectiveness of the formed IrOx films was evaluated with stepwise calibrations performed in conjunction with a glass pH electrode. The pH meter probe, planar sensor, and reference electrodes were suspended in approximately 80 mL of water in a beaker with stirring. The potentiometric module of the VIIBRE multipotentiostat was used to monitor OCP at several electrodes simultaneously, which is not possible with the CHI potentiostat. Separate Ag/AgCl (2 M KCl) reference electrodes were used for each channel. Dilute HCl or NaOH were added either 3 or 4 min apart while the changes in pH at the pH meter were manually recorded. These calibrations were used to determine the sensitivity of the formed IrOx films.

Results and Discussion

Evaporated Platinum Electrodes

Platinum electrodes were fabricated as described. Figure 49 shows the three designs tested during fabrication. Positive masks were used for the electrode designs as a postive

photoresist was used in electrode fabrication. Each electrode design is accompanied by a negative mask for application of the SU-8 insulating layer.

Initially the design most similar to the multi-analyte SPE was used (top left), but the extended path of Pt between the contacts and the electrodes used up much of the footprint of the 2'' x 3'' glass slide, pushing the electrodes to the edge of the glass. This would create issues when fitting a glass slide with photo-curable PDMS over the electrodes.

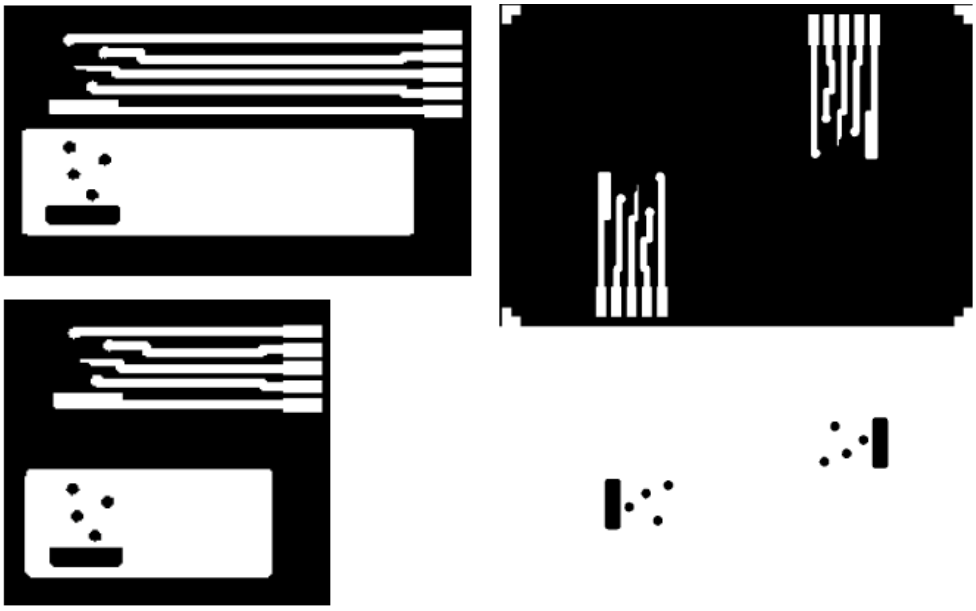

Figure 49. Three Masks Designed for Conductive and Insulating Layer of Evaporated Pt Electrode

The design in the bottom left is the same design as above, but with an inch removed from the Pt path. When deposited on a glass slide, the electrode areas are located in the center. The path could be further shortened, but this design allows to a microfluidic device to be oriented in one of two ways. The chamber could be oriented as with the SPE,

with the flow inlet in the area between the contacts and electrodes, and the outlet on the other side of the electrodes. Alternatively, the microfluidic could be oriented so that the inlet is near electrode 3, and the outlet is on the other side of the counter electrode. Both methods would allow for flow over all of the electrodes without interferents formed at one electrode interacting with another electrode. Finally, a mask was designed allowing for two sensors for be formed on one glass slide. The two sensor formed from these had to be separated by cutting the glass slide in order to undergo ion etching. A dual sensor slide may be possible once the electrode and MAMP has been further optimized and experimental set-up further simplified.

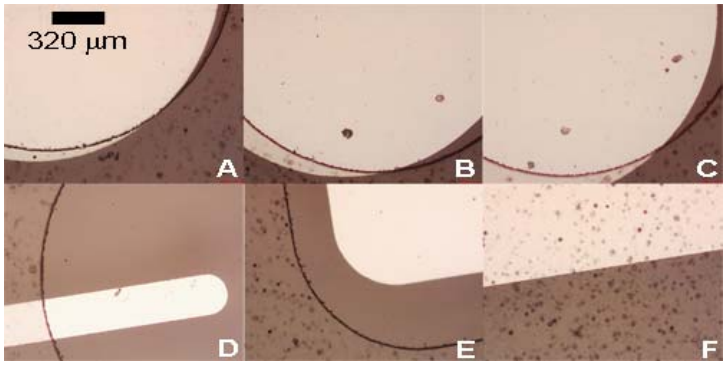

Figure 50. Images of Evaporated Platinum electrodes with SU-8 Insulation(A)-(C) are images of the three disk electrodes. (D) Bar electrode (E) Edges of Counter Electrode (F) Insulated Pt path between contacts and active electrode areas.

Figure 50 is images of the microfabricated Pt electrodes taken in bright field at 50x magnification with the Pixara camera. The platinum reflects the microscope light, and appears white. The surrounding glass does not reflect the light, and appears darker. The SU-8 layer appears bubbled, and the edges between platinum, glass, and SU-8 are visible.

A mask aligner was not used for this sensor, and the slight offset of the electrodes and the SU-8 layer can be seen.

Figure 50A, B, and C shows partial images of the three disk electrodes and of the insulating SU-8 layer. Adherence of small interferents is visible and may be photoresist left from adhering SU-8. Figure 50D shows the bar electrode intended for oxygen detection. Figure 50E and F shows a corner of the counter electrode and an image of the Pt path between the contacts and active electrodes.

Profilometry revealed a Pt thickness of 207 ± 4 nm, meaning the metal layer is 4% as thick as the printed Pt layer. This reduction in thickness will improve the sealing of a microfluidic over electrodes, as the 10 μm contours caused by Pt bars covered with ceramic will not be present.

The thickness of the SU-8 layer was measured for three substrates prepared at different times. The thickness of these substrates was found to be 2.2 μm, 3.2 μm, and 5.6 μm. While the thickness has not be optimized yet to be highly reproducible, the profile is about half of that of the SPE, which had a thickness of 9 μm. More importantly, the method in which the insulating layer is applied does not result in beading of fluid at the edges of the SU-8 film. This means that the electrode wells formed by screen-printing of the ceramic layer on the SPE will not occur when using microfabricated platinum and SU-8.

Quality electrochemical testing of the printed electrodes was performed by cyclic voltammetry in $Fe(CN)_6^{3-/4-}$. As shown in Figure 51A, the three Pt disk electrodes (Ele 1,2, and 3) are not identical, and do not reversibly reduce and oxidize the $Fe(CN)_6^{3-/4-}$ electrochemical couple. Figure 51B shows the scan at the oxygen electrode, which

conducts much less current than the larger electrodes. The poor reversibility of the electrochemical couple indicates that the platinum electrodes feature microscopic defects, which may be introduced through the platinum deposition or the photolithography process. These scans should be done with all new evaporated platinum electrodes to confirm that the electrodes are suitable for further electrochemical measurements.

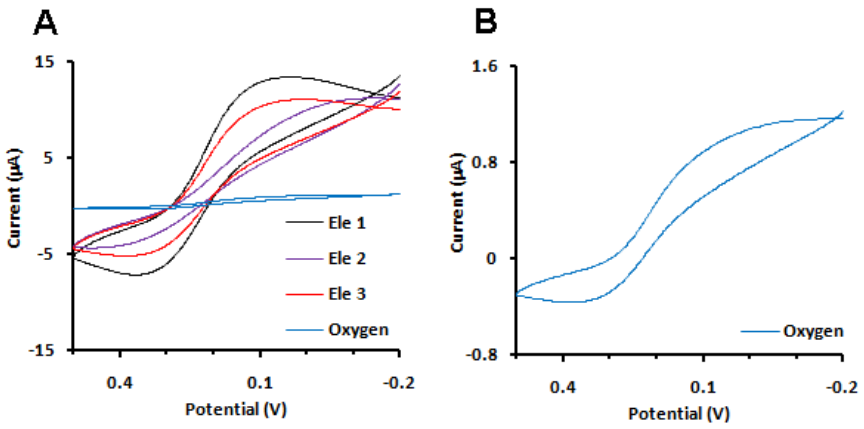

Figure 51.Cyclic voltammogram of four electrodes on the Evaporated Pt Electrode

Iridium Oxide Films on Evaporated Platinum

Iridium oxide films were formed on evaporated Pt electrodes through constant current and constant potential deposition methods. Calibrations were performed as described and photos taken before and after use. Figure 52 shows the images of films formed from both methods. Figure 52A and Figure 52B show the film from the constant potential method before and after use, respectively. The film does not appear to have changes due to use. Figure 52C and Figure 52D show the film from the constant current method before and after use, respectively. Once used, the film appears to have more defects, including a long

swipe missing due to accidental contact with a Kimwipe. An unmodified disk electrode is displayed in Figure 52E. The dark field image shows the defects present in the microfabricated Pt surface.

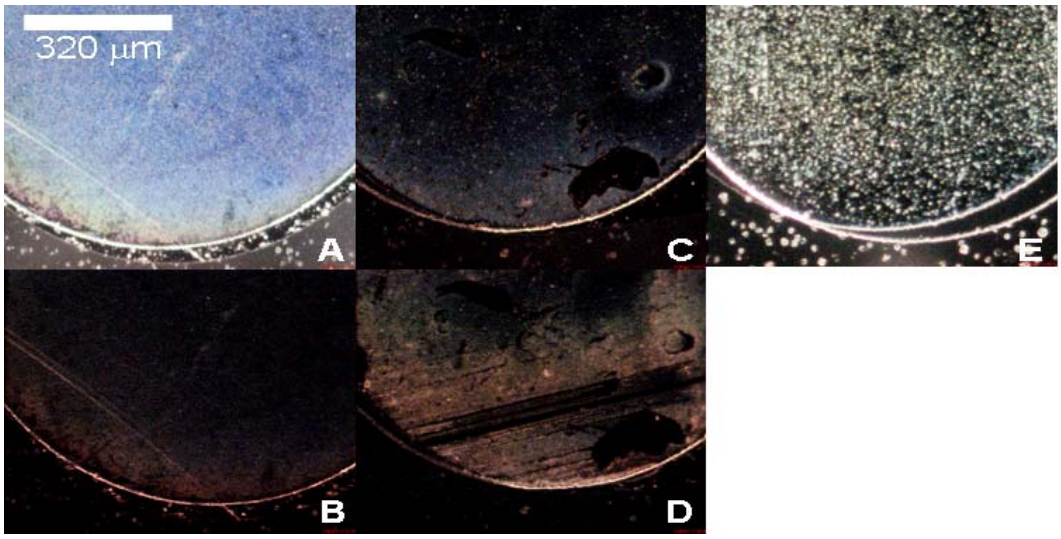

Figure 52. Iridium oxide films deposited on evaporated Pt Electrodes Film formed through constant potential method (A) before calibration (B) and after calibration. Film formed through constant current method (C) before calibration (D) and after calibration. Images were taken at 50x magnification in dark field. (E) An unmodified electrode taken in dark field is shown for comparison.

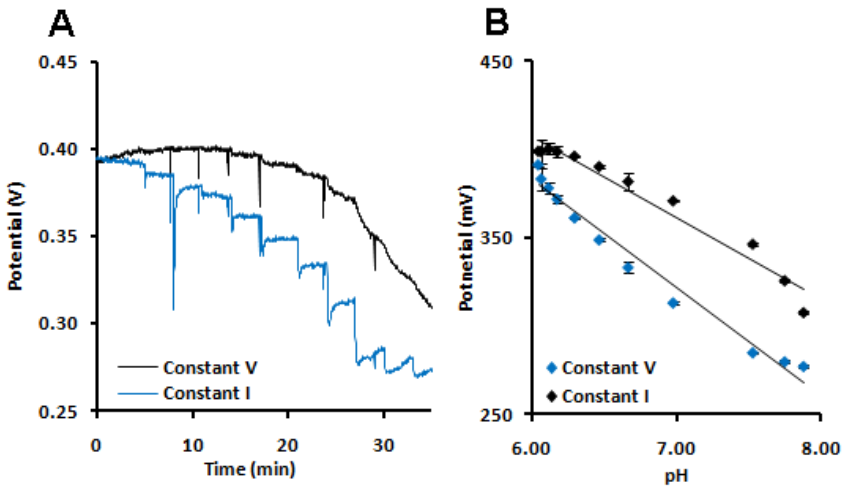

Figure 53. Simultaneous Calibration of IrOx Films formed through different methods (A) OCP measured at both electrodes as dilute NaOH was added (B) Calibration curve from (A).

Both electrodes were calibrated simultaneously, and the OCP was measured with the VIIBRE potentiometric modules. The film formed with constant potential yielded a sensitivity of -46 ± 3 mV/dec, while the constant current method yielded a Nerstian response of -61 ± 3 mv/dec. It is clear from Figure 53A that the film formed in galvanostatic mode has a much faster response time to changes in pH. The OCP of the constant potential film never reaches a constant state, despite stirring and 3 min between additions of NaOH. The fast response time and higher sensitivity show that the galvanostatic method forms better films to detect pH than the constant potential method. This method does have drawbacks, due to the low adhesion of IrOx to the Pt substrate (Figure 52D). Once formed, these films must be handled very carefully to avoid damage.

Previous work by Ges et al suggest that smaller substrates form more consistent IrOx films.[66] The performance of IrOx films formed through galvanostatic methods on either the small bar (oxygen) electrode or the disk electrode was studied (Figure 54.). Over a

wide range of pH (4-10), both sensors exhibited similar sensitivity, but the disk electrode was much less reliable. The sensitivity of the bar electrode was -68 ± 1 mv/dec, while the disk electrode had a response of -66 ± 10 mv/dec.

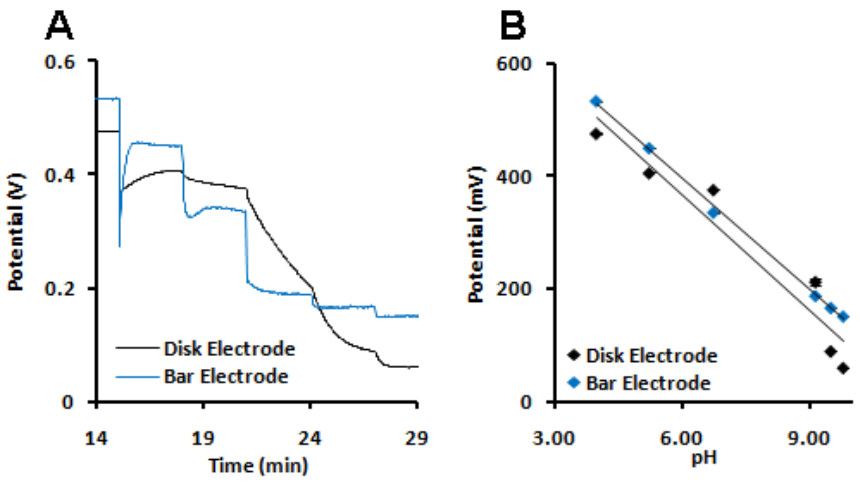

Figure 54. Calibration of IrOx films on Bar and Disk Electrodes pH 4 - 10(A) OCP measured at both electrodes as dilute NaOH was added (B) Calibration curve from (A).

The same films were also tested over a smaller pH range (6-8), which is closer to the physiological range required for MAMP experiments. While only one linear curve is plotted, yielding a sensitivity of -57 ± 4 mv/dec for the disk and -64 ± 1 mv/dec for the bar electrodes, it is clear that the electrode has two separate linear ranges from approximately pH 6-7 and pH 7-8. The higher pH linear range is shown in Figure 55.C. The disk electrode yielded a sensitivity of -107 ± 3 mv/dec, while the bar electrode yielded a super-Nerstian response of -79 ± 1 mv/dec.

The slow response of the disk electrode compared to the bar electrode prevents the OCP from reaching a steady-state. It is unclear why the disk electrode is exhibiting such a slow

response time, as a similar electrode was used to compare deposition methods did not have this issue (Figure 53). The differences may be due to electrode quality, which we have already discussed needs some improvement (Figure 51).

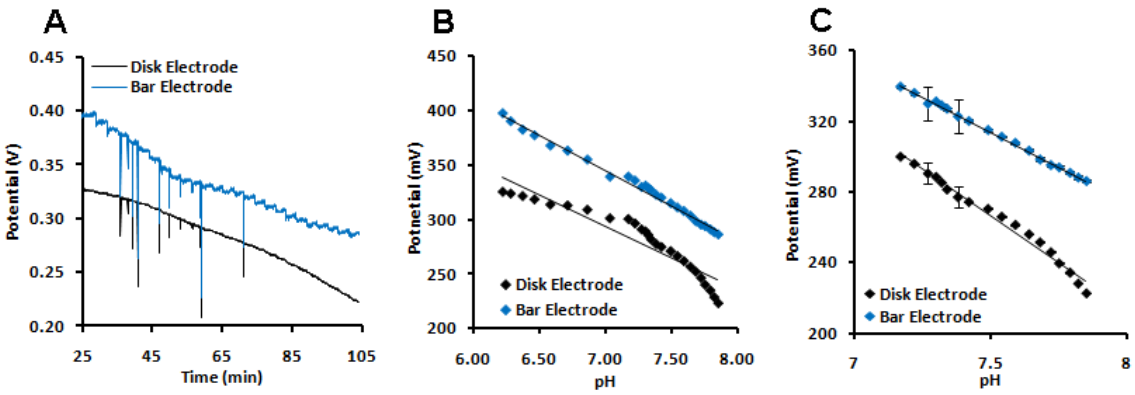

Figure 55. Calibration of IrOx films on Bar and Disk Electrodes pH 6 - 8(A) OCP measured at both electrodes as dilute NaOH was added (B) Calibration curve from (A).Figure (C) is a selected portion of (B) to illustrate the separate linear ranges observed in both electrodes.

Despite electrode differences, it seems likely that a smaller electrode will further improve the IrOx-based pH sensor. If both oxygen and pH were to be measured, some changes would have to be made in the fabrication process. A new positive mask could be designed replacing one of the disk electrodes with another small bar electrode. Alternatively, a new negative mask could be designed to increase the amount of SU-8 coverage over one disk electrode. A disk electrode would still be underneath the insulating layer, but the active electrode area would be defined by the SU-8, allowing for any electrode design smaller than the underlying Pt electrode.

Conclusions

The development of the microfabricated electrode MAMP is very near to being completed. The studies performed with the multi-analyte SPE demonstrated the benefits of the planar electrode, and highlighted issues including microfluidic collapsibility and the perils of uneven contours on the sensor surface. The benefits of the planar electrode, including low-cost, reproducibility, and simple integration with a microfluidic device can be realized with the multi-analyte microfabricated Pt electrode. While the fabrication process is still undergoing optimization, once stable electrodes have been achieved, they can be coupled with the photo-curable PDMS devices created by Dr. Leslie Hiatt to form the next-generation MAMP.

Acknowledgements

This work was supported by NIH grant U01 AI 061223, Defense Threat Reduction Agency grant HDTRA1-09-1-0013, the Vanderbilt Institute for Integrative Biosystems Research and Education, and DOE fellowship Graduate Assistance in Areas of National Need. This work would not have been possible without collaborations with and use of instruments associated with Vanderbilt's Institute of Integrative Biosystem Research and Education. Collaborations with and assistances from Dr. Leslie Hiatt, Ron Reiserer, and Dr. Igor Ges were essential.

APPENDIX B

TESTING OF NEW POTENTIOMETRIC MODULE FOR THE VIIBRE MULTIPOTENTIOSTAT*

* This work details the author's involvement in the development of the multianalyte potentiostat, including testing of the new potentiometric module, and interference studies between the amperometric module, potentiometric module, and LAPS. For a detailed review of the potentiostat hardware and software development, please refer to the dissertation of Dr. Rachel M. Snider, "Development of Multianalyte Microphysiometry for the Study of Islets and Biological Toxins".

We have previously shown that real-time electrochemical monitoring of cellular metabolism can yield a wealth of information about cellular energetics.[40] Multi-analyte microphysiometry, which uses several electrochemical sensors to simultaneously monitor the metabolism of cells housed in a microfluidic chamber, is uniquely poised to explore metabolic flux due to alterations in cell regulation in real-time. In order to measure the flux of several metabolites together in one chamber, a potentiostat is required that can measure the electrochemical changes at amperometric and potentiometric sensors together. The potentiostat also requires several individual chambers to allow for simultaneous recording in replicate chambers.

In order to measure multiple analytes in several electrochemical cells simultaneously, a multichamber multipotentiostat was created that can also incorporate multichamber potentiometric sensing. This multichamber multipotentiostat was built upon a custom

modular framework that allows up to eight modules to operate concurrently while being controlled by a single personal computer. Two different types of modules were designed, implementing either a multi-channel amperometric module or a multi-channel potentiometric module.

Each of the multipotentiostat modules controls three working electrodes (WE), two of which share the same applied potential, and one of which has a separate WE potential as in a conventional adder bipotentiostat.[109] Each potentiometric module implements three independent potentiometric channels, referenced to different electrodes. To avoid using additional reference electrodes and to minimize possible interference with the multipotentiostat modules, the pH sensors operate in differential mode. Therefore, virtually no current is impressed on and no potential is applied to a reference electrode shared by a potentiometric circuit and an amperometric circuit. This multi-chamber multichannel potentiostat enables us to monitor multiple analytes in different fluidic chambers simultaneously. In the MAMP, this instrument has been used to measure glucose, lactate, oxygen, and pH simultaneously.[40] A great degree of flexibility is achieved with this instrument, given that different combinations of amperometric and potentiometric modules can be used to best match the experiment at hand. In addition, our instrument allows for the incorporation of new modules that might eventually be developed in the future to modify or expand its current capabilities. Thus, this instrument is essential to developing additional techniques for performing microphysiometry independent of the Cytosensor microphysiometer.

Calibration of the pH Modules

Once installed, the potentiometric modules require calibration. Dr. Lima built a battery-operated ancillary circuit that contains high-accuracy sub-band gap voltage reference chips and precision resistor bridges that generate a set of ten different dc voltages between 0.0 V and 1.0 V. These voltages are fed sequentially to each of the three channels of a pH module through the respective minigrabbers, and the averaged values output by the DAQ card are stored in a spreadsheet. Based on the nominal and actual voltages, a best-fit line is calculated and its intercept and angular coefficient give the offset voltage and calibration factor, respectively. This calibration procedure is repeated for each installed pH module. The calibration factor for each channel is written into the LabView program.

Interference Studies

The current MAMP couples potentiometric detection of pH though a LAPS with amperometric detection of glucose, lactate, and oxygen. Simultaneous sampling by the Cytosensor instrument and multi-potentiostat has the potential to introduce additional noise into measured signals. For this reason, studies were performed with the multipotentiostat and the MAMP to determine the noise contamination that occurs in both the LAPS and amperometric signals at various potentiostat sampling rates. Sensor heads with bare Pt electrodes were assembled in MAMP chambers containing no cells. The potentiostat mingrabbers were attached to the electrodes to measure current at WE 1, 2, and 3. Modified RPMI was perfused through the chamber at 100 μL/min continuously

while the LabView program was started and stopped to change the sampling frequency of the potentiostat. Without turning on the potentiostat, the Cytosoft program was begun, initiating measurement of potential at the LAPS located in the bottom of the sensor chamber. At five minutes, the potentiostat was turned on, and the LabView program initiated to sample the current at WE 1,2, and 3 at 1 Hz for 5 min. The WEs were held at the potentials traditionally used for MAMP experiments, +0.6 V for WE 1 and 2, and -0.45 V for WE 3. Sensitivities were set at 100 nA/V, which is typical for the magnitude of current observed with these electrodes. After 1 min, the LabView program was started again to sample at 5 Hz for 5 min. This was continued for 10 Hz and 0.5 Hz sampling rates, including 1 min breaks between sampling periods. The LAPS was then turned off, and flow continued at 100 μL/min, while the 5 min sampling periods at each frequency was repeated.

The signals measured at both the LAPS and potentiostat were then analyzed to calculate the increase in noise that occurs due to simultaneous use. For the LAPS signal, the last 100 s of each potentiostat sampling period (0, 0.5, 1, 5, 10 Hz) was averaged and the standard deviation calculated. For the potentiostat signals, the last 100 sec of each sampling period, with and without simultaneous sampling by the LAPS, was averaged and the standard deviation calculated. The average current magnitude is dependent on electrode size and applied potential, therefore the percent standard error was calculated to allow for comparison.

Future generations of the MAMP will require potentiometric sensing of pH independent of the Cytosensor, and will require the potentiometric module of the potentiostat. No sensor head was available with four Pt electrodes to show that noise is

not increased due to simultaneous use of all of the amperometric and potentiometric channels of the potentiostat. In its place, a multi-analyte s SPE featuring three Pt disk electrodes with areas of 1.8 mm^2 intended for glucose, lactate, and pH detection, one electrode with a total area of 0.08 mm^2 intended for oxygen detection, and an electrode with an area of 19 mm^2 to act as the counter electrode. The SPE was designed in house and printed by Pine Research Instrumentation. A 1-in card edge connector modified with five male pins was used to create electrical contacts for connection to the potentiostat.

The amperometric modules could be tested using bare electrodes, however, measuring OCP at a bare Pt electrode results in potentials in excess of 0.9 V and bubble formation at the electrode. Instead, one disk electrode was coated with an IrOx film sensitive to changes in pH. The film was formed from a solution prepared as previously described.[65] The bare Pt sensor was placed in a stirred iridium oxalate solution, along with a mesh counter electrode and Ag/AgCl (2 M KCl) reference electrode. The desired electrode on the sensor was then held at +0.6V for 10 min, forming a dark blue film consisting of iridium complexes. The sensor was stored in phosphate buffered saline at 4 °C for at least two days to allow for film stabilization.

The SPE featuring three bare WEs, and IrOx electrode, and a counter electrode were then placed in 10 mL of modified RPMI media with a Ag/AgCl (2 M KCl) reference electrode. Minigrabbers from the potentiostat were connected to the male pins of the card edge connector and both the amperometric and OCP modules were connected to the same reference electrode. The LabView program was run for 5 min at each frequency (0.5, 1, 5, 10 Hz) three times: once with both amperometric and OCP were collected, once where only the amperometric signals were collected, and once where only OCP was collected.

The last 100 s of each sampling period was averaged and the standard deviation calculated. The average current magnitude is dependent on electrode size and applied potential, therefore the percent standard error was calculated to allow for comparison.

Combined Amperometric and Open Circuit Potential Experiments

In order to test the utility of the pH module in MAMP experiments, WE1 in the MAMP sensor head was plated with an IrOx film instead of glucose oxidase. Electrochemical deposition of the IrOx film was achieved by holding the electrode in solution at + 0.6 V *vs* Ag/AgCl (2 M KCl) with the amperometric modules of the VIIBRE potentiostat for 7 min. These films were prepared one day prior to microphysiometry experiments, and sensor heads were stored in phosphate buffer at 4 °C. Lactate and oxygen electrodes were prepared as in previous MAMP experiments.

The pH module was tested using cortical cultures from day 18 Sprague-Dawley rats prepared as previously described.[8, 9] These mixed cultures (80% glial/20% cortical neuron cultures) were plated in Corning Costar® Transwell® cup assemblies at two times the density previously described.[9] The sensors were placed into cup assemblies containing the cells. Oxygen consumption and lactate production were measured with the amperometric modules, and acid production was measured with both the Cytosensor and the pH modules.

The Cytosensor program and potentiostat were started as the chamber was perfused with 5 mM glucose modified RPMI 1640 media for 2 hrs and 30 min. The media was then changed to modified RPMI 1640 media containing 5 mM glucose and 75 μM alamethicin for 25 minutes before returning to 5 mM glucose RPMI media. After zero metabolic activity was achieved, the sensors were calibrated via perfusion of modified

RPMI with added lactate and adjusted to specific pH. Four calibration solutions covering the following range of physiologically relevant concentrations: 0 mM lactate, pH 7.48; 0.05 mM lactate, pH 7.31; 0.1 mM lactate, pH 7.21; and 0.2 mM lactate, pH 7.08.

Molar lactate production per stop flow period was calculated by comparing Δi_p to calibrations at the end of each experiment. Molar oxygen was calculated by assuming the oxygen baseline of dead cells to be the concentration of dissolved oxygen, 0.24 mM, and was calculated as described previously.[43] Acidification rates in μV/s were calculated from measured OCP using graphing software in the same manner as the Cytosensor program.

Results and Discussion

Calibration of the pH Modules

Calibration of the pH modules was performed using a set of fixed voltages provided by an ancillary custom circuit. The coefficients of the best fit lines determine the correction that should be made to the voltages read from the DAQ card. For comparison purposes, we also show (calibrated) data obtained with a commercial CH Instruments electrochemical analyzer model 660A (Figure 56). The module can measure OCP reliably up to 0.8 V. Above this potential, the module reaches a saturation point that is different in every module. This will not affect pH measurements, as OCPs in that range would not be expected.

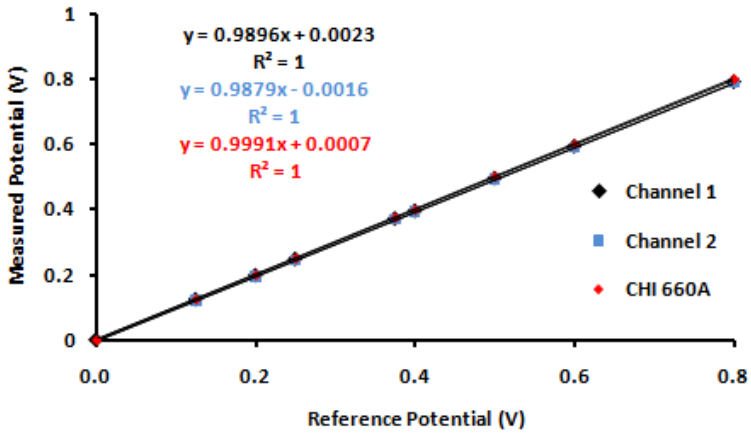

Figure 56. Calibration of the pH modules by a set of fixed voltages provided by an ancillary custom circuit.

Interference Studies

Interference studies were performed with the multipotentiostat and the Cytosensor instrument to determine the noise contamination that occurs due to simultaneous sampling by the instruments. The standard error in the signal of the Cytosensor LAPS operating alone was 0.10 mV. When the potentiostat was simultaneously sampling at 0.5, 1, 5, or 10 Hz, the standard error in the Cytosensor signal increased almost three-fold, to 0.28 ± 0.03 mV (Figure 57.). As the total change in potential during a stop-flow can be on the order of 1 mV, this substantial increase is significant. No increase in noise of the signals collected by the multipotentiostat were observed, where a percent standard error of 3.5 ± 1.4% when the LAPS was simultaneously sampling and 3.3 ± 1.7% error when the multipotentiostat was working independently of the LAPS.

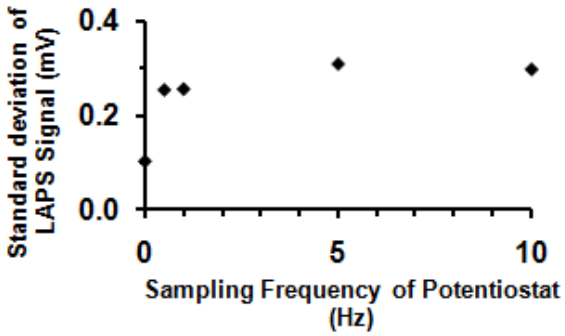

Figure 57. Signal noise of the LAPS increases when potentiostat is sampling at any frequency.

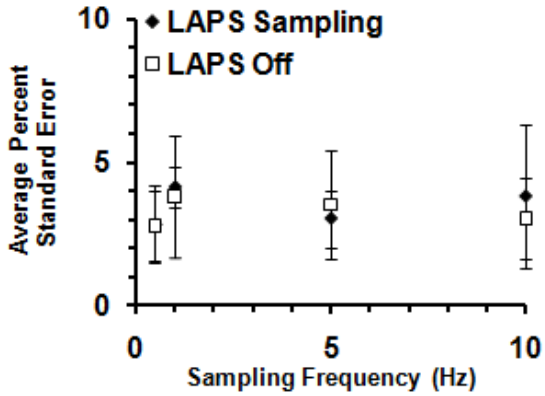

Figure 58. Signal noise of the amperometric WEs do not increase when the LAPS is sampling.

Interference studies were performed with both modules to determine the noise contamination that occurs due to simultaneous sampling. No increases in noise were observed in either amperometric or potentiometric signals when sampled together. The signals of the amperometric and potentiometric modules had a standard error of 1.2 ± 0.8% and 0.110 ± 0.06%, respectively. When sampled independently, the signals of the amperometric modules and potentiometric modules had a standard error of 1.0 ± 0.6% and 0.027 ± 0.004%, respectively.

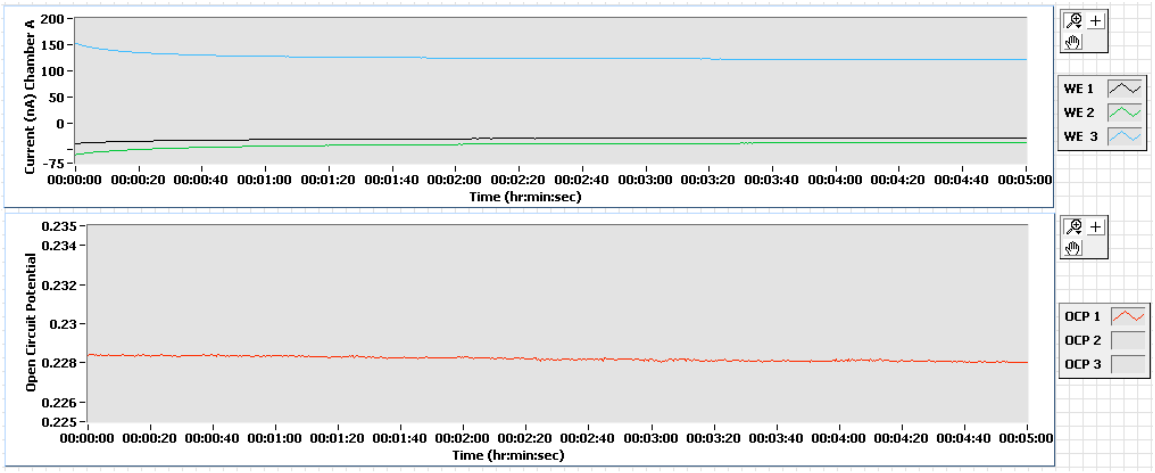

Figure 59. Screenshot of LabView multipotentiostat interface of a typical current response and potentiometric response during interference testing. Both modules were sampled simultaneously for 5 min at 0.5 Hz.

These studies demonstrated that the multipotentiostat module is not significantly affected by simultaneous sampling by a high frequency instrument (Cytosensor) or by the addition of the potentiometric module. The high noise of the Cytosensor compared to the low noise of the potentiometric modules illustrates the need for new MAMP instrumentation independent of the Cytosensor. A screen-shot of one channel of each module working simultaneously is shown in Figure 59.

Combined Amperometric and Open Circuit Potential Experiments

The open-circuit potential module was tested during an MAMP experiment measuring the metabolic rates of co-cultures of primary neurons and glia. Cells and sensors were prepared as described in methods. Figure 60A shows the simultaneous measurement of lactate, oxygen, and pH using the MAMP and the amperometric and potentiometric modules of the potentiostat. Lactate and oxygen electrodes behave as before, with lactate production indicated by an increase in current magnitude during stop-flows, and oxygen

consumption indicated by a decrease in current magnitude during stop-flow. The OCP module allowed for detection of acid independent of the Cytosensor, and in conjunction with the IrOx electrode, yielded ECAR with very low noise. Due to the nature of primary mixed cultures, the metabolic rate in mol·cell^{-1}·s^{-1} could not be calculated, and molar lactate production and molar oxygen consumption per stop flow were calculated along with ECAR (Figure 60B).

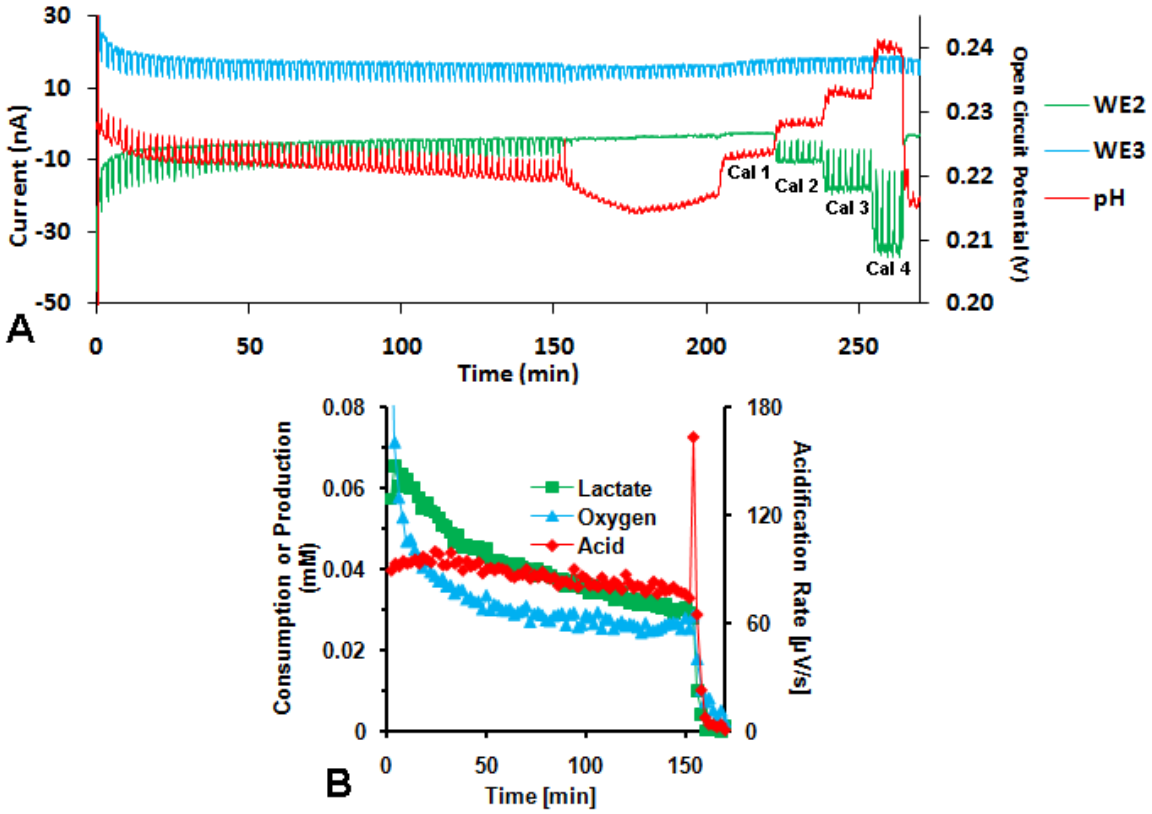

Figure 60. Typical current and open circuit potential response at modified sensor head during MAMP experiment. Sensors with appropriate electrode coatings were assembled in chamber primary mixed neuronal/glial cultures and perfused with 5 mM glucose RPMI media. (A) Raw current and OCP measured over the course of the experiment. (B) Lactate production, oxygen consumption, and acid production as calculated from data gathered in (A).

Conclusion

We have developed a flexible low-cost multichamber multipotentiostat system capable of simultaneously measuring amperometric current response of three working electrodes in combination with open circuit potentials in up to eight electrochemical cell chambers at a controlled bandwidth. The multipotentiostat works with sensitivities of 1, 10, 100, or 1000 nA/V, selectable by software. pH measurements are done at a fixed sensitivity range of ±1.0 V. Additionally, this range, could be easily changed by just replacing three resistors in the pH module, which may allow for detection using other potentiometric sensors. We successfully tested continuous data collection for as long as ten hours. Sampling rates as high as 15 Hz can also be used, and analog filters with a fixed bandwidth of 7.5 Hz present in the multipotentiostat cards help reduce possible high frequency noise originating from crosstalk in the electrochemical cell between the Cytosensor and potentiostat electrodes when LAPS pH measurement is used.

This multipotentiostat system is applicable to any system requiring amperometric and OCP measurements in multiple electrochemical cells simultaneously, such as in an instrumented well plate. The only peculiarity is that the current design is limited to the application of two potentials; however, this is not a significant issue so long as two of the analytes have similar reduction or oxidation potentials.

The use of this multipotentiostat increases the number of MAMP chambers that could be measured simultaneously from one to eight, allowing for simultaneous testing of multiple cell types or exposures or simply allowing replicate experiments to be run simultaneously. In total, eight units were built, tested, and are presently being used in

experiments. Currently, efforts are underway to integrate amperometric detection of superoxide and new potentiometric measurements of Ca^{2+}.

Acknowledgements

This work was supported by NIH grant U01 AI 061223, Defense Threat Reduction Agency grant HDTRA1-09-1-0013, and the Vanderbilt Institute for Integrative Biosystems Research and Education.

REFERENCES

1. Ray, L. B. Metabolism Is Not Boring. *Science*, **330**, 1337.

2. Wong, W. Focus Issue: Metabolic Signals. *Sci Signal*, **3**, eg12-.

3. McKnight, S. L. On Getting There from Here. *Science*, **330**, 1338-1339.

4. Ray, L. B. Connecting Signaling and Metabolism in Cancer. *Sci Signal*, **3**, ec380-.

5. Boucher, J., Macotela, Y., Bezy, O., Mori, M. A., Kriauciunas, K. and Kahn, C. R. A Kinase-Independent Role for Unoccupied Insulin and IGF-1 Receptors in the Control of Apoptosis. *Sci Signal*, **3**, ra87-.

6. Eklund, S., Thompson, R., Snider, R., Carney, C., Wright, D., Wikswo, J. and Cliffel, D. (2009) Metabolic Discrimination of Select List Agents by Monitoring Cellular Responses in a Multianalyte Microphysiometer. *Sensors*, **9**, 2117-2133.

7. Snider, R., McKenzie, J. R., Kraft, L., Kozlov, E., Wikswo, J. P. and Cliffel, D. E. (2010) The Effects of Cholera Toxin on Cellular Energy Metabolism. *Toxins*, **2**, 632-648.

8. Zeiger, S. L. H., McKenzie, J. R., Stankowski, J. N., Martin, J. A., Cliffel, D. E. and McLaughlin, B. (2010) Neuron specific metabolic adaptations following multi-day exposures to oxygen glucose deprivation. *Biochim Biophys Acta Mol Basis Dis*, **1802**, 1095-1104.

9. Brown, J. E., Zeiger, S. L. H., Hettinger, J. C., Brooks, J. D., Holt, B., Morrow, J. D., Musiek, E. S., Milne, G. and McLaughlin, B. (2010) Essential role of the redox-sensitive kinase p66shc in determining energetic and oxidative status and cell fate in neuronal preconditioning. *Journal of Neuroscience*, **30**, 5242-5252.

10. McLaughlin, B., Hartnett, K. A., Erhardt, J. A., Legos, J. J., White, R. F., Barone, F. C. and Aizenman, E. (2003) Caspase 3 activation is essential for neuroprotection in preconditioning. *Proc Natl Acad Sci U S A*, **100**, 715-720.

11. Chijiwa, T., Mishima, A., Hagiwara, M., Sano, M., Inoue, T., Naito, K., Toshioka, T. and Hidaka, H. (1990) Inhibition of forskolin-induced neurite outgrowth and protein phosphorylation by a newly synthesized selective inhibitor of cyclic AMP-dependent protein kinase, N-[2-(p-bromocinnamylamino)ethyl]-5-

isoquinolinesulfonamide (H-89), of PC12D pheochromocytoma cells. *J Biol Chem*, **265**, 5267-5272.

12. McKay, D. M. and Singh, P. K. (1997) Superantigen activation of immune cells evokes epithelial (T84) transport and barrier abnormalities via IFN-γand TNF-α Inhibition of increased permeability, but not diminished secretory responses by TGF-α. *J Immunol*, **159**, 2382-2390.

13. Zeiger, S. L. H., Musiek, E. S., Zanoni, G., Vidari, G., Morrow, J. D., Milne, G. J. and McLaughlin, B. (2009) Neurotoxic lipid peroxidation species formed by ischemic stroke increase injury. *Free Radic Biol Med*, **47**, 1422-1431.

14. Sofer, A. and Futerman, A. H. (1996) Rate of Retrograde Transport of Cholera Toxin from the Plasma Membrane to the Golgi Apparatus and Endoplasmic Reticulum Decreases During Neuronal Development. *J Neurochem*, **67**, 2134-2140.

15. Sofer, A. and Futerman, A. H. (1995) Cationic amphiphilic drugs inhibit the internalization of cholera toxin to the Golgi apparatus and the subsequent elevation of cyclic AMP. *J Biol Chem*, **270**, 12117-12122.

16. Lencer, W. I., Strohmeier, G., Moe, S., Carlson, S. L., T., C. C. and Madara, J. L. (1995) Signal Transduction by cholera toxin: processing in vesicular compartments does not require acidification. *Am J Physiol*, **269**, G548-557.

17. Lencer, W. I., Moe, S., Rufo, P. A. and Madara, J. L. (1995) Transcytosis of cholera toxin subunits across model human intestinal epithelia. *Proc Natl Acad Sci USA*, **92**, 10094-10098.

18. Hamad, A. R. A., Marrack, P. and Kappler, J. W. (1997) Transcytosis of Staphylococcal Superantigen Toxins. *J Exp Med*, **185**, 1447-1454.

19. Shupp, J. W., Jett, M. and Pontzer, C. H. (2002) Identification of a Transcytosis Epitope on Staphylococcal Enterotoxins. *Infect Immun*, **70**, 2178-2186.

20. Beharka, A. A., Armstrong, J. W., Iandolo, J. J. and Chapes, S. K. (1994) Binding and activation of major histocompatibility complex class II-deficient macrophages by staphylococcal exotoxins. *Infect Immun*, **62**, 3907-3915.

21. Reddy, R., Smith, D., Wayman, G., Wu, Z., Villacres, E. C. and Storm, D. R. (1995) Voltage-sensitive adenylyl cyclase activity in cultured neurons. A calcium-independent phenomenon. *J Biol Chem*, **270**, 14340-14346.

22. Milani, D., Minozzi, M. C., Petrelli, L., Guidolin, D., Skaper, S. D. and Spoerri, P. E. (1992) Interaction of ganglioside GM1 with the B subunit of cholera toxin

modulates intracellular free calcium in sensory neurons. *J Neurosci Res*, **33**, 466-475.

23. Kurien, B. T. and Scofield, R. H. Introduction to Protein Blotting, 2009; Vol. 536, pp 9-22.

24. Musch, M. W., Petrof, E. O., Kojima, K., Ren, H., McKay, D. M. and Chang, E. B. (2004) Bacterial Superantigen-Treated Intestinal Epithelial Cells Upregulate Heat Shock Proteins 25 and 72 and are Resistant to Oxidant Cytotoxicity. *Infect Immun*, **63**, 539-546.

25. Lorsbach, R. B., Murphy, W. J., Lowenstein, C. J., Snyder, S. H. and Russell, S. W. (1993) Expression of the nitric oxide synthase gene in mouse macrophages activated for tumor cell killing. Molecular basis for the synergy between interferon-γ and lipopolysaccharide. *J Biol Chem*, **268**, 1908-1913.

26. Fishman, P. H. (1980) Mechanism of Action of Cholera Toxin: Studies on the Lag Period. *J Membrane Biol*, **54**, 61-72.

27. Lando, P. A., Olsson, C., Kalland, T., Newton, D., Kotb, M. and Dohlsten, M. (1996) Regulation of Superantigen-Induced T Cell Activation in the Absence and the Presence of MHC Class II. *J Immunol*, **157**, 2857-2863.

28. Fleming, S. D., Iandolo, J. J. and Chapes, S. K. (1991) Murine macrophage activation by staphylococcal exotoxins. *Infect Immun*, **59**, 4049-4055.

29. Yang, Y. and Balcarcel, R. R. (2004) 96-Well Plate Assay for Sublethal Metabolic Activity. *Assay and Drug Dev Technol*, **2**, 353-361.

30. LeClaire, R. D., Kell, W. M., Sadik, R. A., Downs, M. B. and Parker, G. W. (1995) Regulation of staphylococcal enterotoxin B-elicited nitric oxide production by endothelial cells. *Infect Immun*, **63**, 539-546.

31. Bittner, C. X., Loaiza, A., Ruminot, I., Larenas, V., Sotelo-Hitschfeld, T., Gutierrez, R., Cordova, A., Valdebenito, R., Frommer, W. B. and Barros, L. F. (2010) High resolution measurement of the glycolytic rate. *Front Neuroenerg*, **2**.

32. Barros, L. F. (2010) Towards single-cell real-time imaging of energy metabolism in the brain. *Front Neuroenerg*, **2**.

33. Casciari, J. J., Sotirchos, S. V. and Sutherland, R. M. (1992) Variations in tumor cell growth rates and metabolism with oxygen concentration, glucose concentration, and extracellular pH. *J Cell. Phys.*, **151**, 386-394.

34. Sanfeliu, A., Paredes, C., Cairo, J. J. and Godia, F. (1997) Identification of key patterns in the metabolism of hybridoma cells in culture. *Enzyme Microb Technol*, **21**, 421-428.

35. Ges, I. A. and Baudenbacher, F. (2010) Enzyme electrodes to monitor glucose consumption of single cardiac myocytes in sub-nanoliter volumes. *Biosens and Bioelectron*, **25**, 1019-1024.

36. Owicki, J. C., Bousse, L. J., Hafeman, D. G., Kirk, G. L., Olson, J. D., Wada, H. G. and Parce, J. W. (1994) The light-addressable potentiometric sensor: principles and biological applications. . *Annu Rev Biophys Biomol Struct*, **23**, 87-113.

37. Hafner, F. (2000) Cytosensor ® Microphysiometer: technology and recent applications. *Biosens and Bioelectron*, **15**, 149-158.

38. Cao, C. J., Mioduszewski, R. J., Menking, D. E., Valdes, J. J., Cortes, V. I., Eldefrawi, M. E. and Eldefrawi, A. T. (1997) Validation of the cytosensor for in vitro cytotoxicity studies. *Toxicol. In Vitro*, **11**, 285-293.

39. Eklund, S. E., Cliffel, D. E., Kozlov, E., Prokop, A., Wikswo, J. and Baudenbacher, F. (2003) Modification of the Cytosensor(TM) microphysiometer to simultaneously measure extracellular acidification and oxygen consumption rates. *Anal Chim Acta*, **496**, 93-101.

40. Eklund, S. E., Kozlov, E., Taylor, D. E., Baudenbacher, F. and Cliffel, D. E. Real Time Cell Dynamics With a Multianalyte Physiometer In *Methods in Molecular Biology*; Rosenthal, S. J., Wright, D. W., Eds.; Humana Press Inc: Totowa, NJ, 2005; Vol. 303, pp 209.

41. Eklund, S. E., Snider, R. M., Wikswo, J., Baudenbacher, F., Prokop, A. and Cliffel, D. E. (2006) Multianalyte microphysiometry as a tool in metabolomics and systems biology. *J Electroanal Chem*, **587**, 333-339.

42. Eklund, S. E., Taylor, D., Kozlov, E., Prokop, A. and Cliffel, D. E. (2004) A Microphysiometer for Simultaneous Measurement of Changes in Extracellular Glucose, Lactate, Oxygen, and Acidification Rate. *Anal. Chem.*, **76**, 519-527.

43. Kety, S. S. The general metabolism of the brain in vivo In *Metabolism of the Nervous System*; Richter, D., Ed.; Pergamon Press: London, 1957, pp 221-237.

44. Kety, S. S. and Schmidt, C. F. (1948) The nitrous oxide method for the quantitative determination of cerebral blood flow in man: theory, procedure and normal values. *J Clin Investig*, **27**, 476-483.

45. Peters, A. and Langemann, D. (2009) Build-ups in the supply chain of the brain: on the neuroenergetic cause of obesity and type 2 diabetes mellitus. *Front Neuroenerg.*, **2**, 12.

46. Gidday, J. M. (2006) Cerebral preconditioning and ischaemic tolerance. *Nat Rev Neurosci*, **7**, 437-448.

47. O'Duffy, A. E., Bordelon, Y. M. and McLaughlin, B. (2006) Killer proteases and little strokes-how the things that do not kill you make you stronger. *J Cereb Blood Flow Metab*, **27**, 655-668.

48. Dahl, N. A. and Balfour, W. M. (1964) Prolonged anoxic survival due to anoxia pre-exposure: brain ATP, lactate, and pyruvate. *Am J Physiol*, **207**, 452-456.

49. Kloner, R. A. and Rezkalla, S. H. (2006) Preconditioning, postconditioning and their application to clinical cardiology. *Cardiovasc Res*, **70**, 297-307.

50. Yellon, D. M. and Downey, J. M. (2003) Preconditioning the myocardium: from cellular physiology to clinical cardiology. *Physiol Rev*, **83**, 1113-1151.

51. Serafin, A., Fernandez-Zabalegui, L., Prats, N., Wu, Z. Y., Rosello-Catafau, J. and Peralta, C. (2004) Ischemic preconditioning: tolerance to hepatic ischemia-reperfusion injury. *Histol Histopathol*, **19**, 281-289.

52. Xu, C., Yu, C. and Li, Y. (2008) Current studies on therapeutic approaches for ischemia/reperfusion injury in steatotic livers. *Hepatol Res*, **38**, 851-859.

53. Gross, G. J. (2005) Remote preconditioning and delayed cardioprotection in skeletal muscle. *Am J Physiol*, **289**, R1562-R1563.

54. Lepore, D. A., Knight, K. R., Anderson, R. L. and Morrison, W. A. (2001) Role of priming stresses and Hsp70 in protection from ischemia-reperfusion injury in cardiac and skeletal muscle. *Cell Stress Chaperon.*, **6**, 93-96.

55. Mallick, I. H., Yang, W., Winslet, M. C. and Seifalian, A. M. (2004) Ischemia-Reperfusion Injury of the Intestine and Protective Strategies Against Injury. *Dig Dis Sci*, **49**, 1359-1377.

56. Nath, K. A. (2007) Renal response to repeated exposure to endotoxin: Implications for acute kidney injury. *Kidney Int*, **71**, 477-479.

57. Trapp, S. and Ashcroft, F. (1997) A Metabolic Sensor in Action: News From the ATP-Sensitive K+-Channel. *Physiology*, **12**, 255-263.

58. Rossi, D. J., Brady, J. D. and Mohr, C. (2007) Astrocyte metabolism and signaling during brain ischemia. *Nat Neurosci*, **10**, 1377-1386.

59. Schurr, A. (2006) Lactate: the ultimate cerebral oxidative energy substrate? *J Cereb Blood Flow Metab*, **26**, 142-152.

60. Aguilera, P., Vazquez-Contreras, E., Gomez-Martinez, C. D. and Cardenas, M. E. C. (2009) Hypoxia inducible factor-1 as a therapeutic target in cerebral ischemia. *Curr Signal Transduction Ther*, **4**, 162-173.

61. Smith, D., Pernet, A., Hallett, W. A., Bingham, E., Marsden, P. K. and Amiel, S. A. (2003) Lactate: A Preferred Fuel for Human Brain Metabolism In Vivo. *J Cereb Blood Flow Metab*, **23**, 658-664.

62. Magistretti, P. J. and Pellerin, L. (1999) Astrocytes Couple Synaptic Activity to Glucose Utilization in the Brain. *Physiology*, **14**, 177-182.

63. Chen, Y., Stevens, B., Chang, J., Milbrandt, J., Barres, B. A. and Hell, J. W. (2008) NS21: Re-defined and modified supplement B27 for neuronal cultures. *J Neurosci Methods*, **171**, 239-247.

64. Milne, G. L., Sanchez, S. C., Musiek, E. S. and Morrow, J. D. (2007) Quantification of F2-isoprostanes as a biomarker of oxidative stress. *Nat Protoc*, **2**, 221(226).

65. McLaughlin, B., Pal, S., Tran, M. P., Parsons, A. A., Barone, F. C., Erhardt, J. A. and Aizenman, E. (2001) p38 Activation Is Required Upstream of Potassium Current Enhancement and Caspase Cleavage in Thiol Oxidant-Induced Neuronal Apoptosis. *J Neurosci*, **21**, 3303-3311.

66. Jin, L., Jin, P., Ye, J. and Fang, Y. (1992) Determination of dissolved oxygen by catalytic reduction on Nafion-methyl viologen chemically modified electrode. *Talanta*, **39**, 145-147.

67. Ges, I. A., Ivanov, B. L., Schaffer, D. K., Lima, E. A., Werdich, A. A. and Baudenbacher, F. J. (2005) Thin-film IrOx pH microelectrode for microfluidic-based microsystems. *Biosens and Bioelectron*, **21**, 248-256.

68. Marzouk, S. A. M., Ufer, S., Buck, R. P., Johnson, T. A., Dunlap, L. A. and Cascio, W. E. (1998) Electrodeposited Iridium Oxide pH Electrode for Measurement of Extracellular Myocardial Acidosis during Acute Ischemia. *Anal. Chem.*, **70**, 5054-5061.

69. Sack, D. A., Sack, R. B., Nair, G. B. and Siddique, A. K. (2004) Cholera. *Lancet*, **363**, 223-233.

70. Finkelstein, R. A. Cholera, VIbrio cholerae O1 and O139, and other Pathogenic Vibrios In *Medical Microbiology,* 4th ed.; Baron, S., Ed.; University of Texas Medical Branch: Galveston, Texas, 1996.

71. Olivier, V., Salzman, N. H. and Fullner Satchell, K. J. (2007) Prolonged Colonization of Mice by Vibrio cholerae El Tor O1 Depends on Accessory Toxins *Infect Immun*, **75**, 5043-5051.

72. Lundgren, O. (2002) Enteric nerves and diarrhoea. *Pharmacol Toxicol*, **90**, 109-120.

73. Lencer, W. I. and Tsai, B. (2003) The intracellular voyage of cholera toxin: going retro. *Trends Biochem.*, **28**, 639-645.

74. Eklund, S. E., Thompson, R. G., Snider, R. M., Carney, C. K., Wright, D. W., Wikswo, J. and Cliffel, D. E. (2009) Metabolic discrimination of select list agents by monitoring cellular responses in a multianalyte microphysiometer. *Sensors*, **9**, 2117-2133.

75. Lencer, W. I., Strohmeier, G., Moe, S., Carlson, S. L., T., C. C. and Madara, J. L. (1995) Signal Transduction by cholera toxin: processing in vesicular compartments does not require acidification. *Am. J. Physiol.*, **269**, G548-557.

76. Sanchez, J. and Holmgren, J. (2008) Cholera toxin structure, gene regulation and pathophysiological and immunological aspects. *Cell Mol Life Sci*, **65**, 1347-1360.

77. Martin, T. F. J. and Grishanin, R. N. (2003) PC12 Cells as a Model for Studies of Regulated Secretion in Neuronal and Endocrine Cells. *Meth Cell Biol*, **71**, 267-286.

78. Majoul, I., Schmidt, T., Pomasanova, M., Boutkevich, E., Kozlov, Y. and Söling, H.-D. (2002) Differential expression of receptors for Shiga and Cholera toxin is regulated by the cell cycle. *J Cell Sci*, **115**, 817-826.

79. Voet, D., Voet, J. G. and Pratt, C. W. *Fundamentals of Biochemistry*, John Wiley & Sons: New York, 2002.

80. Davies, S. P., Reddy, H., Caivano, M. and Cohen, P. (2000) Specificity and mechanism of action of some commonly used protein kinase inhibitors. *Biochem J*, **351**, 95-105.

81. Cohen, P. (2003) The Effective Use of Protein Kinase Inhibitors. *Cell Transm*, **19**, 11-14.

82. Lencer, W. I., Moe, S., Rufo, P. A. and Madara, J. L. (1995) Transcytosis of cholera toxin subunits across model human intestinal epithelia. *Proc Natl Acad Sci USA*, **92**, 10094-10098.

83. Orlandi, P. A., Curran, P. K. and Fishman, P. H. (1993) Brefeldin A Blocks the Response of Cultured Cells to Cholera Toxin. *J. Biol Chem.*, **268**, 12010-12016.

84. Mickevicius, C. K., Harrison, J. K. and Genegy, M. E. (1986) Effect of Cholera Toxin on the Activation of Adenylate Cyclase by Calmodulin in Bovine Striatum. *Mol. Pharacol.*, **30**, 469-475.

85. CDC. Bioterrorism Agents/ Diseases. http://www.bt.cdc.gov/agent/agentlist-category.asp#b (accessed

86. Rusnak, J. M., Kortepeter, M., Ulrich, R., Poli, M. and Boudreau, E. (2004) Laboratory Exposures to Staphylococcal Entertoxin B. *Emerg Infect Dis*, **10**, 1544-1549.

87. Smith, T. L., Pearson, M. L., Wilcox, K. R., Cruz, C., Lancaster, M. V., Robinson-Dunn, B., Tenover, F. C., Zervos, M. J., Band, J. D., White, E. and Jarvis, W. R. (1999) Emergence of Vancomycin Resistance in *Staphylococcus Aureus*. *New Engl J Med*, **340**, 493-501.

88. Fraser, J., Arcus, V., Kong, P., Baker, E. and Proft, T. (2000) Superantigens - powerful modifiers of the immune system. *Mol Med Today*, **6**, 125-132.

89. Choi, Y. W., Kotzin, B., Herron, L., Callahan, J., Marrack, P. and Kappler, J. (1989) Interaction of Staphylococcus aureus toxin "superantigens" with human T cells. *Proc Natl Acad Sci USA*, **86**, 8941-8945.

90. Lavoie, P. M., Thibodeau, J., Erard, F. and Sekaly, R.-P. (1999) Understanding the mechanism of action of bacterial superantigens from a decade of research. *Immunol Rev*, **168**, 257-269.

91. Zhou, J., Hu, L., Guo, K., Huang, Y., Guo, A., Wu, Y., Wang, Y. and Tu, S. (2007) Establishment of genescan technique of diversity gene of T cell antigen receptor CDR3 for assaying clonality of human TCR T cell. *Shandong Yiyao*, **47**, 7-9.

92. Cao, C. J., Mioduszewski, R. J., Menking, D. E., Valdes, J. J., Cortes, V. I., Eldefrawi, M. E. and Eldefrawi, A. T. (1997) Validation of the cytosensor for in vitro cytotoxicity studies. *Toxicol In Vitro*, **11**, 285-293.

93. Snider, R. M., Ciobanu, M., Rue, A. E. and Cliffel, D. E. (2008) A multiwalled carbon nanotube/dihydropyran composite film electrode for insulin detection in a microphysiometer chamber. *Anal. Chim. Acta*, **609**, 44-52.

94. Tudorache, M. and Bala, C. (2007) Biosensors based on screen-printing technology, and their applications in environmental and food analysis. *Anal Bioanal Chem*, **388**, 565-578.

95. Huang, X.-J., O'Mahony, A. M. and Compton, R. G. (2009) Microelectrode arrays for electrochemistry: approaches to fabrication. *Small*, **5**, 776-788.

96. Tymecki, L., Glab, S. and Koncki, R. (2006) Miniaturized, planar ion-selective electrodes fabricated by means of thick-film technology. *Sensors*, **6**, 390-396.

97. Glab, S., Adam, H., Edwall, G. and Ingman, F. (1989) Metal-Metal Oxide and Metal Oxide Electrodes as pH sensors. *Crit. Rev. in Anal. Chem.*, **21**, 29-47.

98. Cater, D. B. and Silver, I. A. Microelectrodes and Electrodes Used in Biology In *Reference Electrodes: Theory and Practice*; Ives, D. J. G., Ed.; Academic Press: New York, 1961, pp 464-523.

99. Marzouk, S. A. M. (2003) Improved Electrodeposited Iridium Oxide pH Sensor Fabricated on Etched Titanium Substrates. *Anal Chem*, **75**, 1258-1266.

100. Baur, J. E. and Spaine, T. W. (1998) Electrochemical deposition of iridium (IV) oxide from alkaline solutions of iridium(III) oxide. *J Electroanal Chem*, **443**, 208-216.

101. Prokop, A., Prokop, Z., Schaffer, D., Kozlov, E., Wikswo, J., Cliffel, D. and Baudenbacher, F. (2004) NanoLiterBioReactor: long-term mammalian cell culture at nanofabricated scale. *Biomed Microdevices*, **6**, 325-339.

102. Sia, S. K. and Whitesides, G. M. (2003) Microfluidic devices fabricated in Poly(dimethylsiloxane) for biological studies. *Electrophoresis*, **24**, 3563-3576.

103. Leclerc, E., Sakai, Y. and Fujii, T. (2003) Cell Culture in 3-Dimensional Microfluidic Structure of PDMS (polydimethylsiloxane). *Biomedical Microdevices*, **5**, 109.

104. Wu, M.-H. (2009) Simple poly(dimethylsiloxane) surface modification to control cell adhesion. *Surf Interface Anal*, **41**, 11-16.

105. Keranov, I., Vladkova, T., Minchev, M., Kostadinova, A. and Altankov, G. (2008) Preparation, characterization, and cellular interactions of collagen-immobilized PDMS surfaces. *J Appl Polym Sci*, **110**, 321-330.

106. Bard, A. J. and Faulkner, L. R. *Electrochemical Methods: Fundamentals and Applications*, 2nd ed., John Wiley and Sons, Inc: New York, 2001.

Jennifer (Merritt) McKenzie

Vanderbilt University, 7330 Stevenson Center, Station B 351822, Nashville, TN 37235 615-322-5013
jennifer.mckenzie@vanderbilt.edu

Education

Vanderbilt University, Nashville, TN
Ph.D., Department of Chemistry
Advisor: Dr. David E. Cliffel
Graduation: May 2011

Hendrix College, Conway, AR
ACS Certified B.A. in Chemistry
Spring 2006
Graduated *magna cum laude* with Distinction in Chemistry

Citizenship

United States of America

Research Interests

To develop novel methods and instrumentation for quantitative and sensitive detection of biomolecules, especially those which aim to improve current detection methods at the clinical or point-of-care level.

Research Experience

Vanderbilt University, Nashville, TN, 2007-Present
Graduate Research Advisor: Dr. David E. Cliffel

- Utilized and trained peers on current microphysiometry platform for real-time monitoring of cellular metabolites in response to stressors
- Developed and implemented a new platform for real-time monitoring of cellular metabolites in a microfluidic device to replace the current technology
- Revealed new insights into the metabolic adaptation of ischemic neurons with microphysiometry
- Worked closely with collaborators to test and improve a multichannel multipotentiostat for simultaneous amperometric and potentiometric sensing in up to six individual microfluidic chambers
- Investigated the immediate metabolic effects of biological toxins
- Mentored and supervised the research of four graduate students and six undergraduates, one of whom was then selected as a Beckman Scholar

Hendrix College Department of Chemistry, Conway, AR, 2005-2006
Undergraduate Research
Advisor: Dr. Liz Gron

- Collected water and soil samples
- Analyzed samples from local water and soil sources for nitrates and phosphates using ion chromatography to draw conclusions about contribution of fertilizers and water treatment plants in local water pollution
- Trained other students on the department's new ion chromatography system and wrote a standard operating procedure for future student use

Hendrix College Department of Chemistry, Conway, AR, Summer 2006
Lab Assistant
Advisor: Dr. Warfield Teague

- Designed and tested new green environmental chemistry labs for use in a non-science major chemistry course
- Supervised students during lab testing and used feedback to improve written laboratories

- Wrote end-of-term student evaluation to gauge student performance and determine effectiveness of labs in teaching learning objectives

Expertox, Inc., Deer Park, TX, Summer 2004 and 2005
Lab Assistant

- Organized and tracked samples collected on-site and off-site (hospitals, medical examiners, private clients) for toxicological testing
- Prepared human biological samples for GC/MS, ICP/MS, and drug assay testing
- Collected specimens from patients
- Performed urinalysis assays and analyzed blood samples for blood alcohol concentration using GC/MS

Publications

Rachel M. Snider, **Jennifer R. McKenzie** (co-authors), Lewis Kraft, Eugene Kozlov, John P. Wikswo, and David. E. Cliffel. "The Effects of Cholera Toxin on Cellular Energy Metabolism" *Toxins* **2010**, *2*(4), 632-648.

Stephanie L. H. Zeiger, **Jennifer R. McKenzie**, Jeannette N. Stankowski, Jacob A. Martin, David E. Cliffel, and BethAnn McLaughlin. "Neuron Specific Metabolic Adaptations Following Multi-Day Exposures to Oxygen Glucose Deprivation" Biochim. Biophys. Acta, Mol. Basis Dis. **2010**, 1802, 1095-1104.

Manuscripts in Preparation

Jennifer R. McKenzie, Leslie A. Hiatt, David Shaffer, Phillip Samson, Dmitri Markov, John P. Wikswo, David E. Cliffel. "Development of a Screen-printed Electrode for Real-time Monitoring of Cellular Metabolism in a Microfluidic Environment"

Jennifer R. McKenzie, Jacquelynn E. Brown, Amy M. Kleman, BethAnn McLaughlin, and David E. Cliffel. "Extracellular Acidosis is An Essential Mediator of Neuronal Preconditioning: New Insight from the Use of Metabolic Multianalyte Microphysiometry"

Jennifer R. McKenzie, David E. Cliffel. "Differential Metabolic Effects of Staphylococcal Entertoxin B on Affected Cell Types"

Leslie A. Hiatt, **Jennifer R. McKenzie**, Leila F. Deravi, S. Reese Harry, David W. Wright, and David E. Cliffel. "A printed Superoxide Dismutase Coated Electrode for the Study of Macrophage Oxidative Burst."

Eduardo A. Lima, Rachel M. Snider, Ronald S. Reiser, **Jennifer R. McKenzie**, Sven Eklund, David E. Cliffel, John P. Wikwo. "Multichamber Multipotentiostat for Cellular Microphysiometry"

Conference Oral Presentations

McKenzie, Jennifer R., Wikswo, J. P., Cliffel, D. E. Adaptation of a Platinum Screen-printed Electrode for the Real-time Monitoring of Cellular Metabolism in a Microfluidic Environment. Oral Presentation, Pittsburg Conference, Orlando, Fl, February 28-March 5, 2010.

McKenzie, Jennifer R., Wikswo, J.P.; Cliffel, D.E. Physiological Effects of Staphylococcal Enterotoxin B on an Epithelial Colorectal Adenocarcinoma Cell Line. Oral Presentation, Chemical and Biological Science and Technology Conference, Dallas, TX, November 16-20, 2009.

Merritt, Jennifer R.; Wikswo, J.P.; Cliffel, D.E. A Multi-Analyte Platinum Screen-Printed Electrode for Real-Time Monitoring of Cellular Metabolism in a Microfluidic Device. Oral Presentation, 60th Southeast Regional Meeting of the American Chemical Society, Nashville, TN, United States, November 12-15, 2008.

Merritt, Jennifer R.; Wikswo, J.P.; Cliffel, D.E. A Platinum Screen-printed Electrode for Real-time Monitoring of Cellular Metabolism in a Microfluidic Device. Oral Presentation, Pacific Rim Meeting on Electrochemical and Solid-State Science, Honolulu, HI, October 12-17, 2008.

Conference Poster Presentations

McKenzie, Jennifer R., Brown, J.E., McLaughlin, B. A., Cliffel, D.E. Development of New Techniques to Study Neural Preconditioning Phenomenon with Multi-analyte Microphysiometry. Poster presentation, 2009 Vanderbilt Institute of Chemical Biology Retreat. Nashville, TN, August 13, 2009.

Merritt, Jennifer R., Gron, Liz. Connecting students to the environment through green, analytical ion chromatography. Undergraduate poster, 231st ACS National Meeting, Atlanta, GA, March 26-30, 2006.

Merritt, Jennifer R., Gron, Liz. Winning over the environmentalists with green, analytical chemistry. Undergraduate poster, 231st ACS National Meeting, Atlanta, GA, March 26-30, 2006.

Teaching Experience

Vanderbilt University, Nashville, TN, Summer 2007 to Present
Graduate and Undergraduate Mentor

- Mentored four undergraduate biomedical engineers developing microfluidic housing for a single analyte screen-printed electrode
- Mentored two undergraduates performing independent research in microphysiometry
- Mentored four graduate students, two of which joined the laboratory

Vanderbilt University, Nashville, TN, Fall 2006
General Chemistry, Teaching Assistant

- Instructed sixty students during weekly laboratory experiments
- Assisted students during office hours
- Graded written lab reports and exams

Vanderbilt University, Nashville, TN, Spring 2007
Vanderbilt Student Volunteers for Science (VSVS), Graduate Team Leader

- Instructed a 5^{th} and 6^{th} grade class in Nashville public schools in weekly hands-on science lessons
- Trained and supervised undergraduate volunteers in lesson plans

Hendrix College, Conway, AR, 2003-2006 General Chemistry, Teaching Assistant

- Instructed thirty to sixty students during weekly laboratory experiments
- Graded weekly lab reports of sixty to ninety students
- Reviewed multiple years of student performance to determine effectiveness of labs in teaching learning objectives

Distinctions

Chemical and Biological Defense Science and Technology Conference, Student Travel Full Scholarship, Dallas, TX, 2009

Electrochemical Society Travel Grant to attend ECS Meeting, Honolulu, HI, 2008

Graduate Assistance in Areas of National Need Fellowship, Vanderbilt University, 2006-2007

Chairman's Scholarship, Hendrix College, 2002-2006

Scientific Skills

Electrochemistry – Sensor design, amperometry, voltammetry, reference electrode fabrication, electrodeposition, electropolymerization, enzyme-based sensors

Cell Culture – Maintained cell lines for research including seeding, counting, splitting, plating, cell viability assays, growth on PDMS and porous membranes

Microfabrication- PDMS, profilometry, plasma treatment, silanization, photolithography, e-beam evaporation, some AutoCAD

Microphysiometry – Instrument repair, custom electrode fabrication, enzyme-based electodes, real-time metabolic analysis, work with and edit National Instruments LabVIEW-based software

Additional techniques – Biosafety level II training, ion chromatography, GC/MS, atomic absorption spectroscopy

Leadership

Laboratory Safety Officer, 2007-Present

As senior graduate student, responsible for day-to-day operations in the lab, including lab orientation and training, recruitment sessions, scheduling, ordering supplies, maintenance of instrumentation, several lab moves, and organization of newly renovated laboratory spaces, 2008 - Present

Section leader for Music City Community Chorus, 2007-2010

President of Hendrix Chapter of Student Affiliates of the American Chemical Society, 2005-2006

President of Hendrix Choir, 2005-2006

Publicity Chair of Hendrix Chapter of Student Affiliates of the American Chemical Society, 2004-2005

Treasurer of Hendrix Choir, 2005-2006

Professional Affiliations

The American Chemical Society

The Electrochemical Society

The Society for Electroanalytical Chemisty

References

Dr. David Cliffel, Associate Professor of Chemistry
(615) 343-3937
d.cliffel@vanderbilt.edu

Dr. John Wikswo, Director, Vanderbilt Institute for Integrative Biosystems Research and Education
(615)-343-4124
john.wikswo@vanderbilt.edu